IN VIVO ULTRASOUND-SWITCHABLE FLUORESCENCE IMAGING AND ITS APPLICATIONS

by

TINGFENG YAO

Presented to the Faculty of the Graduate School of

The University of Texas at Arlington in Partial Fulfillment

of the Requirements

for the Degree of

DOCTOR OF PHILOSOPHY

THE UNIVERSITY OF TEXAS AT ARLINGTON

August 2020

Acknowledgements

I would like to express my deepest gratitude to my supervisor, Prof. Baohong Yuan, for his guidance, patience, understanding and encouragement throughout my Ph.D. study. His rigorous and serious academic attitude has been a great model for me. His dedication and passion for work has always inspired me. I sincerely appreciate the independent work platform he provides with tremendous resource and trust. His guidance has helped me to be a better researcher and person.

It is my privilege to have Dr. Hanli Liu, Dr. Georgios Alexandrakis, Dr. Yi Hong, and Dr. Juhyun Lee on my dissertation committee. I am sincerely grateful for all the insightful criticisms and suggestions given for this thesis.

I would like to thank my colleagues and friends, Miss. Liqin Ren, Mr. Yang Liu, Dr. Ruilin Liu, Dr. Shuai Yu, Dr. Wenbin Cai and Dr. Jayanth Kandukuri for their professional contributions, discussions, companions, and support during the last five years.

I would also like to thank the Office of Graduate Studies Dissertation Fellowship, which supports me to focus effort on completing this thesis.

I am grateful to my friend, Shuxin Li, who has given me great help in life during the past years.

This work was supported in part by funding from the CPRIT RP170564 (PI: Baohong Yuan) and the NSF CBET- 1253199 (PI: Baohong Yuan).

Last but not least, I can never be thankful enough to my grandmother and my mother, whose love and support are the constant source of strength and inspiration for me.

June 29th, 2020

Abstract

IN VIVO ULTRASOUND-SWITCHABLE FLUORESCENCE IMAGING AND ITS APPLICATIONS

Tingfeng Yao, PhD

The University of Texas at Arlington, 2020

Supervising Professor: Baohong Yuan

The conventional fluorescence imaging has limited spatial resolution in centimeters-deep tissue because of the tissue's high scattering property. Ultrasound-switchable fluorescence (USF) imaging, a new imaging technique, was recently proposed to realize high-resolution fluorescence imaging in centimeters-deep tissue. Although promising results were achieved in tissue-mimic phantoms or tissue samples, the *in vivo* USF imaging had not been realized so far. There were two major challenges in realizing *in vivo* USF imaging. First, the lack of stable near-infrared (NIR) USF contrast agents in a biological environment and the lack of data about their biodistributions. Second, the previous USF imaging systems adopted a fiber bundle to collect the emitted fluorescence photons, which led to a few limitations, such as (1) low photon-collection efficiency; (2) low efficiency for scanning a sample with an uneven surface (such as a mouse); (3) low imaging speed, because of the adoption of a raster scan and the long wait time for the tissue to cool down before starting the data acquisition at the next location. This work focuses on two parts: (1) investigating the biodistribution of the NIR USF contrast agents in mice and demonstrating their feasibility of *in vivo* USF imaging; (2) developing camera-based USF imaging systems and a faster scan method.

First, the biodistribution of the Indocyanine green (ICG)-encapsulated poly(N-isopropylacrylamide) (PNIPAM) nanoparticle (ICG-PNIPAM NP) in mice was studied. The ICG-PNIPAM NP (with an average diameter of ~335 nm) was mainly accumulated into the spleen of the mice. *In vivo* and *ex vivo* USF imaging of the mouse spleen via intravenous injections using frequency-domain USF imaging system were successfully achieved. The accuracy of the USF imaging was validated by a commercial micro-CT system. Second, an electron-multiplying charge-coupled device (EMCCD) camera-based USF imaging system was proposed to overcome the limitations of the previous fiber bundle-based USF imaging systems. Thanks to the spatial information provided by the camera, a new scan method, Z-scan, was developed, and the imaging speed was improved four times over the raster scan. Third, the biodistribution of β-cyclodextrin/ICG complex-encapsulated PNIPAM nanogel (PNIPAM/β-CD/ICG nanogel) in

mice was investigated. The PNIPAM/β-CD/ICG nanogel (with an average diameter of ~32 nm) could quickly accumulate into the liver tissue and then degrade fast in a short period. Animal experiments also showed that the present nanogels were able to be effectively accumulated into U87 tumor of a live mouse via the enhanced permeability and retention effect. The *ex vivo* USF imaging of the mouse liver and *in vivo* USF imaging in mouse tumor using the EMCCD camera-based USF imaging system were successfully obtained. Fourth, an improved EMCCD camera-based USF imaging system via a software trigger mode was proposed. The USF imaging of a sub-millimeter silicone tube with an inner diameter of 0.76 mm and an outer diameter of 1.65 mm in 5.5 cm-thick chicken breast tissue using 808 nm excitation light with a low intensity of 28.35 mW/cm^2 was successfully achieved.

In summary, the results provided in this work demonstrated for the first time the feasibility of USF imaging in living mice. Both ICG-PNIPAM NP and PNIPAM/β-CD/ICG nanogel showed great stability in a biological environment. Their biodistributions were different due to the various sizes. Camera-based USF imaging systems could improve the photon collection efficiency and increase the imaging speed by adopting a Z-scan method. The USF imaging of submillimeter objects in centimeters-deep tissue could be achieved by optimizing the gain of the EMCCD camera. This work has paved the way for adopting USF imaging technique in many potential biomedical applications in future.

Table of Contents

List of Illustrations

List of Tables

Chapter 1

INTRODUCTION

1.1 Motivation of Ultrasound-Switchable Fluorescence Technique

Biomedical optical imaging based on fluorescence has been intensively developed during the past decades and is playing important roles in many applications, such as fluorescence microscopy [1, 2], two-dimensional (2D) fluorescence planar imaging [3, 4], and three-dimensional (3D) fluorescence diffuse optical tomography [5, 6]. It has high sensitivity and specificity with benefits of low cost, use of non-ionizing radiation and capability of multicolor imaging. Besides fluorescence microscopy, imaging based on fluorescence contrast in deep tissues (such as centimeters) attracts a lot of interests too because it has many unique advantages compared with other modalities, such as x-ray, magnetic resonance imaging (MRI), and positron-emission tomography (PET). For example, it can provide unique opportunities to simultaneously image multiple biological targets via multiple colors and therefore make it possible to investigate the interactions among these targets [7, 8]. This may include examples such as monitoring migration of cancer cells or cell clusters into blood vessels in metastasis in deep tissues by differentiating the cells from the vessels via labeling them with different colored fluorophores. Also, it may be used to increase the imaging specificity to a biological target in deep tissues (such as cancer stem cells or cell clusters) by simultaneously identifying the multiple biomarkers of the target via multicolored fluorophores.

However, fluorescence imaging in deep tissues has been facing several dilemmas since its invention because of the tissue's high scattering property [9]. First, its spatial resolution significantly degrades with the increase of tissue thickness, such as from submicrons for microscopy in a tissue sample with a thickness of a few hundred microns to a few millimeters in a tissue with a thickness of a few centimeters. The low resolution will lead to unwanted spatial overlap of different fluorescence signals and difficulty differentiating them. Second, to achieve high spatial resolution in deep tissue, the sensitivity can be an issue since the detectable photons become limited due to the improvement of spatial resolution. Third, nonspecific photons, which may come from tissue autofluorescence, laser leakage, or stray light in the environment, are always noises and reduce the specificity and sensitivity of signal to its contrast agents in deep tissues.

Ultrasound imaging is another imaging modality widely used in biomedical applications [10]. It has the advantages of low cost, use of non-ionizing radiation, real-time imaging capability, and ability to characterize tissues. Ultrasound imaging can achieve high spatial resolution while maintaining large penetration depth, because the

ultrasonic wave with a frequency of megahertz is scattered two to three magnitudes smaller than of photons in biology tissues [11]. However, ultrasound imaging does not have sensitivity to fluorescent molecules. Thus, it makes sense to combine the high resolution and large penetration depth from ultrasound imaging, including strong contrast from fluorescence imaging, in order to achieve high resolution fluorescence imaging in centimeters-deep tissue. Several hybrid imaging modalities combining fluorescence and ultrasound have been proposed and demonstrated, such as ultrasound-modulated fluorescence [12-15], ultrasound-induced temperature-controlled fluorescence [16-18], and time-reversed ultrasonically encoded optical focusing [19-23]. These technologies have been shown to be able to achieve high acoustic resolution and retain fluorescence contrast in deep scattering media.

During the past years, a new hybrid imaging technique, ultrasound-switchable fluorescence (USF), has been developed to realize fluorescence imaging with high spatial resolution in centimeters-deep tissue [18, 24-28]. What makes USF different from others is the unique contrast agent that can be switched on via ultrasound-induced thermal energy (or temperature rise) only in the ultrasound focal volume. By scanning the ultrasound focus, a 3D USF image can be acquired with fluorescence contrast and ultrasound resolution. Unlike MRI, ultrasound, x-ray based computed tomography (CT) and photoacoustic imaging [29], USF signal has extremely high specificity to its contrast agent, which means the detected USF signal can only come from its contrast agent. This feature is similar to PET imaging in which the detected γ photons only come from the positrons emitted by the injected radioactive isotope [30]. In addition, USF signal strength and dynamic pattern can be externally manipulated by controlling the ultrasound exposure, which makes the USF signal uniquely differentiated from the noise to achieve high signal-to-noise ratio (SNR) or sensitivity. Besides structural, functional and molecular imaging, USF can be seamlessly combined with high-intensity focused ultrasound (HIFU) treatment as a tool predicting pre-treatment, monitoring intro-treatment and evaluating post-treatment.

1.2 Principle of USF Imaging Technique

The basic mechanism of USF imaging is shown in Figure 1-1. Briefly, the principle of USF is to use a HIFU beam to control the fluorescence emission of the fluorophores in the ultrasound focal zone. The USF imaging technique contains two main parts: the USF contrast agent and an acoustic-optical imaging system. The USF contrast agents are synthesized by encapsulating environment-sensitive fluorophores into thermal-sensitive nanoparticles [24, 31]. The fluorophores emit weak fluorescence (i.e., the ‘OFF’ state) when the temperature is below a threshold. By applying a HIFU transducer to illuminate the tissue, the temperature quickly rises at the focal zone by a few degrees

Celsius and reaches the threshold to change the micro-environment inside the nanoparticles. The intensity of the emitted fluorescence becomes stronger due to the increased quantum yield of the fluorophores (i.e., the 'ON' state). The increased fluorescence (i.e., the USF signal) is then detected by a sensitive optical imaging system. Because the USF photons only come from the thermal focal zone, a fluorescence image with ultrasound resolution can be achieved by scanning the HIFU focus inside the tissue.

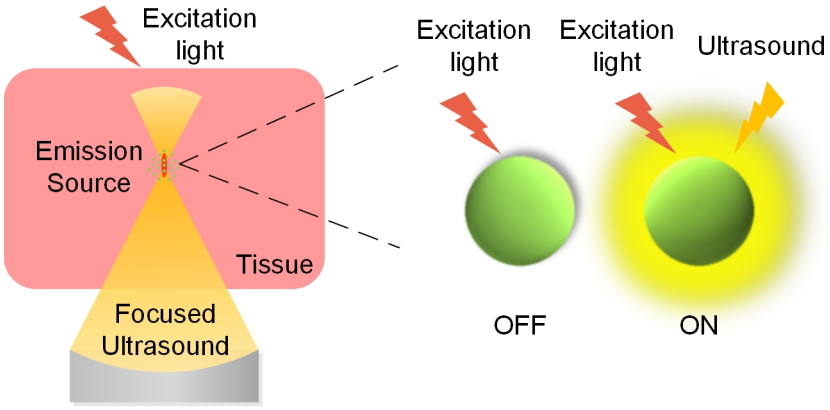

Figure 1-1 Schematic diagram of USF principle.

1.3 SNR and Resolution

The SNR and the resolution are usually used to evaluate the performance of an imaging system. Herein, these two parameters of the USF technique are discussed.

1.3.1 SNR

The USF signal is defined as the increased fluorescence from the thermal focal zone induced by the HIFU heating (i.e., the increased output signal of the system). Ideally, the output signal of the USF imaging system should be zero or a constant value when the HIFU is off. However, in real case, it is variant in absence of ultrasonic energy. This variation is considered as the noise of the USF system. The noise sources can be characterized into two types:

(a) The variation of the incident light illuminated on the detector. One source of this kind of noise is the instability of the excitation laser which is environment depended. If the laser output changes in a timescale of second or hundreds of milliseconds, it would affect the USF signal whose duration time is in the same time scale. Another source of this noise often appears in living animal experiments. The breath of the anesthetized animal which is usually periodical with a frequency of sub Hertz or a few Hertz may affect the system's output. Especially, the noise caused by breathing is significant when the scan area of USF imaging is at or closed to the chest.

(b) The electronic noises of the USF system. The main electronic noises are the shot noise and the instability of the system's gain. The shot noise is depended on the received photons. When the ultrasound is not applied, the received photons (i.e., the background photons) are composed of the tissue's autofluorescence, laser leakage and the fluorescence from non-100%-off contrast agents. Moreover, the received photons are usually needed to be significantly amplified. If the gain of the detector is instable, additional noise will be introduced to the output signal. Thus, it is crucial to improve the SNR by reducing the background photons, so that USF photons can stand out of the noise.

Several methods have been proposed to improve the SNR based on the unique pattern of the USF signal [25, 27]. In the frequency-domain (FD) USF system, the detected USF signal usually has a sharp rising edge and a relative long falling edge. Therefore, the SNR of the USF image can be improved by adopting a correlation method [25]. To make the USF signal pattern more unique than the noise, collected USF signal can be encoded by modulating the temperature within the tissue sample. Modulation of the temperature is achieved by modulating the ultrasound pressure wave via controlled switching of the HIFU transducer [27].

1.3.2 Resolution

The spatial resolution of an imaging system is commonly defined as the minimum separation distance at which two objects are individually resolved. In USF imaging, it is depended on the size of the thermal focal volume induced by the HIFU heating. The thermal focal volume can be controlled by changing the exposure time and the intensity of the ultrasound or the optical detection time [32]. In order to confine the enhanced fluorescence emission into the ultrasound focal zone, thermal confinement should be met by adopting a short HIFU exposure time (e.g., few hundreds of milliseconds). It should be noted that the lateral resolution of the USF imaging system is usually much better than the axial resolution because of the inherent nonuniform shape of the ultrasound focus [33].

There are several ways to improve the spatial resolution of the USF imaging. First, nonlinearity of the HIFU heating can be used by adopting a shorter exposure time with a higher intensity. Thus, the size of thermal focal zone can be even smaller than that of the ultrasound focus, which means the USF technique has the ability to break the acoustic diffraction [33]. It should be careful to increase the HIFU intensity to avoid causing any mechanical damage to the tissue [34]. Second, a HIFU transducer with a higher frequency can be used because the size of the ultrasound focus is depended on its frequency. However, the absorption of ultrasound in biological tissue rises with the increase of ultrasound frequency [35]. Thus, the penetration depth will be reduced when using a transducer with a higher

frequency. Third, the axial resolution of USF imaging can be improved by using dual HIFU transducers placed perpendicular to each other. This could contribute to a more uniform thermal distribution in its lateral and axial direction [26].

Obviously, there is a tradeoff between the SNR and the resolution. The resolution is improved by reducing the size of the thermal focal volume. Therefore, the amount of USF contrast agent in the focal volume will be correspondingly less (i.e., less fluorophores can be switched on). Meanwhile, the noise which is not related to the focal size will keep stable. Hence, the SNR rapidly reduces as the resolution increases.

1.4 USF Contrast Agents

As shown in Figure 1-2, the fluorescence of the USF contrast agent changes as a step function of the temperature. The USF contrast agents are usually characterized via the following parameters: (1) the wavelengths of peak excitation and emission (λ_{ex} and λ_{em}); (2) the fluorescence intensity ratio between on and off states ($R_{On/Off}=I_{On}/I_{Off}$); (3) the temperature threshold to switch on fluorophores (T_{th}); and (4) the temperature transition bandwidth (TBW).

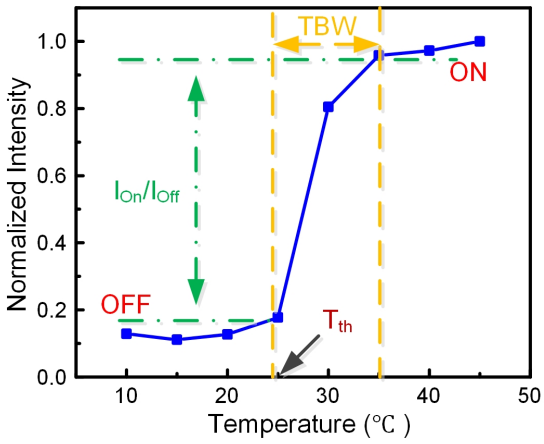

Figure 1-2 Fluorescence intensity changes as a function of temperature.

As mentioned in the previous section, it is important to reduce the background photons to improve the SNR. The autofluorescence of the tissue can be minimized by adopting λ_{ex} and λ_{em} in near-infrared (NIR) region. To reduce the non-100%-off fluorescence, a USF contrast agent with a large $R_{On/Off}$ is desired. An important consideration during USF imaging is to avoid tissue damage due to thermal ablation. Therefore, the USF contrast agent should exhibit a narrow TBW (e.g., a few degree Celsius). Also, the USF contrast agents with different T_{th} or the lower critical solution

temperature (LCST) are required depending on the application. For example, phantom studies require LCST around ~24-26 ℃ (i.e., the room temperature) while the *in vivo* studies require LCST above ~37 ℃ (i.e., physiological body temperature) [36].

Several USF contrast agents have been proposed so far [24, 25, 31, 37, 38]. Although 4,4-difluoro-4-bora-3a,4a-diaza-sindacene (aza-BODIPY) dyes encapsulated Pluronic micelles showed splendid performance in phantom studies, they are difficult to be used for USF imaging in living tissues because of the instability of these contrast agents in biological environments [25, 37]. Therefore, the Indocyanine green (ICG)-encapsulated poly(N-isopropylacrylamide) (PNIPAM) nanoparticle (ICG-PNIPAM NP) is used in this study to demonstrate the feasibility of *in vivo* USF imaging [31]. ICG is a U.S. Food and Drug Administration (FDA) approved NIR dye with a peak excitation at 780 nm and a peak emission at 830 nm [39]. It demonstrates an increased fluorescence intensity upon decreasing solvent's polarity [24]. The PNIPAM nanoparticles will shrink to expel the water molecules from the nanoparticles when the temperature is increased above the LCST. Hence, the fluorescence emission of the ICG molecules inside the nanoparticle is enhanced due to less polarized microenvironment. One of the drawbacks of ICG-PNIPAM NP is that its emission peak is significantly blue shifted compared to that of free ICG in water. Recently, a β-cyclodextrin/ICG complex-encapsulated PNIPAM nanogel (PNIPAM/β-CD/ICG nanogel) was proposed to overcome this limitation [38]. The excitation/emission characteristics of the ICG itself in PNIPAM/β-CD/ICG nanogel were almost completely retained. Additionally, the average diameter of the nanogels was significantly decreased to ~32 nm from ~335 nm compared to the ICG-PNIPAM nanoparticles. In this study, *in vivo* USF imaging using PNIPAM/β-CD/ICG nanogel was also carried out.

1.5 Fiber-Bundle Based USF Imaging Systems

The schematic diagram of a typical fiber-bundle based USF imaging system is shown in Figure 1-3 [24]. The USF system is composed of three main subsystems: (1) an optical system to deliver the excitation light and collect the emitted fluorescence, (2) an ultrasonic system to induce temperature rise, and (3) an electronic system to control the laser excitation, data acquisition and HIFU scanning. The excitation light passes through an emission filter (F1), a shutter and illuminates the sample. The emitted fluorescence from the sample is collected by a fiber bundle and filtered by a set of emission filters (F2–F5). It is finally focused on a cooled photomultiplier tube (PMT) and converted into an electronic signal. This signal is further amplified and acquired by an oscilloscope. A HIFU transducer driven by a function generator is used to switch on/off the USF contrast agent. The driving signal is amplified by a radio frequency

power amplifier (RF-AMP). The amplified signal is delivered to a matching network (MNW) and then the HIFU transducer to generate an ultrasonic wave. A pulse delay generator (PDG) is used to synchronize the laser excitation by controlling the shutter, the HIFU exposure and the data acquisition. A motorized translation stage controls the HIFU transducer to realize the sample scanning.

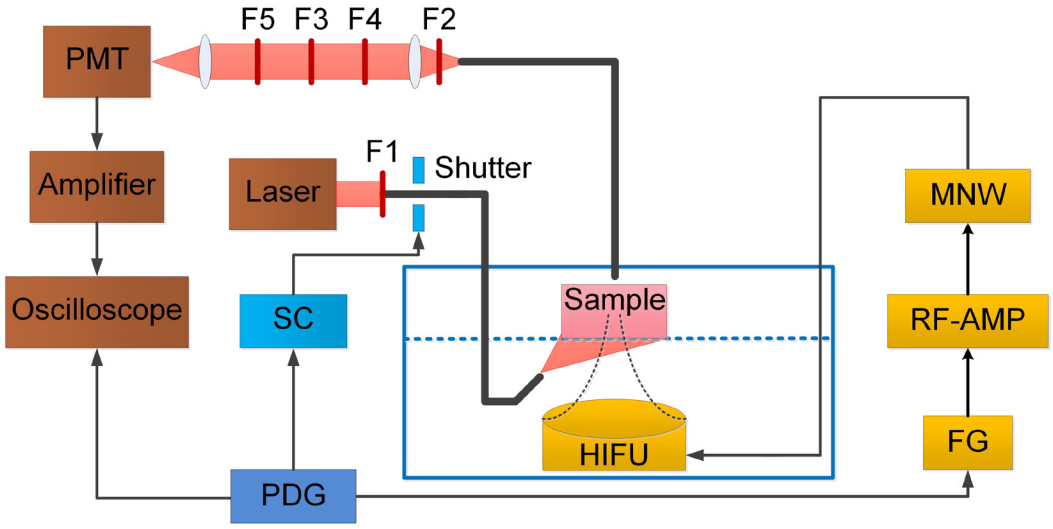

Figure 1-3 The schematic diagram of the fiber-bundle based USF imaging system. FG: function generator; RF-Amp: radio-frequency power amplifier; MNW: matching network; HIFU: high intensity focused ultrasound; PMT: photomultiplier tube; F1: excitation filter; F2–F5: emission filters; SC: shutter controller; PDG: pulse delay generator.

To improve the sensitivity of the above USF system, an FD-USF imaging system using modulated excitation light and a lock-in amplifier (LIA) to further amplify the detected signal was proposed [25]. Although promising results have been achieved in tissue phantoms via these fiber-bundle based USF systems, these systems suffer from a low photon collection efficiency. Additionally, attention must be paid when scanning tissue with an uneven surface (such as a mouse). Moreover, the imaging speed is limited by the time required to cool the tissue to minimize the thermal diffusion effect between the two adjacent locations in the scanning sequence. Therefore, in this study, camera-based USF imaging systems were developed to overcome these limitations.

1.6 Dissertation Outline

The motivation of the thesis is to demonstrate the feasibility of *in vivo* USF imaging in mice and improve the USF imaging systems. The approach is to investigate the biodistribution of the NIR USF contrast agents in mice and

perform the USF imaging of the organs in which the contrast agents are accumulated. Novel camera-based USF imaging systems suitable for animal study were proposed and a faster scan method was developed.

In chapter 2, the biodistribution of the ICG-PNIPAM NP in mice was investigated. The USF imaging in porcine heart tissue and mouse breast tumor via local injections were studied and demonstrated. *In vivo* and *ex vivo* USF imaging of the mouse spleen via intravenous injections were also successfully achieved. By comparing the results of CT imaging and the results of USF imaging, the accuracy of USF imaging was proved.

In chapter 3, an electron-multiplying charge-coupled device (EMCCD)-camera based USF imaging system was developed to overcome the limitations of the previous fiber-bundle based USF imaging systems. A new scan method, Z-scan, was developed to significantly improve the imaging speed compared to the conventional raster scan. The USF imaging using the Z-scan for tissue samples was realized and the results were validated by a commercial micro-CT system.

In chapter 4, the feasibility of *in vivo* USF imaging using PNIPAM/β-CD/ICG nanogel and the camera-based USF imaging system was investigated. The USF performances of the ICG-PNIPAM NP and PNIPAM/β-CD/ICG nanogel were compared in centimeters-thick chicken breast tissue. The biodistribution of the PNIPAM/β-CD/ICG nanogel in mice was studied. The *ex vivo* USF imaging of the mouse liver was obtained. The *in vivo* USF imaging in mouse tumor was also successfully achieved.

In chapter 5, an improved EMCCD camera-based USF imaging system using software trigger was developed. The stability of the EM gain of the EMCCD camera was compared between two trigger modes: the MATLAB trigger mode and the external hardware trigger mode. The SNR of the USF imaging with different EM gain in various thick tissues using a modified ICG-liposome was studied. The USF performances of the modified ICG-liposome and PNIPAM/β-CD/ICG nanogel were also compared.

The last chapter summarizes all the results and concludes this dissertation. Potential problems and future solutions are discussed.

Chapter 2

IN VIVO USF IMAGING USING ICG-PNIPAM NP

2.1 Introduction

Fluorescence imaging has been widely used in many biomedical applications because it can provide tissue functional and molecular information [40, 41]. It has high sensitivity and specificity with benefits of low cost, use of non-ionizing radiation and capability of multicolor imaging. However, fluorescence imaging suffers from limitations caused by the high scattering property of tissues in different applications [40-43]. For example, fluorescence microscopy has a high spatial resolution (sub-microns) but is limited in imaging depth (<1 mm). Fluorescence diffuse optical tomography can image tissue as deep as several centimeters but is limited by poor spatial resolution (a few millimeters).

To address these challenges, several technologies have been or are being investigated, such as ultrasound-modulated fluorescence [12, 13] or luminescence [44], ultrasound-induced temperature-controlled fluorescence [16-18] or luminescence [45], and time-reversed ultrasonically encoded optical focusing [19-23]. During the past years, we have developed a new hybrid imaging technique, USF imaging, to achieve high resolution fluorescence imaging in centimeters-deep tissue [18, 24-27].

Although the results are promising from the technologies mentioned above, all of them are still in their early or concept development stage, and all the results are demonstrated in tissue-mimic phantoms (such as highly optical scattering intralipid solution or gels) or tissue samples (such as chicken breast tissues or porcine muscle tissues). Significant technical challenges hinder their use in real *in vivo* applications. To achieve those potential biomedical applications via fluorescence contrast, it is important to demonstrate the *in vivo* imaging feasibility and validate the accuracy. In this study, overcoming the technical barriers, we, for the first time, successfully demonstrate *in vivo* USF imaging in mice and validate the results by micro-CT imaging. The success of *in vivo* USF imaging is an important step to push this technology for future applications.

2.2 Materials and Methods

2.2.1 Characterization of the ICG-PNIPAM NPs

The ICG-PNIPAM NPs used in this study were synthesized according to the previously proposed protocol [31]. The method measuring the fluorescence intensity of the ICG-PNIPAM NPs as a function of temperature was described in our previous study [36]. To measure the size of the ICG-PNIPAM NP, a 50 μL ICG-PNIPAM NP sample

was diluted with 3 mL deionized water. A dynamic light scattering system (ZetaPALS, Brookhaven Instruments Corporation, NY, USA) was used to measure the hydrodynamic size of nanoparticles at 25 °C.

To measure the concentration of the ICG-PNIPAM NP, a freeze dryer (FreeZone, Labconco, Kansas City, MO, USA) was used to freeze dry 15 mL nanoparticles solution with a vacuum at 0.01 mBar and a temperature of -50 ˚C. Afterwards, the obtained sample was weighed. The concentration of the nanoparticles was calculated by using the following equation:

$$Nanoparticle\ Concentration\ (\frac{mg}{ml}) = \frac{Mass\ of\ the\ sample\ after\ freeze\ dry\ (mg)}{Volume\ of\ the\ sample\ used\ to\ freeze\ dry\ (ml)}$$

which gave a result of 24.60 mg/mL.

2.2.2 USF Imaging System

The USF imaging system was similar to the one described in our previous study [25]. A function generator (FG, 33220A, Agilent, Santa Clara, CA, USA) was used to modulate the intensity of the excitation laser (808 nm, MGL-II-808-2W, Dragon lasers, JL, China) into a 1 kHz sinusoidal wave and also provided a synchronized 1 kHz reference signal for the LIA (SR830, Stanford Research Systems, Sunnyvale, CA, USA). The modulated light passed through a band-pass filter (FF01-785/62-25, Semrock Inc., Rochester, NY, USA) and illuminated the sample. The light intensity reached on the tissue's surface was 3.13 mW/cm^2 for porcine muscle tissue phantom, 1.48 mW/cm^2 for the porcine heart tissue phantom, 3.16 mW/cm^2 for the mouse leg, 4.87 mW/cm^2 for the mouse tumor, 2.87 mW/cm^2 for the spleen in the living mouse, and 3.67 mW/cm^2 for the *ex vivo* spleen in the porcine heart tissue phantom. These numbers are calculated based on the illumination area and the measured optical power (via a power and energy meter, PM100D, Thorlabs Inc. Newton, NJ, USA). The emitted fluorescence from the sample was collected by a fiber bundle and filtered by a set of emission filters, two long-pass filters (BLP01-830R, Semrock Inc., Rochester, NY, USA) and two absorptive filters (FSR-RG830, Newport Corporation, Irvine, CA, USA). It was finally focused on a cooled PMT (H7422-20 driven by a high-voltage source C8137-02, Hamamatsu, Japan) and converted into an electronic signal with a 1 kHz frequency. This 1 kHz signal was then amplified by a low-noise current preamplifier (SR570, Stanford Research Systems, Sunnyvale, CA, USA) and sent into the LIA. A HIFU transducer (2.5 MHz, H-108, Sonic Concepts Inc., Bothell, Washington, USA) driven by another function generator (33500B, Keysight Technologies, Santa Rosa, CA, USA) was used to switch on/off the USF contrast agent. The driving signal was amplified by a RF-AMP (325LA, E&I, Rochester, NY, USA). The amplified signal was delivered to an MNW and then the HIFU transducer to generate

an ultrasonic wave. The triggers from this function generator, which was working in burst mode, were used to control a multifunctional input/output device (I/O, PCIe-6363, National Instruments, Austin, TX, USA) to sample the output signals from the LIA and the preamplifier. A three-axis motorized translation stage (XSlide™ and VXM™, Velmex Inc. Bloomfield, NY, USA) was used to realize the sample scanning. The temperature of the water was controlled by a temperature controller (PTC10, Stanford Research Systems, Sunnyvale, CA, USA) with a heater and a temperature sensor. A magnetic stirrer (11-100-16S, Fisher Scientific, USA) along with a long magnetic bar was used to make the water temperature uniform.

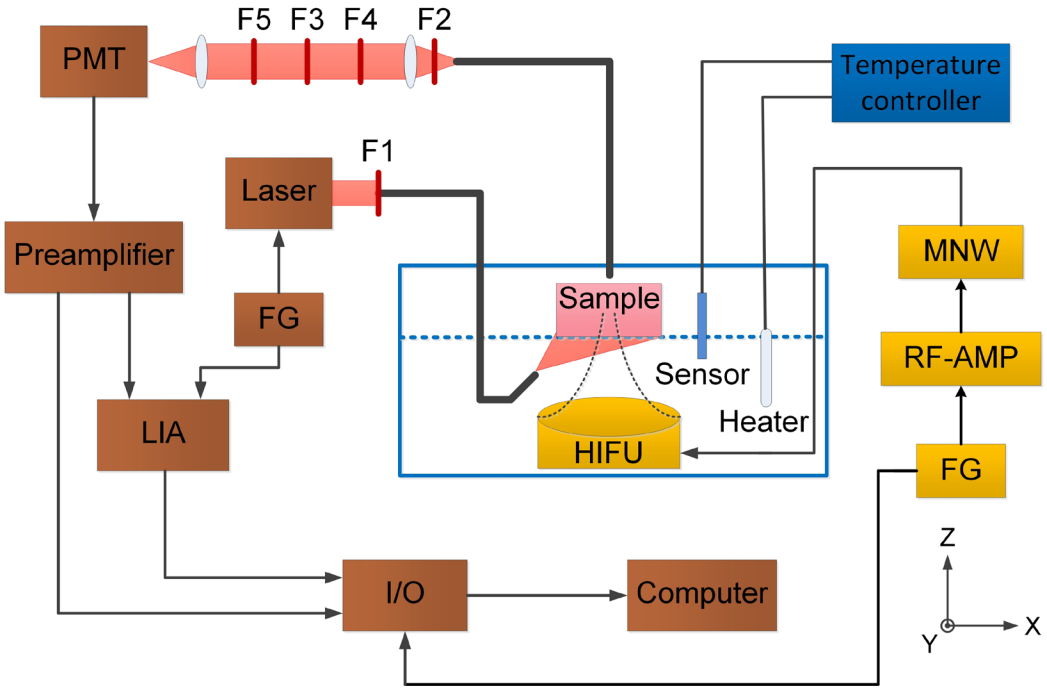

Figure 2-1 The schematic diagram of the USF imaging system. FG: function generator; RF-Amp: radio-frequency power amplifier; MNW: matching network; HIFU: high intensity focused ultrasound; PMT: photomultiplier tube; LIA: lock-in amplifier; F1: excitation filter (785/62 BP); F2–F3: emission filters (830 LP); F4–F5: emission filters (RG 830); I/O: multifunctional input/output device.

2.2.3 Fluorescence Imaging System

The excitation light from a laser (808 nm, MGL-II-808-2W, Dragon lasers, JL, China) driven by a function generator (33220A, Agilent, Santa Clara, CA, USA) passed through an excitation filter (FF01-785/62-25, Semrock Inc., Rochester, NY, USA) to illuminate the sample. The emitted fluorescence signal from the sample was filtered by a set of emission filters (four long-pass filters (two BLP01-830R-50 and two BLP01-830R-25, Semrock Inc.,

Rochester, NY, USA) and an absorptive filter (FSRRG830, Newport Corporation, Irvine, CA, USA)), passed through a camera lens (35mm fixed-focal-length lens, Edmund Optics Inc., Barrington, NJ, USA) and was received by an EMCCD camera (ProEM®-HS:1024BX3, Princeton Instruments, Trenton, NJ, USA).

2.2.4 Sample Configuration Protocol of the Silicone Tube-Embedded Porcine Muscle Tissue and the Heart Tissue

A silicone tube (ST 60-011-01, Helix Medical, Carpinteria, CA, USA) was inserted into a piece of porcine muscular tissue with a thickness of 1 cm at a depth of 5 mm from the bottom. To prepare the heart tissue, the USF contrast agent (ICG-PNIPAM NP) with an LCST of ~24–25 °C was mixed a commercial CT contrast agent (ExiTronTM nano 12000, Miltenyi Biotec, Bergisch Gladbach, Germany) with a ratio of 3:1 first. The 50μL mixed contrast agents were then locally injected into the heart tissue with a thickness of 1 cm to form a single point. The tissue (heart tissue or porcine muscle tissue) was placed on the transparent parafilm (PM-992, BEMIS Company Inc. Neenah, WI, USA), which sealed the rectangular window of a small tank. The gap between the bottom side of the tissue and the parafilm was filled with ultrasound gel (01-08, Aquasonic 100, Parker Laboratories Inc., Fairfield, NJ, USA) to maintain appropriate ultrasound coupling. The surface of the tissue was also covered with the ultrasound conductive gel and of the transparent parafilm to prevent it from drying during the experiment.

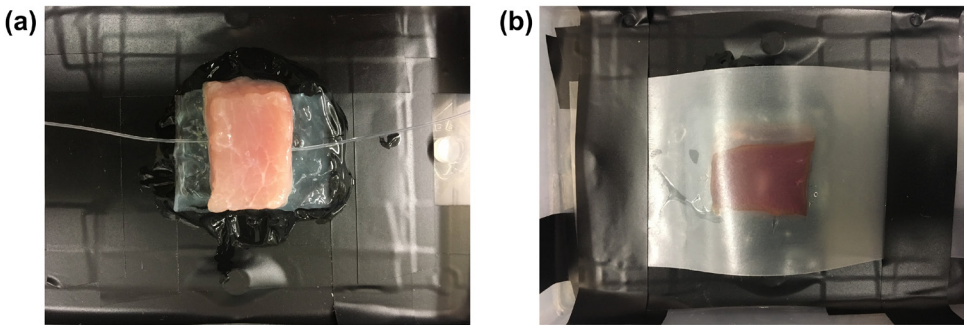

Figure 2-2 Sample configuration of tissues. (a) Tube embedded porcine muscle tissue and (b) porcine heart tissue.

2.2.5 Measuring the Temperature Increase in Silicone Phantom and Porcine Heart Tissue.

Both the silicone phantom and porcine heart tissue had a thickness of 7 mm and were placed on the parafilm. The gap between the lower surface and parafilm was filled with ultrasound gel, while the phantom's upper surface was exposed to air. The HIFU with a center frequency of 2.5 MHz was positioned under the phantom, but the ultrasound wave was focused on the upper surface of the phantom. An infrared (IR) camera (FLIR A300, FLIR Systems, Wilsonville, Oregon, USA) with a frame rate of 20 Hz was positioned on the top of the phantom and was

used to record the temperature distribution on the upper surface of the phantom. The ultrasound exposure time was 400 ms under a driving voltage of 200 mV (~4.82W ultrasound power).

2.2.6 In vivo USF Imaging in Mouse Tumor

The mouse (female, 55 weeks) of strain FVB/N-Tg (MMTVneu) 202Mul/J purchased from Jackson Lab (Bar Harbor, ME, USA) was used for this experiment. The mouse was initially anesthetized with a concentration of 2.5% isoflurane (ISOSOL ISOFLURANE, Miller Veterinary Supply, Ft. Worth, TX, USA) at a flow rate of 1 liter/min for animal preparation. The hair on the tumor surface was removed. A temperature image of the whole mouse body was taken by an IR camera. Afterwards, the 120 μL mixed contrast agents (90 μL ICG-PNIPAM NP with an LCST of ~35–36 °C and 30 μL ExiTron nano 12000) were locally injected into the mouse's breast tumor. The mouse then underwent USF imaging via the FD-USF imaging system. The mouse tumor was placed on the parafilm, which was covered by ultrasound gel (Figure 2-3(a)). To realize long time anesthesia of the mouse, the concentration and the flow rate were reduced to 1.8% and 0.8 liters/min during USF imaging, respectively. To maintain the mouse body temperature, the water temperature in the large tank was kept at 38°C. To determine the scan area, the rough location of the contrast agent was scanned by the USF system quickly without ultrasound exposure. The scan area was selected based on the fluorescence distribution. After USF imaging was completed, the mouse was sacrificed. A 2D planar fluorescence image (excitation/emission: 808/830 nm) was immediately acquired after the mouse's death because the body posture had not been changed at that time. The dead mouse was then scanned by a commercial micro-CT system (Skyscan 1178, Bruker, Kontich, Belgium).

2.2.7 Comparison of USF Imaging in Living and Dead Mouse.

A mouse (female, 9 weeks) of strain BALB/C purchased from Jackson Laboratory (Bar Harbor, ME, USA) was used for this experiment. The hair on the mouse's right hind leg was removed. A temperature image of the whole mouse body was taken by an IR camera. The 70 μL mixed contrast agents (52.5 μL ICG-PNIPAM NP with an LCST of ~35–36 °C and 17.5 μL ExiTron nano 12000) were locally injected into the mouse's right hind leg. An area of 5.08 × 5.08 mm^2 was raster scanned by the HIFU transducer with a driving voltage of 120 mV (~1.74 W of ultrasound power) and an exposure time of 400 ms. The lateral step size was 0.508 mm, and the axial step size was 1.27 mm. The light intensity illuminating the tissue was 1.39 mW/cm^2. Two USF scans were conducted at the same location in a

mouse before and after its death (Figure 2-3(b)). After USF imaging, a temperature image of the dead mouse was then taken by an IR camera.

2.2.8 The Biodistribution of the ICG-PNIPAM NP in Mice.

Mice (female, 7–8 weeks, 17g) of strain BALB/C purchased from Jackson Laboratory (Bar Harbor, ME, USA) were used for this experiment. The mouse was anesthetized with 2.5% isoflurane at a flow rate of 1 liter/min initially, and the hair on the whole-body surface was removed. 120 μL ICG-PNIPAM NP with an LCST of ~35–36°C was injected into mouse body via the tail vein, which corresponded to a 173.65 mg/kg dose of ICG-PINPAM NP. Fluorescence imaging (excitation/emission: 808/830 nm) was carried out at various time points—i.e., 0, 1, 2, 4, 6, 8, 10, 24, 48, 72, 96, 144, 216, 336, 672 hours (h) after the intravenous injection.

2.2.9 In vivo and Ex vivo USF Imaging of Mouse Spleen

A BALB/c mouse (female, 7 weeks, 16g) purchased from Jackson Laboratory (Bar Harbor, ME, USA) was used for this experiment. ICG-PINPAM NP with an LCST of ~35–36 °C and ExiTron nano 12000 were mixed together with a volume ratio of 2:1. The mouse was injected with 150 μL mixed contrast agents via the tail vein, which corresponded to a 153.75 mg/kg dose of ICG-PINPAM NP. The 2D planar fluorescence images of the whole mouse body were taken at 0 and 3 h after the injection. Afterwards, the mouse was placed on the transparent parafilm covered by ultrasound gel with the left side of the body upward for USF imaging (Figure 2-3(c)). The USF imaging was started at 4 h after the intravenous injection since it took about one hour to prepare the experiment. After the USF imaging and sacrifice of the animal, another 2D planar fluorescence image of the dead mouse was taken at about 9 h after the intravenous injection. The dead mouse was then scanned by the micro-CT system. After CT imaging, the main organs (heart, liver, spleen, kidney, stomach, small intestine, and large intestine) were dissected and put on a parafilm. These *ex vivo* organs were immediately imaged using the 2D planar fluorescence imaging system and the CT imaging system. The spleen was then inserted into a piece of porcine heart tissue with a thickness of 1 cm for *ex vivo* USF imaging. The spleen was placed near the top of the heart tissue to simulate the situation when the spleen was in the mouse body. The 2D planar fluorescence imaging, USF imaging, and CT imaging of the heart tissue with spleen inside were carried out in sequence. To realize *ex vivo* USF imaging, the water temperature was kept at 37 °C.

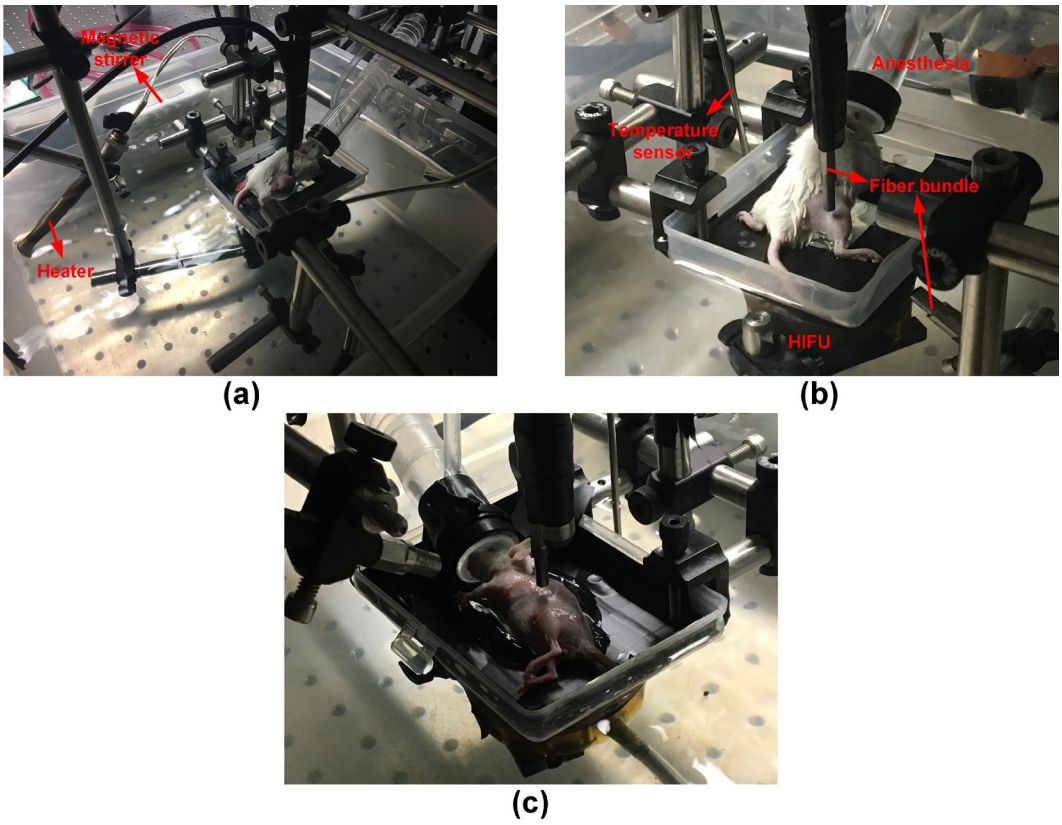

Figure 2-3 Photos to show the animal setup in the *in vivo* USF imaging experiments: (a) in the experiment of imaging mouse tumor; (b) in the experiment of imaging mouse leg; (c) in the experiment of imaging *in vivo* spleen after intravenous injection.

2.2.10 USF Image Processing

Figure 2-4 shown here is based on the experimental data of the *in vivo* USF imaging of the mouse spleen. Figure 2-4(a) shows the raw USF signal output from the lock-in amplifier (the blue line). The oscillation is caused by the mouse breathing. By fitting the raw USF signal via a polynomial fitting, the USF signal is smoothed (the red line). After fitting, the USF signal strength, defined as the maximum value of the fitted signal in the range of 2 to 5 s, can be acquired for each location. A USF image can be formed after a 2D or 3D scanning. As an example, Figure 2-4(c) shows a 2D image representing the USF signal strength distribution and therefore the distribution of the USF contrast agents on the XY plane.

To remove some obvious noises or artifacts, in each experiment, the shapes of all the fitted USF data were evaluated, and three typical fitted USF signals were selected as the references (Figure 2-4(b)). Thus, each fitted USF signal was correlated with the three references, and three correlation coefficients were calculated for each fitted USF

signal at each location. In this study, based on our experience and observation, we defined noise as none of the three correlation coefficients being greater than 0.8. In other words, to consider a signal as a USF signal, at least one of the three correlation coefficients had to be greater than 0.8. The data in Figure 2-4(c) were processed using this correlation method, and the result is shown in Figure 2-4(d). Clearly, some artifacts caused by noise and mouse breathing were removed by using this correlation method.

After correlation, a 3D USF image could be obtained by combining the multiple layers of the 2D USF images (XY plane). By 3D interpolation, the pixel size of the USF image was reduced to 50.8 μm instead of 762 μm (Figure 2-4(e)). Afterwards, the interpolated 3D USF image was divided into 2D images (YZ plane) used for image segmentation. By segmenting the 2D image that had the maximum intensity value among all the images (YZ plane) using 2D Otsu method [46], a threshold was obtained. All the 2D USF images (YZ plane) were then segmented by applying this threshold. As shown in Figure 2-4(f), some background signals shown in Figure 2-4(e) were removed after the segmentation.

Strictly speaking, the USF signal strength is not in direct proportion to the quantity of contrast agents along the axial direction because of the optical and acoustic attenuation. To compensate for this attenuation, the models describing photon diffusion and acoustic attenuation may be adopted. However, we did not consider these methods for the following reasons: (1) in order to adopt those models many background parameters of the tissue will be needed, such as optical absorption and scattering coefficients and the acoustic attenuation coefficient, which are usually unknown and will make the imaging too complicated; (2) similar to fluorescence confocal or 2-photon microscopy, the current USF system adopts a point-by-point scanning method so that the USF signal strength is directly correlated to the distribution of the contrast agent, although it is not directly equal; (3) the maximum scanning range along the depth direction in this study is 8.128 mm, which is relatively small and the errors caused by natural attenuation along the depth direction may be tolerable; (4) because USF imaging is still in the early development stage, adopting the current method is an efficient way to avoid complicating the methods and results, and more strict methods can be developed in future.

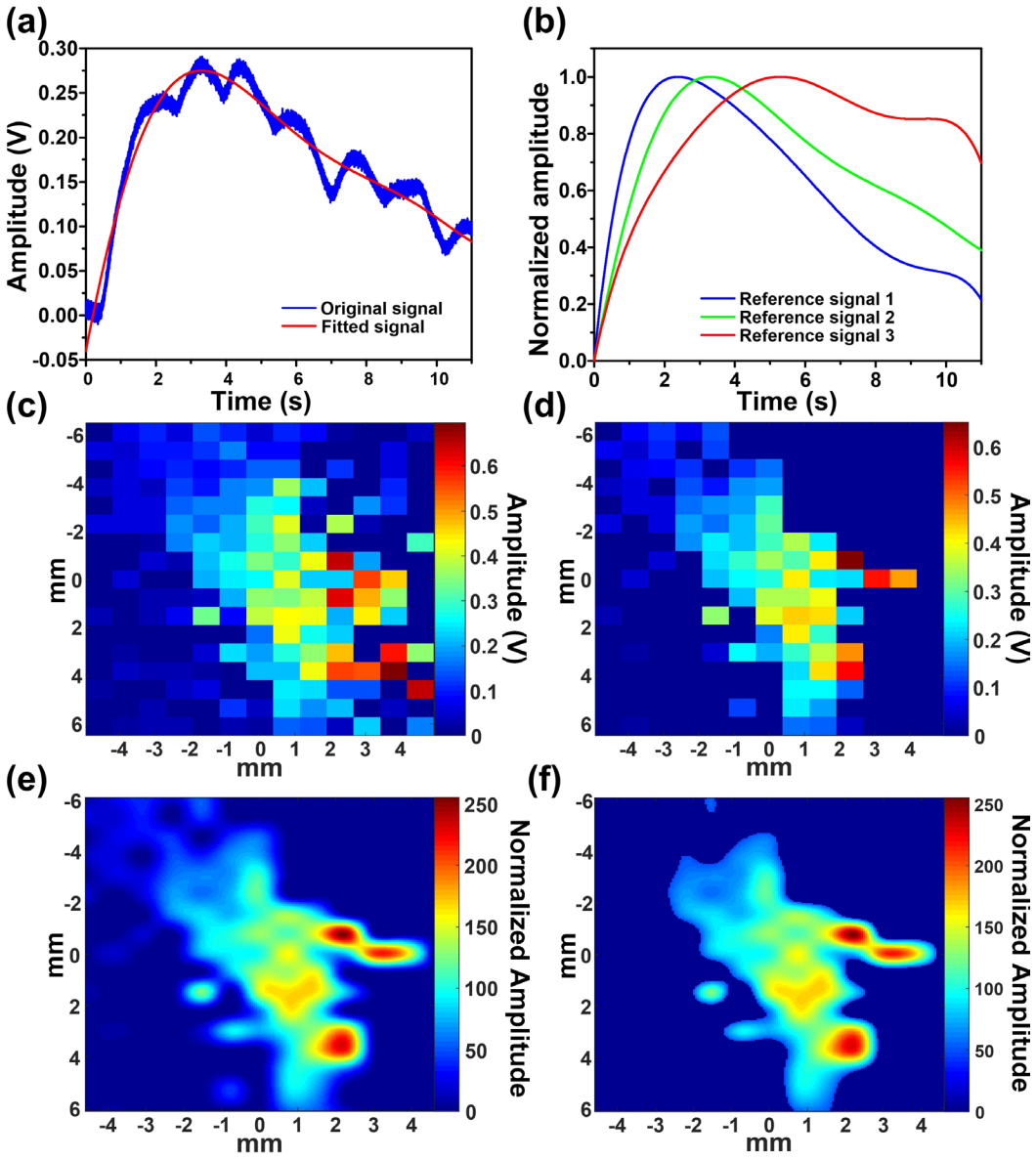

Figure 2-4 USF image processing. (a) Original (blue line) and fitted (red line) USF signal. (b)Three USF fitted curves used as three reference signals for correlation. USF images: (c) before correlation, (d) after correlation, (e) after interpolation based on (d), (f) after image segmentation based on (e).

2.2.11 Co-Registration of USF Image and CT Image

The CT image was reconstructed and processed via the software provided by the micro-CT manufacturer (NRecon and CTAn). The scanning volume in USF imaging was extracted from the reconstructed CT image by comparing the 2D planar fluorescence image with the X-ray projection image of the phantom or the mouse. The 3D CT image and the 3D USF image were co-registered in the software provided by the micro-CT manufacturer

(DataViewer). Because the rough locations of the contrast distribution shown in both imaging modalities were very close to each other, the co-registration was realized by slightly adjusting the angle and location of the objects. The visualization of the 3D images was realized via ParaView (Sandia National Laboratory, Kitware Inc, Los Alamos National Laboratory).

2.3 Results

2.3.1 Characterization of the ICG-PNIPAM NPs

As shown in Figure 2-5(a), the LCST of the ICG-PINPAM NP used for tissue phantom experiments is ~24–25 °C, and for *in vivo* experiments, it is ~35–36 °C. As shown in Figure 2-5(b), the mean and median hydrodynamic diameters of the nanoparticles are 359.2 nm and 334.8 nm, respectively. The polydispersity is 0.151.

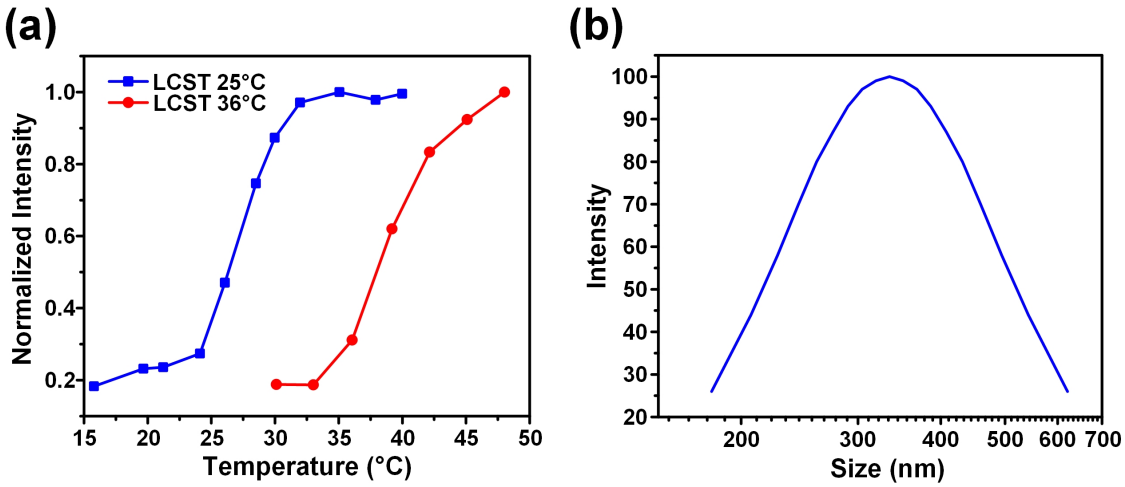

Figure 2-5 (a) Normalized fluorescence intensity of the ICG-PINPAM NP as a function of temperature. (ICG-PINPAM NP with an LCST of ~24–25 °C: blue solid line with square; ICG-PINPAM NP with an LCST of ~35–36 °C: red solid line with circle). (b) Dynamic light scattering of the synthesized ICG-PINPAM NP.

2.3.2 Quantification of the Effect of the Driving Voltage on the Spatial Resolution of USF Imaging in a Silicone Tube-Based Tissue Phantom

To quantify the effect of the driving voltage of HIFU on the spatial resolution of the FD-USF system, we carried out USF imaging using a silicone tube-based tissue phantom. As shown in Figure 2-6(a), a silicone tube (with an inner diameter of 0.31 mm and outer diameter of 0.64 mm) was inserted into a piece of porcine muscular tissue (with a thickness of ~10 mm) at a depth of ~5 mm to simulate a blood vessel. Before USF imaging, the silicone tube was filled with ICG-PINPAM NP with an LCST of ~24–25 °C. To obtain the lateral and axial one-dimensional (1D)

profiles of the tube, a HIFU transducer was used to scan the tube laterally (with a scan range of 6.604 mm and a step size of 127 μm) and axially (with a scan range of 10.16 mm and a step size of 635 μm).

Figure 2-6(b) shows the lateral (i.e., Y direction) 1D USF profiles of the silicone tube using two different HIFU driving voltages of 80 mV and 140 mV from the function generator (i.e., peak-to-peak, Vpp). The peak values of the 1D USF profiles under the two driving voltages of 80 mV and 140 mV are about 267 mV and 626 mV, respectively. The higher driving voltage induces stronger USF signal strength because of the higher HIFU-induced temperature rise. As shown in Figure 2-6(c), the full width at half maximum (FWHM) of the lateral profiles under the two driving voltages are 1.08 mm and 1.39 mm, respectively. Figure 2-6(d) shows that the lateral FWHM of the USF profile of the tube increases with the rising of the HIFU driving voltage (60, 80, 100, 120, 140, 160, and 180 mV and the estimated ultrasound power: 0.43, 0.77, 1.21, 1.74, 2.36, 3.09, 3.90 W). This is because a higher driving voltage can induce a larger thermal focal volume, switch on more contrast agents, and lead to a stronger USF signal and a larger FWHM (i.e., a lower spatial resolution of USF imaging).

As shown in Figure 2-6(e), the peak values of the axial USF profiles (i.e., Z direction) under the two driving voltages of 80 mv and 140 mV are about 207 mV and 661 mV, respectively. As shown in Figure 2-6(f), the FWHM of axial USF profiles under the two driving voltages are 3.31 mm and 5.37 mm, respectively. Figure 2-6(g) shows that the axial FWHM of the USF profile of the silicone tube increases with the rising of the HIFU driving voltage. It should be noted that the axial FWHM is much larger than the lateral FWHM, which is due to the focal zone shape of the HIFU transducer. The axial and lateral FWHMs of the acoustic intensity focus was measured as 2.8 mm and 0.55 mm [33], respectively.

Figure 2-6(h) shows the lateral USF profile of the silicone tube using a driving voltage of 180 mV, and Figure 2-6(i) is the corresponding normalized USF signals as a function of time at different positions of the tube (right). It should be noted that the shapes of the USF signals are different when the HIFU is scanning across the tube (i.e., along the Y direction). The USF signal at the edge of the tube decays more slowly than that at the center of the tube. Due to the thermal diffusion, the USF signal will have a longer duration time than in the focus. Three reference signals chosen for correlation in image processing are based on this observation. It should be noted that the three peak times in Figure 2-4(b) are slightly shifted, which are not in Figure 2-6(i). This is because the ICG-PINPAM NP may be well spread in the spleen, rather than only being confined in the silicone tube in which situation thermal diffusion would affect the shape of the USF signal less significantly.

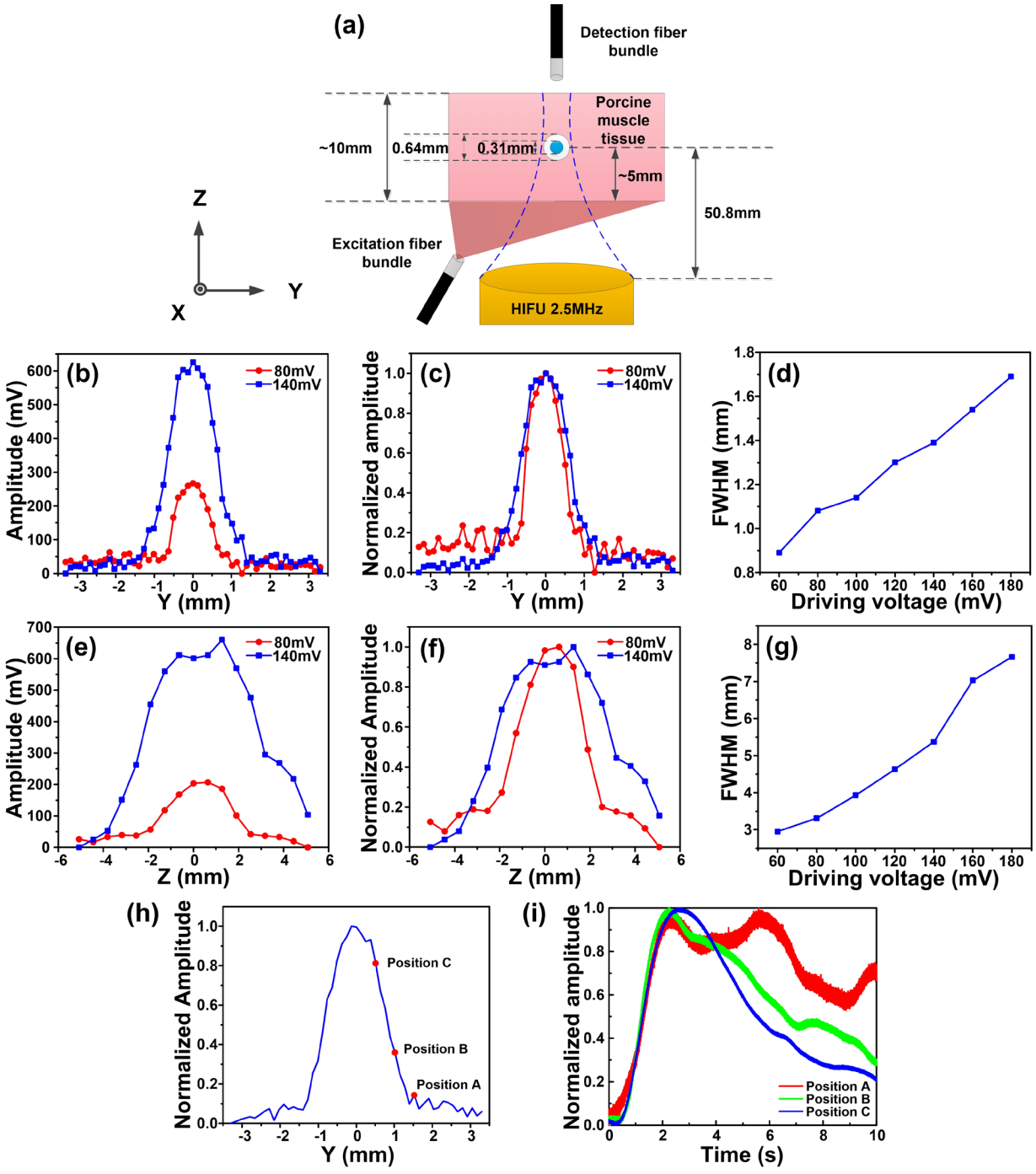

Figure 2-6 (a) The sample configuration, including the porcine muscular tissue, the silicone tube, the excitation and detection fiber bundles, and the HIFU transducer. (b) and (c) are the original and normalized lateral (i.e., Y direction) 1D profiles of the silicone tube using a driving voltage of 80 mV (the red solid line with circles) and 140 mV (the blue solid line with squares), respectively. (d) The lateral FWHMs at different driving voltages. (e) and (f) are the original and normalized axial (i.e., Z direction) 1D profiles of the silicone tube using a driving voltage of 80 mV (the red solid

line with circles) and 140 mV (the blue solid line with squares), respectively. (g) The axial FWHMs at different driving voltages. (h) The lateral 1D profile of the silicone tube using a driving voltage of 180 mV, and (i) the corresponding USF signals as a function of time at the position A (the red line), the position B (the green line) and the position C (the blue line).

2.3.3 USF Imaging of the Contrast Agent Distribution in the Porcine Heart Tissue via a Local Injection

Figure 2-7(a) is a white-light photo of the porcine heart tissue (with a thickness of 10 mm). The USF contrast agent (37.5 μL) was mixed with the contrast agent of the CT (12.5 μL), and the mixed solution was locally injected into the heart tissue to form a single spot. Figure 2-7(b) shows the normalized 2D fluorescence intensity distribution on the tissue top surface (i.e., on the XY plane). The image was acquired via an EMCCD camera, the excitation light has a central wavelength of 808 nm, and the emission detection is >830 nm. The red box shows the scan area of USF imaging on the XY plane. A volume of 9.144 × 9.144 × 7.620 mm^3 was raster scanned by the HIFU transducer using a driving voltage of 120 mV. The lateral step size was 0.762 mm, and the axial step size was 1.524 mm. The 2D USF images shown in Figures 2-7(c1–c6) indicate the distribution of USF contrast agent on XY plane at different depths (i.e., Z direction). Figures 2-7(d1–d3) show the top view (XY plane), right view (YZ plane), and front view (XZ plane) of the reconstructed 3D CT image indicating the CT contrast agent distribution, respectively. Similarly, Figures 2-7(e1–e3) show the top view, right view, and front view of the 3D USF image indicating the USF contrast agent distribution, respectively. Figure 2-7(f1) shows the co-registered 3D image of the two modalities, and Figures 2-7(f2–f5) are the 2D cross-section images on the XY plane at different depths. The blue volumes or areas show the CT contrast agent distribution only, and the green ones indicate the USF contrast agent distribution only. The red ones represent the overlap parts between the two contrast agent distributions.

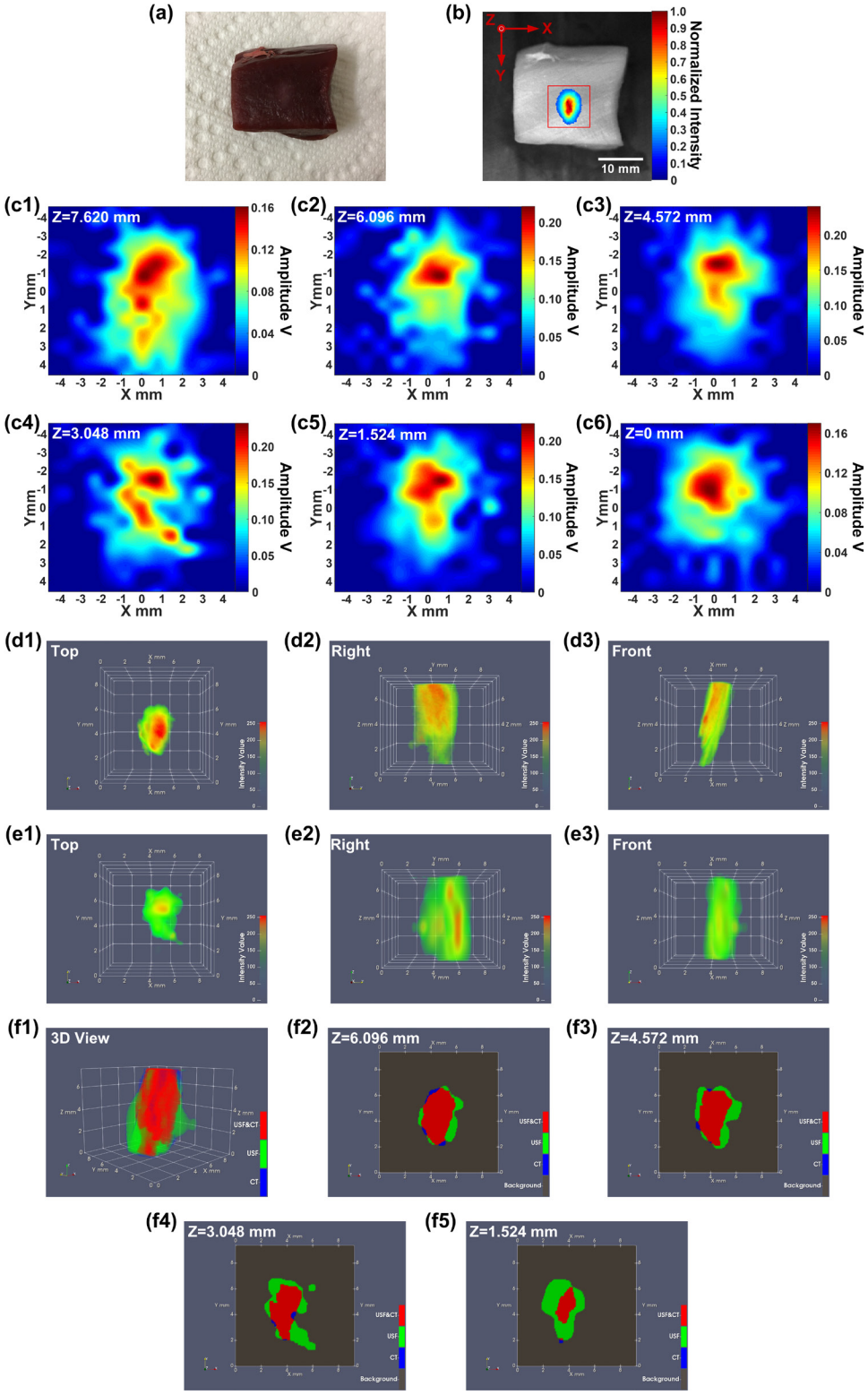

Figure 2-7 (a) A white-light photo of the porcine heart tissue. (b) The fluorescence image (Ex/Em=808/830 nm) of the mixed contrast agents distribution in the tissue. The red square represents the scan area of USF imaging on the XY

plane. (c1–c6) 2D USF images on the transverse (XY) plane at different depths. (d1–d3) The top view (XY), right view (YZ), and front view (XZ) of the reconstructed 3D CT image. (e1–e3) The top view (XY), right view (YZ), and front view (XZ) of the 3D USF image. (f1) The 3D view of the co-registered image of the two modalities, and (f2–f5) the 2D cross-section images on XY plane at different depths.

2.3.4 Measuring the Temperature Increase in Silicone Phantom and Porcine Heart Tissue

The left panel of Figure 2-8(a) shows the temperature dynamic variation after HIFU exposure at the central position where temperature is spatially maximum. The right panel of Figure 2-8(a) shows the 2D temperature distribution on the silicone phantom's upper surface at the time when the peak temperature was reached.

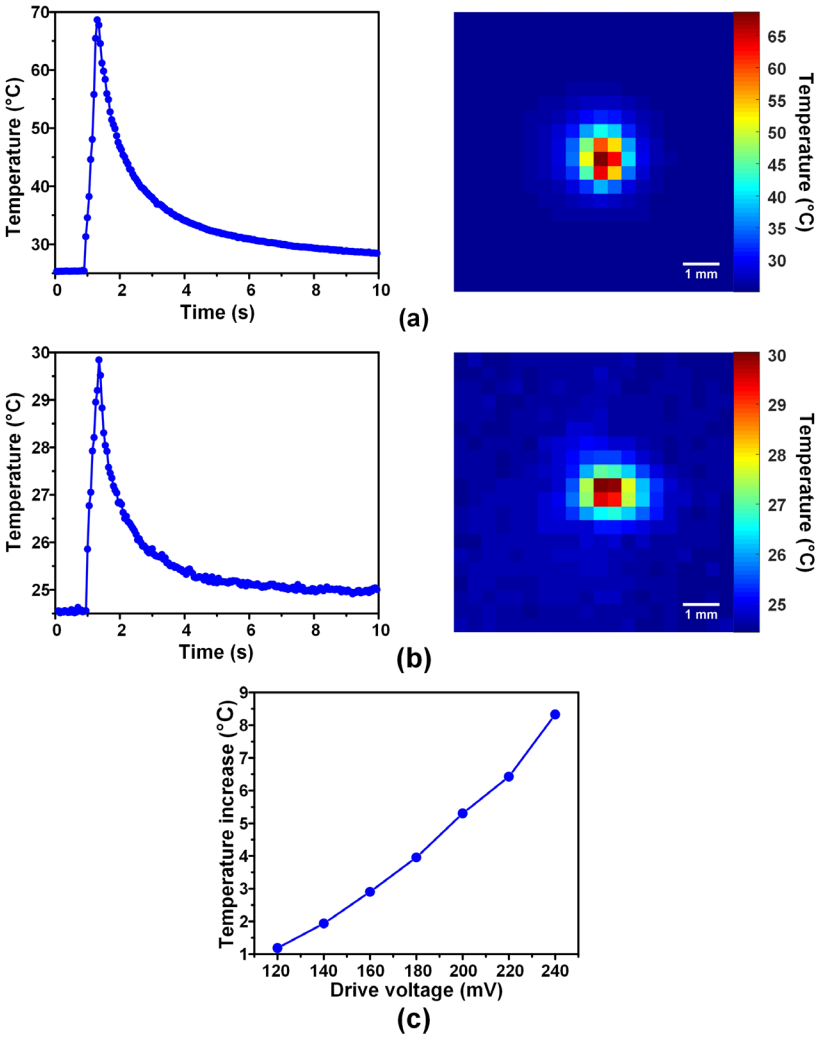

Figure 2-8 Comparison of the temperature rise with 200 mV driving voltage in (a) a silicone phantom and (b) a porcine heart tissue. (c) Temperature rise in the porcine heart tissue as a function of driving voltage.

Figure 2-8(b) shows the corresponding results in the porcine heart tissue. The temperature increases quickly during the ultrasound exposure and decays slowly after the exposure. The absolute values of the peak temperature in the two phantoms are ~68.64 and ~29.84 °C, respectively. The HIFU-induced temperature rise is much more in the silicone phantom (~43.30 °C,) than in the heart tissue (~5.30 °C) with the same driving voltage. This is due to the larger ultrasound absorption coefficient of the silicone. Figure 2-8(c) shows the HIFU-induced temperature rise in the porcine heart tissue as a function of the driving voltage. Obviously, raising the driving voltage increases the temperature rise. A super linear relationship between the driving voltage and the temperature rise can be observed. During USF imaging, it will be difficult to quantify the temperature rise because the IR camera cannot detect temperature inside the tissue. However, the above method and results can provide a rough guideline about the relationship. In this study, to avoid potential thermal damage to the tissue, the temperature rise was limited to a few Celsius degrees by controlling the driving voltage.

2.3.5 Comparison of USF Imaging in Living and Dead Mouse.

Figure 2-9(a) shows the fluorescence 2D planar image (Ex/Em:808/830 nm) in the right hind leg where the contrast agent was injected, and a white-light photo of the mouse is shown on the top right corner. The red box indicates the scan area of the USF imaging on the horizontal plane. Figure 2-9(b) and 2-9(c) show the images of the body temperature before and after the death, respectively. The shell temperature of the living mouse's leg is ~34–35 °C while that of the dead mouse's leg is ~24–25 °C, which is far below the LCST of the ICG-PINPAM NP (~35–36 °C) used in this experiment. Thus, by using the same experimental parameters, a USF image was successfully acquired when the mouse was living (Figure 2-9(d)). In contrast, almost no USF signal was observed from the dead mouse (Figure 2-9(e)). This result shows the importance of matching the background temperature close to the temperature switching threshold (i.e., LCST of the contrast agent).

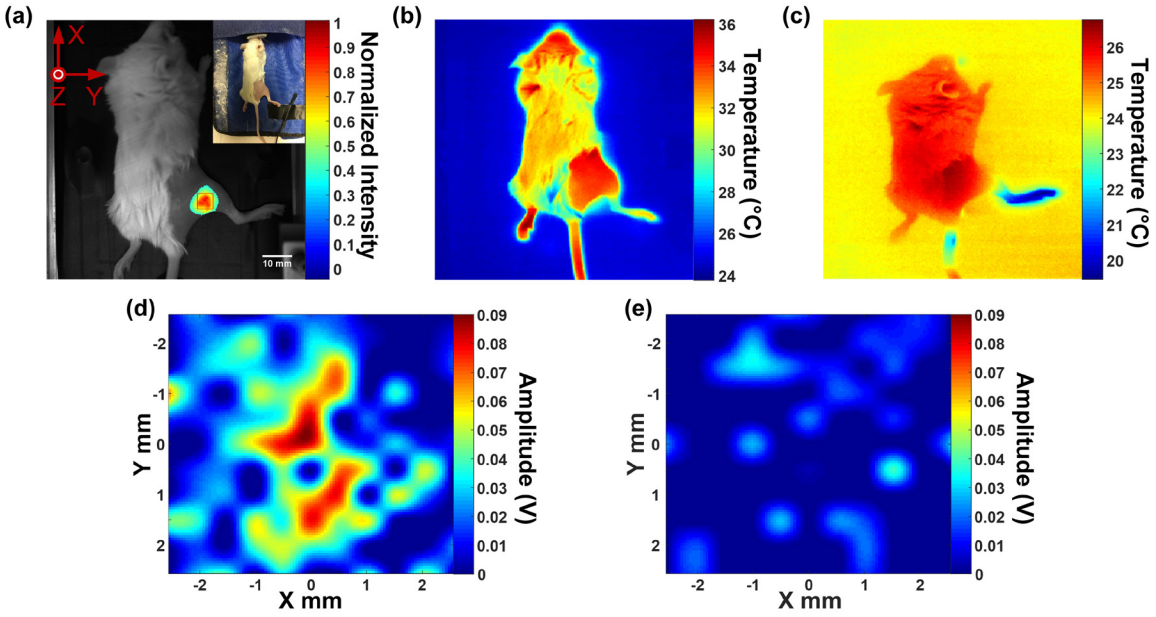

Figure 2-9 Comparison of USF imaging before and after the dead of a mouse. (a) A 2D planar fluorescence image (Ex/Em=808/830 nm) at the location of the injection on the mouse's right hind leg overlapped on a black-and-white photo. The USF scan area on the horizontal plane is indicated by a red square. A white-light photo of the mouse is shown on the upper right corner. The mouse body temperature images: (b) before and (c) after the death. 2D USF images (d) before and (e) after the death.

2.3.6 In vivo USF Imaging of the Contrast Agent Distribution in a Breast Tumor on a Mouse via a Local Injection

Figure 2-10(a) shows the 2D fluorescence planar image (Ex/Em:808/830 nm) of the injected contrast agents in a mouse's breast tumor, and a white-light photo of the mouse is shown on the top right corner. The red box overlaid on the fluorescence image shows the scan area of USF imaging on the XY plane. A volume of 7.112 × 7.112 × 7.620 mm^3 was raster scanned by the HIFU transducer using a driving voltage of 250 mV. The lateral step size was 0.508 mm, and the axial step size was 2.54 mm. Figure 2-10(b) shows the shell temperature of the mouse acquired using an IR camera. Because the shell temperature of the mouse tumor is ~35 °C, the LCST of the USF contrast agent used for this *in vivo* experiment is ~35–36 °C rather than ~24–25 °C, which is suitable for phantom experiments at room temperature. The 2D USF images shown in Figures 2-10(c1–c4) indicate the distribution of the USF contrast agent on XY plane at different depths (i.e., Z direction). Figures 2-10(d1–d3) show the top view (XY), right view (YZ), and front view (XZ) of the reconstructed 3D CT image indicating the CT contrast agent distribution, respectively. Similarly, Figures 2-10(e1–e3) show the top view, right view, and front view of the 3D USF image indicating the USF

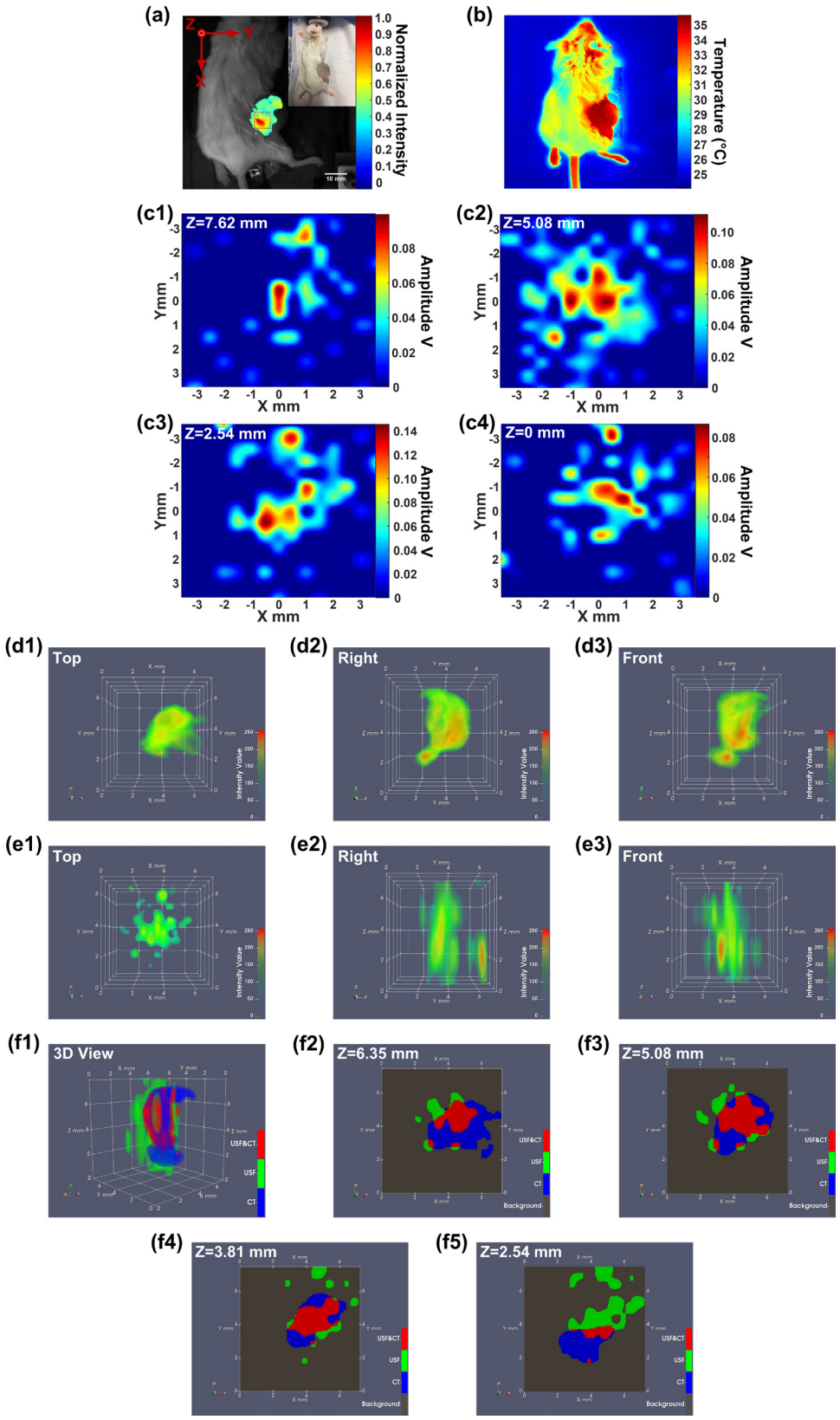
(a)
Z
Y
X
10 mm
Normalized Intensity
1.0
0.9
0.8
0.7
0.6
0.5
0.4
0.3
0.2
0.1
0
(b)
Temperature (°C)
35
34
33
32
31
30
29
28
27
26
25
(c1)
Z=7.62 mm
(c2)
Z=5.08 mm
(c3)
Z=2.54 mm
(c4)
Z=0 mm
Ymm
X mm
Amplitude V
(d1)
Top
(d2)
Right
(d3)
Front
(e1)
Top
(e2)
Right
(e3)
Front
Intensity Value
(f1)
3D View
USF&CT
USF
CT
(f2)
Z=6.35 mm
(f3)
Z=5.08 mm
(f4)
Z=3.81 mm
(f5)
Z=2.54 mm
Background

Figure 2-10 (a) A white-light photo of the mouse with a breast tumor (top-right) and the fluorescence image (Ex/Em=808/830 nm) of the mixed contrast agents locally injected in the tumor. The USF scan area is indicated via a red square on the XY plane. (b) An image of the shell temperature of the mouse acquired via an infrared camera. (c1–c4) 2D USF images on the transverse (XY) plane at different depths. (d1–d3) The top view (XY), right view (YZ), and front view (XZ) of the reconstructed 3D CT image. (e1–e3) The top view (XY), right view (YZ), and front view (XZ) of the 3D USF image. (f1) The 3D view of the co-registered image of the two imaging modalities, and (f2–f5) the 2D cross-section images on the XY plane at different depths.

contrast agent distribution, respectively. Figure 2-10(f1) shows the 3D co-registered USF and CT image, and Figures 2-10(f2–f5) are the cross-section images on the XY plane at different depths.

2.3.7 The Biodistribution of the ICG-PINPAM NP in Mice

Figure 2-11(a) shows the left side of the mouse body. The region where the spleen was located emitted a strong fluorescence signal and reached the highest value at 4 h after the injection. The signal intensity decayed slowly from 6 to 72 h and was below the threshold (0.2) at 216 h. Figure 2-11(b) shows the right side of the mouse body. The region where the kidney and liver were located emitted a moderate fluorescence signal. The intensity stayed near the maximum value between 6 and 72 h and slowly decayed from 72 to 672 h at which time the intensity was below the threshold (0.125). Figure 2-11(c) shows the ventral side of the mouse body. The region where the liver was located emitted a moderate fluorescence signal. The intensity kept increasing slowly from 0 to 72 h and remained stable from 72 to 144 h. After that, the intensity decreased slowly and eventually reached the threshold (0.125) at 672 h. The signals emitted from the region of the liver and kidney had similar intensity but were much weaker than the signal from the spleen region.

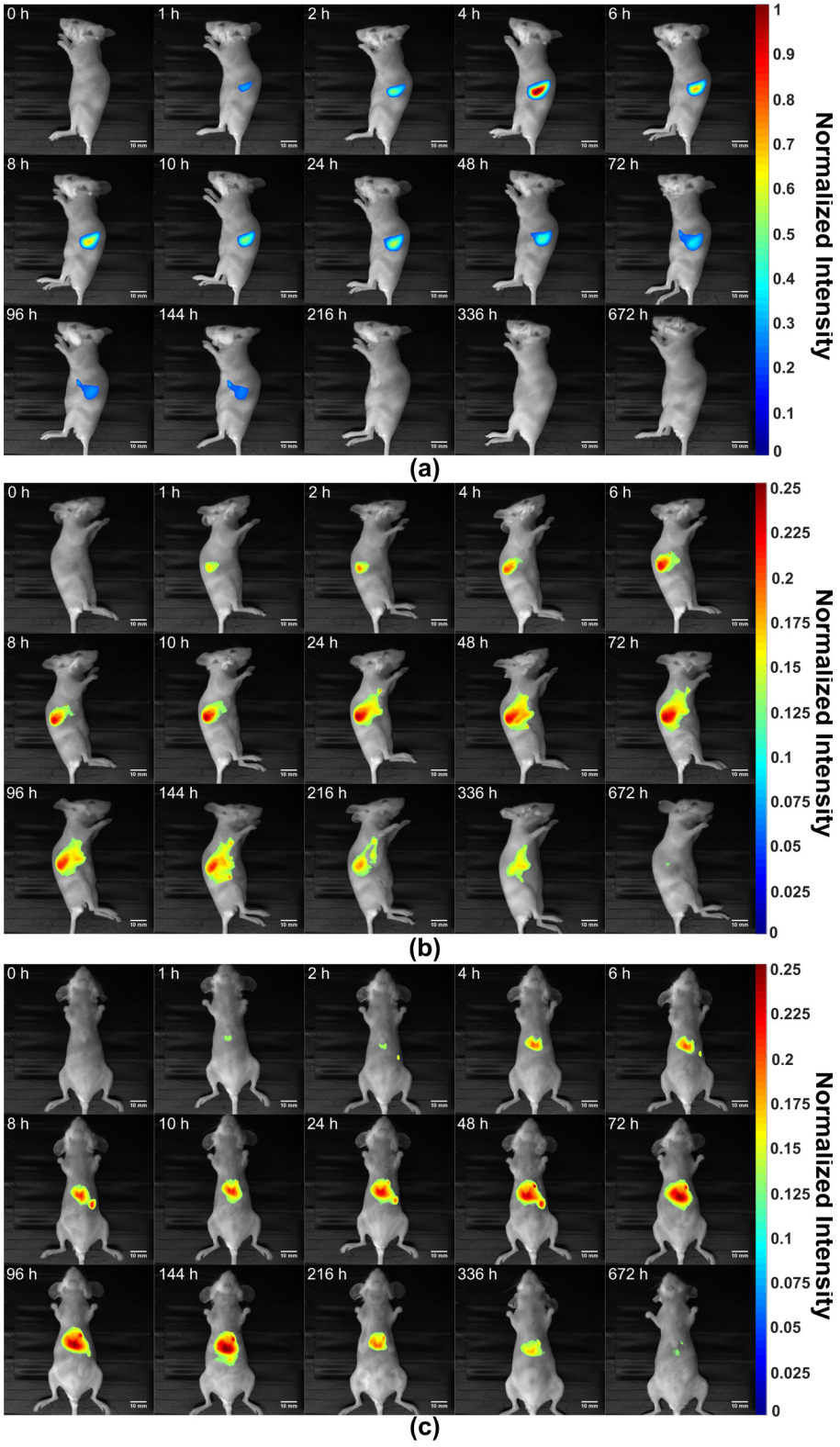

Figure 2-11 Fluorescence images of mouse body at different time points after intravenous injection of ICG-PINPAM NP (Ex/Em=808/830 nm) (a) left side; (b) right side; (c) ventral side.

2.3.8 In vivo USF Imaging of the Contrast Agent Distribution in a Mouse's Spleen via an Intravenous Injection

Figures 2-12(a1–a3) show the fluorescence images (Ex/Em:808/830 nm) of the mouse body at 0, 3 and 9 hours after the intravenous injection of 150 μL mixed contrast agents via the tail vein (100 μL ICG-PINPAM NP with an LCST of ~35–36 °C as USF contrast agent and 50 μL ExiTron nano 12000 as CT contrast agent). The ICG-PINPAM NP were found to be accumulated in the region of the mouse spleen and the fluorescence signal reached to a peak at ~3–4 hours after the intravenous injection. The red box on Figure 2-12(a3) indicates the USF scan area on the XY plane. A volume of 9.144 × 12.192 × 6.096 mm^3 was raster scanned by the HIFU transducer using a driving voltage of 200 mV. The lateral step size was 0.762 mm, and the axial step size was 2.032 mm. The 2D USF images shown in Figures 2-12(b1–b4) indicate the distribution of USF contrast agent on XY plane at different depths (i.e., Z direction). Figures 2-12(c1–c3) show the top view (XY), right view (YZ), and front view (XZ) of the reconstructed 3D CT image indicating the CT contrast agent distribution, respectively. The white dashed lines represent the contours of these spleen CT images. Similarly, Figures 2-12(d1–d3) show the top view, right view, and front view of the 3D USF image indicating the USF contrast agent distribution, respectively. For direct comparison, the same white dashed lines as shown in Figures 2-12(c1–c3) indicating the contours of the spleen CT images were also overlaid on these USF images. Figure 2-12(e1) shows the 3D co-registered USF and CT image, and Figures 2-12(e2–e5) are the cross-section images on XY plane at different depths.

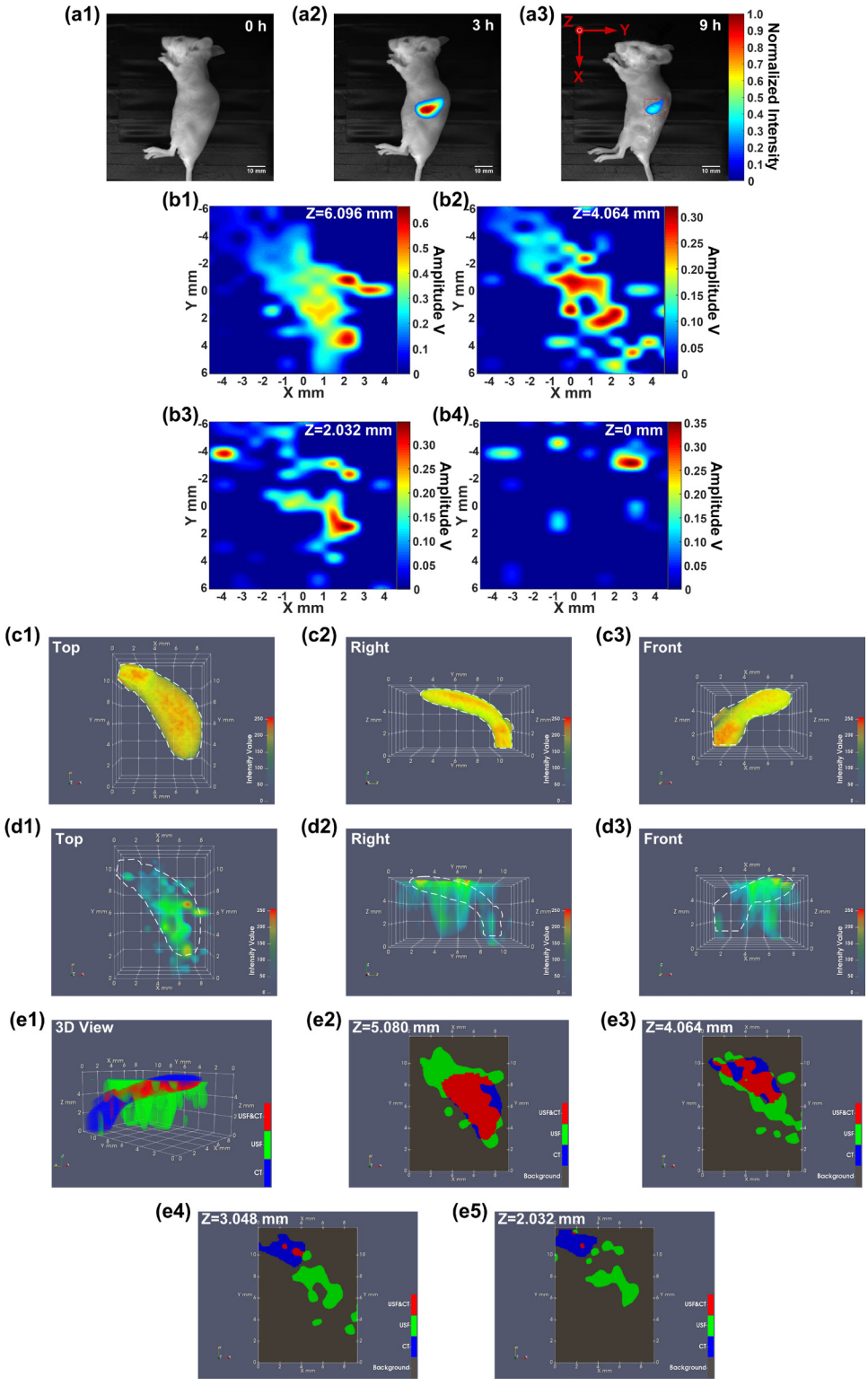

Figure 2-12 (a1–a3) 2D planar fluorescence images of the mouse at different time points after intravenous injection of the mixed contrast agents (Ex/Em=808/830 nm). The red box on the Figure (a3) indicates the USF scan area on the XY plane. (b1–b4) 2D USF images on the transverse (XY) plane at different depths. (c1–c3) The top view (XY), right

view (YZ), and front view (XZ) of the reconstructed 3D CT image. (d1–d3) The top view (XY), right view (YZ), and front view (XZ) of the 3D USF image. (e1) The 3D view of the co-registered image of the two imaging modalities, and (e2–e5) the 2D cross-section images on XY plane at different depths.

2.3.9 Ex vivo USF Imaging of the Mouse's Spleen

To further validate the results of the *in vivo* USF imaging of the mouse spleen, *ex vivo* USF imaging of the mouse spleen was carried out. Figures 2-13(a) is a white-light photo of the major organs of the mouse dissected after the USF imaging. Figures 2-13(b) is the fluorescence image overlaid on the black-and-white image of the organs. As shown in Figures 2-13(b), the fluorescence image (Ex/Em:808/830 nm) of the organs confirmed that most of the ICG-PINPAM NP were accumulated into the spleen as it emitted the strongest fluorescence signal. Also, this figure indicates that the distribution of ICG-PINPAM NP in this spleen may not be uniform because the lower left part of the spleen on this image emits a stronger fluorescence signal than does the upper right part. The stomach, liver, and kidney emit relatively low fluorescence signals. The heart and intestine show no or very weak signals. Figures 2-13(c) shows the reconstructed CT image of the same organs. Similar to the fluorescence image, the spleen also shows the strongest CT signal, and the distribution of the CT contrast agent in the spleen is also not uniform. The liver and some parts of the large intestine show moderate CT signal, and the kidney, heart, stomach, and small intestine all show much weaker CT signals.

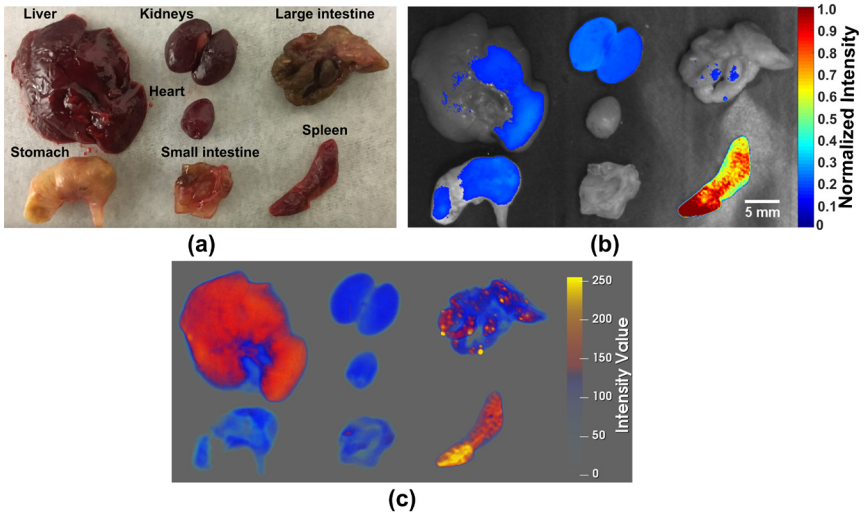

Figure 2-13 Bio-distribution of ICG-PINPAM NP (USF contrast agent) and ExiTron nano 12000 (CT contrast agent) in mice. (a) A white-light photo of the major organs dissected after USF imaging. (b) A 2D planar fluorescence image (Ex/Em=808/830 nm) of the organs. (c) A reconstructed CT image of the organs.

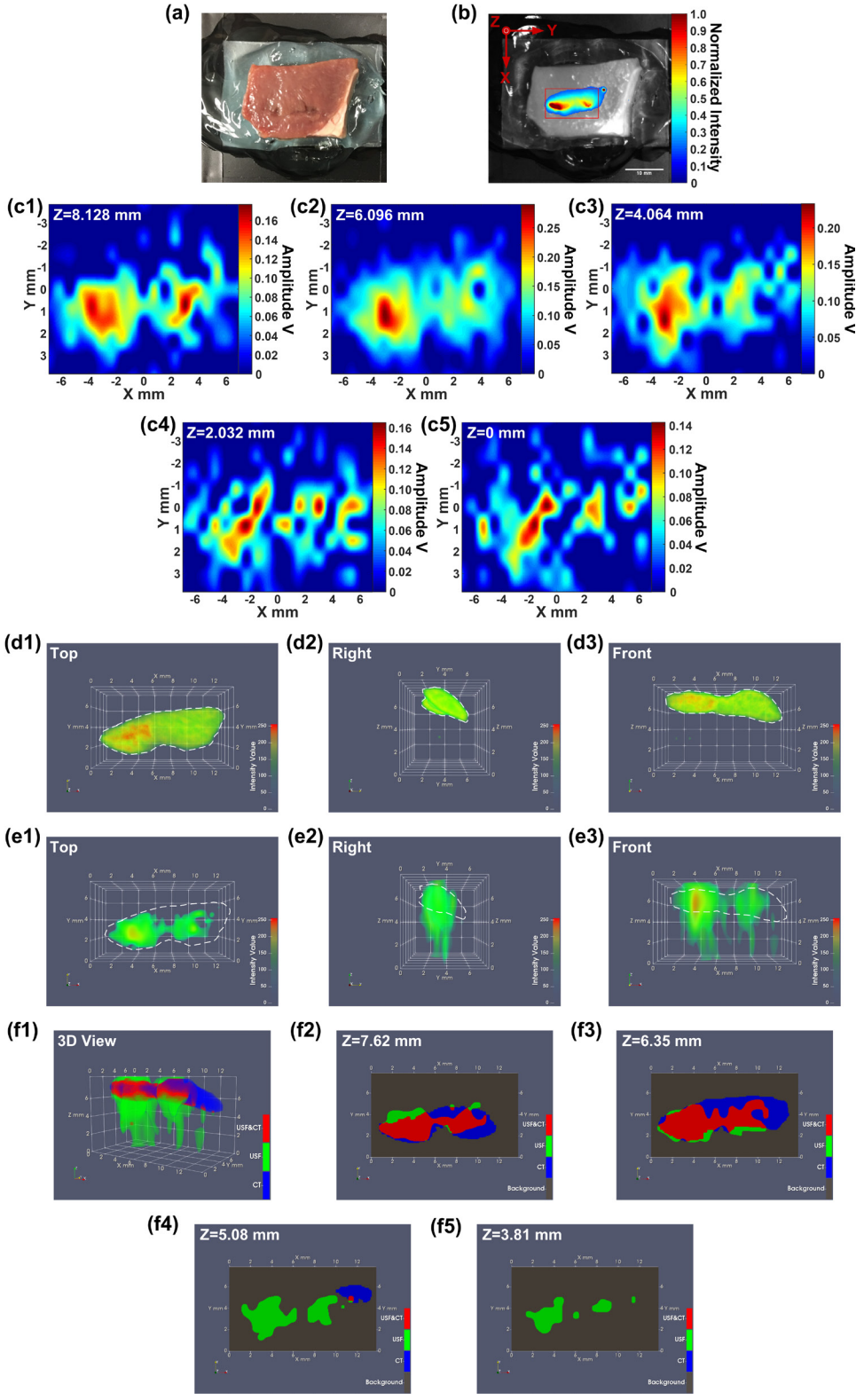

Figure 2-14 (a) A white-light photo of the porcine heart tissue in which the spleen is embedded. (b) The fluorescence image (Ex/Em=808/830 nm) of the tissue and the USF scan area indicated as a red box on the horizontal XY plane.

(c1–c5) 2D USF images on the transverse (XY) plane at different depths. (d1–d3) The top view (XY), right view (YZ), and front view (XZ) of the reconstructed 3D CT image. (e1–e3) The top view (XY), right view (YZ), and front view (XZ) of the 3D USF image. (f1) The 3D view of the co-registered image of the two imaging modalities, and (f2–f5) the 2D cross-section images on XY plane at different depths.

As shown in Figure 2-14(a), to simulate the situation of the spleen inside the mouse body, the spleen was inserted into a piece of porcine heart tissue (with a thickness of 1 cm) in which the spleen was close to the surface. Figure 2-14(b) shows the 2D fluorescence image of the tissue overlaid on a black-white background image. The red box represents the scan area of USF imaging on the XY plane. A volume of 13.716 × 7.620 × 8.128 mm^3 was raster scanned by the HIFU transducer using a driving voltage of 140 mV. The lateral step size was 0.762 mm, and the axial step size was 2.032 mm. The 2D USF images shown in Figures 2-14(c1–c5) indicate the distribution of USF contrast agent on XY plane at different depths (i.e., Z direction). Figures 2-14(d1–d3) show the top view (XY), right view (YZ), and front view (XZ) of the reconstructed 3D CT image indicating the CT contrast agent distribution, respectively. The white dashed lines indicate the contours of the spleen CT images. Similarly, Figures 2-14(e1–e3) show the top view, right view, and front view of the 3D USF image indicating the USF contrast agent distribution, respectively. For direct comparison, the same white dashed lines as shown in Figures 2-14(d1–d3) indicating the contours of the spleen CT images were also overlaid on these USF images. Figure 2-14(f1) shows the 3D co-registered USF and CT image, and Figures 2-14(f2–f5) are the corresponding cross-section images on XY plane at different depths.

2.4 Discussion

2.4.1 HIFU Driving Voltage

Figure 2-6 indicates that raising the HIFU driving voltage will increase the USF signal strength and therefore SNR (Figures 2-6(b) and 2-6(e)) but decrease the spatial resolution (Figures 2-6(d) and 2-6(g)). This is because the higher driving voltage leads to the higher ultrasound power, higher temperature rise, larger thermal focal volume, and therefore more switched-on contrast agents. The driving voltage also varies in different types of tissues due to their different ultrasound absorption abilities. In this study, a total of five different types of tissues were used: (1) tube-embedded porcine muscle tissue, (2) porcine heart tissue, (3) breast tumor in a live mouse, (4) live mouse spleen, and (5) dead mouse spleen. For convenience, the driving voltages applied to these tissues are reorganized in Table 2-1.

Generally, high driving voltage was adopted in live tissues, such as 200 mV in the live spleen and 250 mV in the live tumor; and relatively low driving voltages in dead tissues, such as 140 mV in the dead spleen, 120 mV in the porcine heart tissue, and as low as 60 mV in the tube-embedded porcine muscle tissue. The live tissues usually contain much more fluids, such as water and blood, while the dead tissues usually have much less. Water and blood usually have much smaller ultrasound absorption coefficients than the tissues mentioned above (water: 0.002; blood: 0.2; muscle: 1.1, breast: 0.75; fat: 0.48; liver: 0.5 db/MHz/cm) [47]. In addition, flowing blood may partially function as a cooling system. Accordingly, live tissues are more difficult to heat via HIFU than dead tissue. This fact can explain why we adopted 200 mV for the *in vivo* and 140 mV for the *ex vivo* spleen imaging when intravenous injection was applied to both, and 250 mV in live tumor and 120 mV in dead porcine heart tissue when local injections were applied to both. Lastly, comparing the tube-embedded porcine muscle tissue with the porcine heart tissue with local injections, even lower voltage can be used for the former. This could be for two possible reasons. (1) The adopted silicone tube has a much larger ultrasound absorption coefficient than that of biological tissues discussed in this study (Figure 2-8). (2) Another factor that should be considered is the agent dilution due to either the local or intravenous injection. In the tube-based phantom, the stock solution of the USF contrast agent was injected into the tube so no dilution is applied. For local injection, the contrast agent concentration is usually diluted due to natural diffusion of agents in tissue, whereas for intravenous injection, the dilution is due to the relatively large blood or body volume. In addition, to avoid HIFU-induced tissue damage, the temperature increases in real tissue are limited to only a few Celsius degrees under the driving voltages used in this study (Figure 2-8).

Table 2-1 A summary of HIFU driving voltage Vpp in this study.

	Tissue status (dead or live)	Applied HIFU driving voltage Vpp (mV)
Tube embedded porcine muscle tissue (Figure 2-6)	Dead	As low as 60 mV (60, 80, 100, 120, 140, 160, 180)
Porcine heart tissue (Figure 2-7)	Dead	120
In vivo tumor (Figure 2-10)	Live	250
In vivo spleen (Figure 2-12)	Live	200
Ex vivo spleen (Figure 2-14)	Dead	140

2.4.2 Lateral vs. Axial Resolution

The lateral resolution of the USF imaging system is ~3.3–4.5 times better than the axial resolution, which is due to the inherent nonuniform shape of the ultrasound focus (Figure 2-6(d) vs. 2-6(g)). As shown in all the 3D co-registered images, the sizes of the USF images are larger than CT images along the Z direction, which is the transmission direction of the ultrasound (i.e., the axial direction of the HIFU transducer). However, the USF images match well with CT images on the horizontal XY plane, which is the plane orthogonal to the ultrasound transmission direction as shown in the cross-section images of the XY plane (i.e., the lateral direction of the HIFU transducer).

2.4.3 Biodistribution

The biodistribution data indicates that the USF contrast agents are mainly distributed in the spleen and liver. This is because the median hydrodynamic diameter of the nanoparticles is ~335 nm, and the large-sized nanoparticles are more likely to be accumulated in the spleen and liver due to the uptake of macrophages [48]. The two kidneys also show some fluorescence signal, which may be due to the existence of either very small nanoparticles or the residue of free ICG molecules. Currently, it is unclear why the stomach also shows certain fluorescence signal. Similar to the USF contrast agent, the CT contrast agent (ExiTron nano 12000) was mainly found in the spleen and liver. The mean hydrodynamic diameter of the CT contrast agent is ~110 nm, and it mainly accumulates in the liver and spleen due to uptake by macrophages of the liver [49]. The similar biodistribution in the spleen of both contrast agents makes it possible to image this organ via both modalities for comparison.

In this study, we selected the spleen as the target organ because (1) it can accumulate enough contrast agents of both modalities, has a relatively small volume (therefore a relatively high contrast agent concentration), and is close to the skin, which are all helpful to achieve a high SNR. And (2) it has a unique shape and location, which make it easy to be roughly identified and located with a 2D camera. To achieve this goal, we controlled the nanoparticles size relatively large (~335 nm) because large-sized nanoparticles have a better chance of accumulating in the spleen.

2.4.4 The Key Factor to Successfully Achieve In vivo USF Imaging—Stability of USF Contrast Agents in Biological Environments

This is the first time that USF has been demonstrated to successfully image living biological tissues via both local and intravenous injections. It is important to point out that the success of *in vivo* imaging is highly dependent upon the stability of contrast agents in biological environments. The adopted USF contrast agent in this study is ICG-encapsulated PNIPAM-based nanoparticles. The shelf life of the stock solution can be as long as a year or longer

without loss of the switching performance [31]. More importantly, the USF contrast agent adopted in this study shows high stability in biological environments. As described in Methods, the *in vivo* USF imaging of the spleen was conducted between 4 and 9 hours after the intravenous injection, and the *ex vivo* USF imaging was conducted 1 day after the intravenous injection. These data clearly indicated that the switching property of the contrast agents was well maintained no matter whether in living or dead tissue. In addition, we believe that the temperature-switching threshold of the adopted contrast agent was maintained the same in both living and dead spleen as the value measured in vitro (such as in a cuvette). This conclusion is drawn based on the following two facts: (1) to be able to observe a similar USF signal in the dead tissue to that in living tissue, the background temperature of the dead tissue needs to be raised up to around 37 ℃ (similar to the living mouse body temperature) via a water bath; (2) without heating the dead tissue, almost no USF signal can be observed from the dead tissue (Figure 2-9).

2.4.5 Current Technical Limitations and Future Directions

Currently the on-to-off ratio of the adopted ICG-PINPAM NP is ~5, which is enough for *in vivo* USF imaging in this study and may be able to further improve in future by optimizing the synthesis protocols. Using a contrast agent with a higher on-to-off ratio may improve the SNR and therefore possibly reduce the required driving voltage or ultrasound power.

The contrast agent distribution appears discrete in the XY plane and stretched along the Z axis. The factors causing this issue are as follows. First, the SNR of the *in vivo* USF imaging was not as high as that in phantoms. This is because the contrast agent is highly diluted by the blood, and there are some motion artifacts caused by the mouse breathing. Second, the ultrasound might be blocked by other organs and ribs during the propagation towards spleen. Third, the axial resolution is worse than the lateral resolution, which causes that some USF signals are shown in the bottom layers below the spleen.

The non-uniform spatial resolutions have been partially addressed in our recent work by using two 90^0-crossed confocal HIFU transducers [26]. Further development and implementation need to be conducted in future. Another technical limitation of current USF imaging systems is the speed. Because it is a point-by-point scanning imaging technology and adopts the HIFU-induced temperature to switch on fluorescence, it usually takes a few hours to finish a 3D image acquisition. Currently, we are developing and testing several strategies to increase the imaging speed, such as via camera-based fast scanning techniques, and we expect the imaging speed to increase significantly if successful. It is highly desirable to develop new USF contrast agents that have better switching performance (such

as high on-to-off ratio, narrow-switching bandwidth, in near-infrared region, etc.), are feasible for molecular targeting and multicolor imaging, and are biocompatible and biodegradable. Currently, because of the use of the large sized and non-targeting nanoparticles, the accumulation of ICG-PINPAM NP in the mouse tumor after intravenous injection via the conventional enhanced permeability and retention (EPR) effect is weak and not enough for USF imaging. Using smaller sized and/or functionalized nanoparticles may increase the accumulation of nanoparticles in a tumor [50]. With the success of addressing these technical challenges and approvals of various regulations in the future, we expect that USF imaging technique will be a promising, unique, and powerful technology for preclinical and clinical applications to complement the existing imaging technologies.

2.5 Conclusion

For the first time, we successfully achieved the goal of *in vivo* USF imaging via both local and intravenous injections in mice. The USF contrast agent adopted in this study, ICG-encapsulated PNIPAM nanoparticles, was proved to be stable in biological environments (such as in breast tumor and spleen). Biodistribution studies showed that the contrast agent was mainly accumulated in the spleen of mice. It provided a good opportunity to conduct *in vivo* USF imaging. All the USF images were compared with CT images. The results showed that USF achieved similar accuracy to CT on the lateral plane (i.e., the horizontal XY plane orthogonal to the direction of the ultrasound wave propagation), and lower accuracy than CT in the axial direction (i.e., the direction of the ultrasound wave propagation). In addition, USF maintained high sensitivity and specificity to its contrast agents in deep tissues because the signals could be generated only from the contrast agents, and therefore USF was insensitive to non-specific background photons (or noises). With the success of *in vivo* USF imaging, we believe that many potential biomedical applications can be explored in future. The work in this chapter has been published in Scientific Reports [51].

Chapter 3

USF IMAGING VIA AN EMCCD CAMERA AND A Z-SCAN METHOD

3.1 Introduction

To achieve high resolution fluorescence imaging in centimeter-deep tissue, many techniques based on ultrasound mediated fluorescence emission have been investigated recently [16, 18, 24-27, 31, 52-56]. In general, the basis for improving spatial resolution in these approaches is to confine the fluorescence emission to a small volume, the size of which depends on the ultrasound frequency. However, the volume where the desired signal comes from is relatively small compared to the total fluorophore distribution, which not only requires high fluorescence emission efficiency of the contrast agent and sensitivity of the imaging system, but also needs to increase the detection specificity and reduce the noise which means the signal photons should be exclusively differentiated from other background photons.

Recently, we developed a new hybrid imaging modality, USF imaging, to address above challenges [18, 24-27, 31]. USF has a much higher signal-to-noise ratio than ultrasound-modulated fluorescence methods, which were restricted by the low ultrasound modulation efficiency [54-56]. The unique USF contrast agent and the sensitive USF imaging system were critical. We had developed several USF imaging systems before [18, 24-27]. Thanks to the use of modulated excitation light and lock-in amplifier, the sensitivity of the FD-USF imaging system [25] was significantly improved compared to the continuous-wave USF imaging system [24]. However, all the systems used a fiber bundle to collect the emitted fluorescence photons from the sample, which suffered from a low photon collection efficiency. Additionally, attention must be paid when scanning tissue with an uneven surface (such as a mouse). Moreover, the imaging speed was limited by the time required to cool the tissue to minimize the thermal diffusion effect between the two adjacent locations in the scanning sequence.

In this study, we developed a camera-based USF imaging system to overcome the above limitations. An EMCCD camera was used to receive the emitted photons instead of the fiber bundle, which improved the collection efficiency and left enough space between the sample and the detector. Because the spatial information for the fluorescence distribution at the tissue surface was acquired in this system (i.e., as a conventional 2D planar fluorescence imaging system), the desired scan area could be precisely selected. With the camera as the detector, a smart scan method, Z-scan, was developed, which improved the imaging speed by four times over the raster scan method adopted by the previous systems. Two temporally adjacent scan positions were spatially well separated, which

significantly reduce the effect of thermal diffusion and signal crosstalk. We studied the resolution of the proposed imaging system by using a piece of porcine muscle tissue with a silicone tube, and we imaged the contrast agent distribution in the porcine tongue tissues. The USF images were validated by a commercial CT imaging system.

3.2 Materials and Methods

3.2.1 Camera-Based USF Imaging System

The schematic diagram of the proposed camera-based USF imaging system is shown in Figure 3-1. The first function generator (FG1, 33500B, Agilent, Santa Clara, CA, USA) was used to drive the excitation laser (808 nm, MGL-II-808-2W, Dragon lasers, JL, China). The excitation light passed through a band pass filter (FF01-785/62-25, Semrock Inc., Rochester, NY, USA), divided by a dual branch light guide (¼" x 72", Edmund Optics Inc., Barrington, NJ, USA) into two equal parts and illuminated the tissue sample that was placed in a water tank from two opposite directions to ensure uniform illumination. The emitted fluorescence signal was filtered by two 2-inch (BLP01-830R-50, Semrock Inc., Rochester, NY, USA) and one 1-inch emission filters (BLP01-830R-25, Semrock Inc., Rochester, NY, USA) that were placed before and after a camera lens (AF NIKKOR 50mm f/1.8D Lens, Nikon, Shinagawa, Tokyo, Japan), respectively, and received by an EMCCD camera (ProEM®-HS:1024BX3, Princeton Instruments, Trenton, NJ, USA). A HIFU transducer (2.5 MHz, H-108, Sonic Concepts Inc., Bothell, Washington, USA) driven by the second function generator (FG2, 33500B, Keysight Technologies, Santa Rosa, CA, USA) was used to switch on/off the USF contrast agent in its focus. The driving signal generated from the FG2 was amplified by a RF-AMP (A075, E&I, Rochester, NY, USA) with 50-dB gain. The amplified driving signal was then delivered to an MNW and then to a HIFU transducer to generate an ultrasonic wave. To scan the sample, the HIFU transducer was controlled by a motorized translation stage (Velmex Inc. Bloomfield, NY, USA) which received commands from the computer. The computer received the triggers via a multifunctional input/output device (I/O, PCIe-6363, National Instruments, Austin, TX, USA) from the third function generator (FG3, AFG3252, Tektronix, Beaverton, OR, USA) which was used to synchronize the camera exposure, ultrasound heating and translation stage movement. In the proposed imaging system, the XY plane represents the horizontal plane, which is perpendicular to the transmission direction of the ultrasound. The Z direction is the axial direction, which is parallel to the transmission direction of the ultrasound.

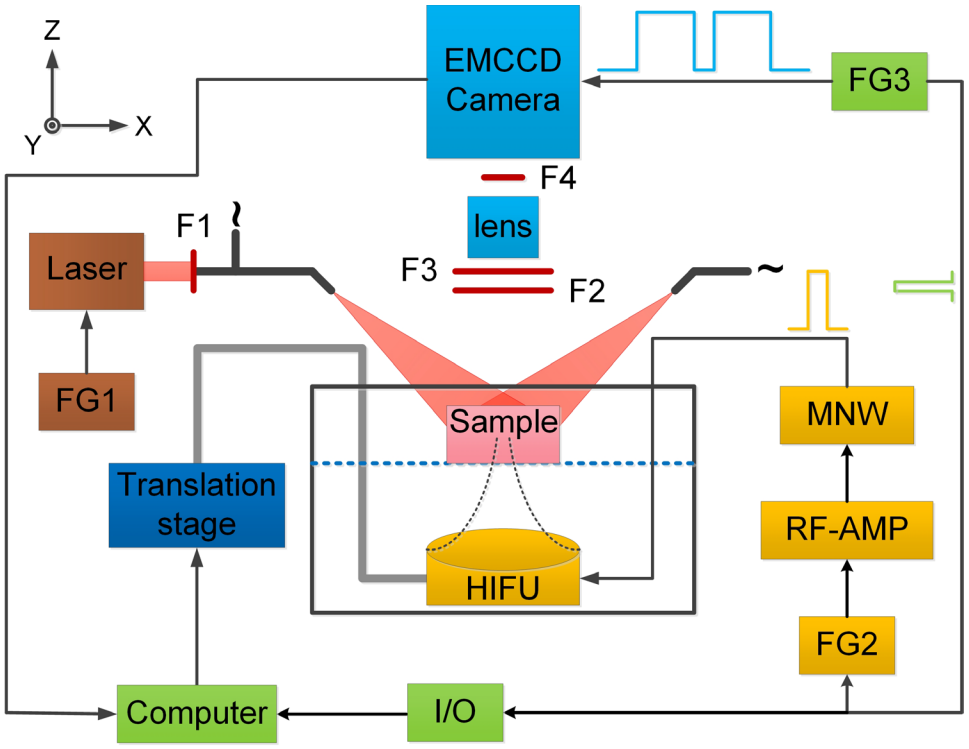

Figure 3-1 Schematic diagram of the proposed camera-based USF imaging system. FG: function generator; RF-Amp: radio-frequency power amplifier; MNW: matching network; HIFU: high intensity focused ultrasound; I/O: multifunctional input/output device; F1: excitation filter (785/62 BP); F2–F4: emission filters (830 LP).

3.2.2 Z-Scan Method

The proposed USF imaging system had two scan modes: raster scan and Z-scan. As shown in Figure 3-2(a), in the raster scan mode, the HIFU transducer was scanned from the first point to the fourth point along the x-axis positive direction, moved to the fifth point along the y-axis positive direction, and scanned the second line along the x-axis negative direction. By repeating this process, a 2D scan was achieved. This scan method was adopted in the previous FD-USF imaging system. The transducer did not move to the next adjacent position until the tissue cooled down and the USF signal vanished, which was time consuming.

To overcome this limitation, a new scan strategy named Z-scan was adopted in this camera-based USF imaging system. As shown in Figure 3-2(b1), in the Z-scan mode, the entire scan region was divided into four equal subregions, which meant the scan points in the x and y directions should be even number. The scanning sequence of the points was indicated by the numbers. As shown in Figure 3-2(b2), the HIFU transducer scanned all the first points in all subregions first. The moving trajectory of the transducer looked like a ‘Z’. As shown in Figure 3-2(b3), the

HIFU transducer moved to the fifth point in the scan sequence, which was the second point in region I, and scanned all the second points in all subregions. In Figure 3-2(b4–b5), all the points were scanned by repeating this process. The two adjacent points in the scanning sequence were separated in space, which meant the rising temperature of the tissue in the former scan position would not affect the current position significantly. By adopting this new scan method, the imaging speed of the proposed camera-based USF imaging system was four times faster than the speed achieved by the raster scan. Figure 3-2(c) shows the time sequence diagram of this USF imaging system. The EMCCD camera took two fluorescence images at each scan position and the exposure was controlled by the FG3. The first 1.5 s exposure of the camera was used to record the fluorescence image before the ultrasound heating which was a background used for the USF signal calculation. The FG3 sent triggers to the FG2 and the I/O at the same time as the first camera exposure. The FG2 delayed the trigger for 1.6 s and sent a driving signal with a duration of 0.4 s to the HIFU transducer. Directly after the ultrasound exposure, the second fluorescence image was taken with the same exposure time of 1.5 s as the previous background image. The increase in fluorescence intensity between the two frame images was caused by the HIFU-induced temperature rising and could be obtained by subtracting the first fluorescence image from the second fluorescence image. The computer received the trigger from FG3 via DAC and then sent the command to move the translation stage after 3 s. Because the HIFU transducer was below the sample, the movement of the transducer did not affect the collection of emitted fluorescence. The time intervals between the two adjacent scanning locations in the sequence were 20 s in raster scan mode and 5 s in Z-scan mode. The 20 s interval in the former was mainly to wait for tissue to cool down; therefore, avoiding fluorescence cross talk between the adjacent locations.

The focus of the HIFU transducer was initially positioned on the bottom surface of a small tank used to hold the sample. The position of the focus was also identified and calibrated in the field of view of the camera by positioning the ultrasound focus on a silicone tube inserted at the surface of a transparent silicone phantom and by calculating the geometric center of the obtained USF signal pattern.

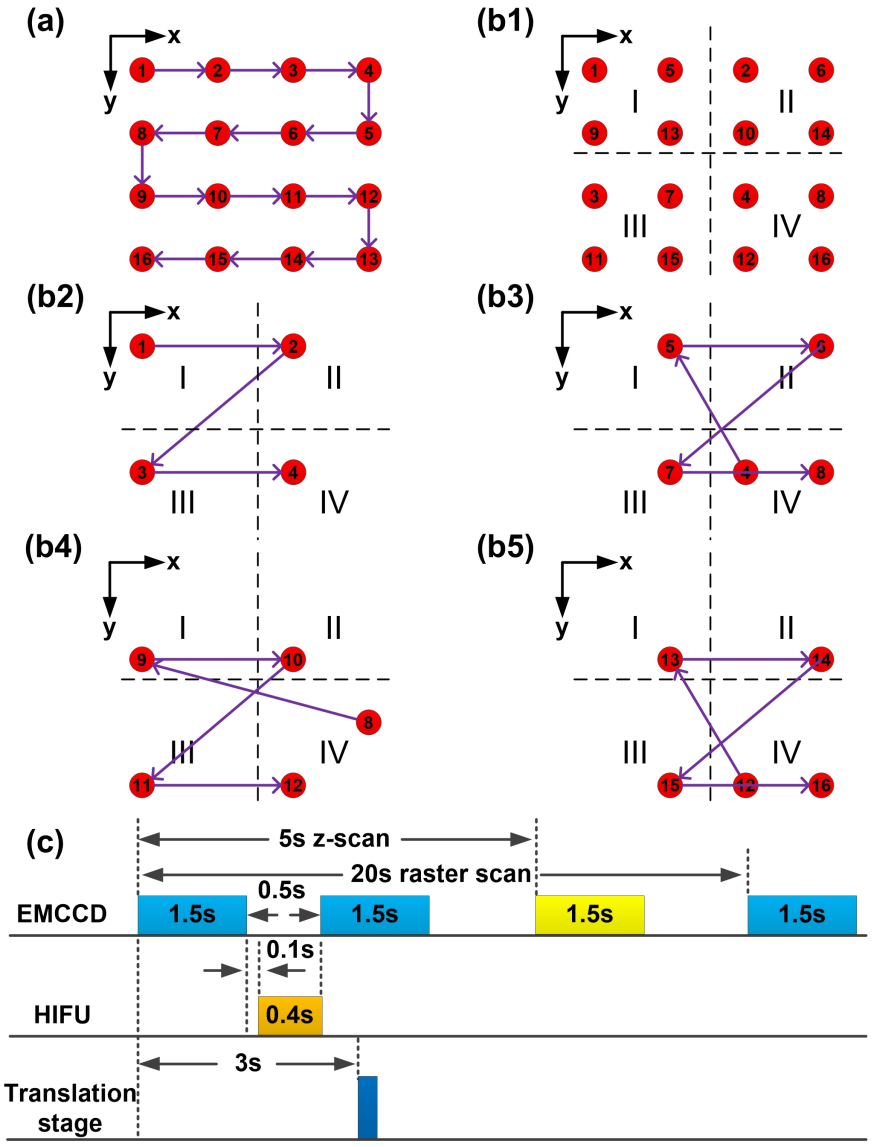

Figure 3-2 Schematic diagram of (a) raster scan and (b1–b5) Z-scan; (c) time sequence diagram of the USF imaging system.

3.2.3 Resolution Measurement of the USF Imaging System

A silicone tube (ST 60-011-01, Helix Medical, Carpinteria, CA, USA) with an inner diameter of 0.31 mm and an outer diameter of 0.64 mm was inserted into a porcine muscle tissue with a thickness of ~10 mm at a depth of ~5 mm. The tissue was placed on a piece of transparent parafilm (PM-992, BEMIS Company Inc. Neenah, WI, USA) that sealed the rectangle window of a small plastic tank. The gap between the parafilm and the bottom side of the tissue was filled with ultrasound gel (01–08, Aquasonic 100, Parker Laboratories Inc., Fairfield, NJ, USA) to maintain the appropriate ultrasound coupling. To prevent the tissue from drying during the experiment, the surface of the tissue

was covered by ultrasound gel and a piece of transparent parafilm. Before USF imaging, the ultrasound focus was positioned on the silicon tube which was then filled with ICG-PINIPAM NP with an LCST of ~24–25 °C. The intensity of the excitation light illuminated on the tissue was 6.16 mW/cm^2 (Power: 4.367 mW, sensor's area: 0.709 cm^2), which was measured by a power and energy meter (PM100D, Thorlabs Inc. Newton, NJ, USA). To obtain the lateral and axial 1D profiles of the silicone tube in the USF imaging, the HIFU transducer scanned the tube in the Y direction (with a step size of 127 μm and a scanning range of 7.112 mm) and in the Z direction (with a step size of 508 μm and a range of 10.16 mm), respectively.

3.2.4 USF Image Processing and Co-Registration

As mentioned above, the increase in fluorescence can be extracted by subtracting the first fluorescence image (i.e., the background fluorescence image) from the second fluorescence image (i.e., the fluorescence image acquired after HIFU exposure). To convert this subtracted image into a single value of the signal strength to represent the HIFU-induced fluorescence increase at each scan location, a 7 × 7 pixel moving average filter was applied to the subtracted image. A threshold of 100 counts was set to remove obvious noise. Then, a square with a side length of 1 mm was drawn at the center of the scan position on the processed image. Finally, the photon counts of all the pixels within this square were averaged and used to represent the strength of the HIFU-induced fluorescence increase at the current location. Accordingly, a single number could be calculated for each scanning point, and a 3D USF image could be formed by scanning a 3D volume. Note that the specific threshold and side length might be varied in different samples for better USF image quality.

The 2D USF images of the contrast agent distribution on the XY plane at different depths were obtained by performing 2D USF imaging along the Z direction. Because of the excitation light and the emitted fluorescence attenuated with the depth of the tissue, the intensity of the USF signals from different layers were not comparable. Thus, the signal intensity was normalized at each layer. The pixel size of these USF images was interpolated to 50.8 μm, and the target (i.e., contrast agent distribution at that depth) was differentiated from the background via the 2D Otsu method [46]. By combining all the 2D USF images, a 3D USF image was obtained. The 2D X-ray projections were reconstructed into a 3D CT image using the software provided by the manufacturer of the micro-CT system (NRecon). Because the exact scan area of the USF imaging was known, the 3D CT image of the contrast agent distribution could be extracted from the reconstructed CT image using the software provided by the manufacturer (CTAn). The 3D USF image and the 3D CT image were co-registered in the software provided by the manufacturer

(DataViewer). The co-registration was realized by slightly moving and rotating the USF image compared to the CT image, which may not be accurate because no markers could be detected by the two modalities. The visualization of the 3D images was realized using ParaView (Sandia National Laboratory, Kitware Inc, Los Alamos National Laboratory).

3.3 Results and Discussion

3.3.1 Resolution Measurement of the USF Imaging System

To measure the resolution of the proposed camera-based USF imaging system and the effect of the driving voltage on the resolution, we carried out USF imaging on a piece of porcine muscle tissue in which a silicone tube was inserted to mimic a blood vessel. Figure 3-3(a) shows a white-light photo of the silicone tube embedded tissue. As shown in Figure 3-3(b), the size of the tube shown by fluorescence imaging on the tissue surface is quite large because of the high scattering property of the tissue (a threshold of 0.3 is applied). Figure 3-3(c) shows the lateral (i.e., Y direction) 1D USF profiles of the silicone tube with two various HIFU driving voltages of 60 mV and 80 mV (i.e., the Vpp from FG2, estimated ultrasound power: 0.43 W and 0.77 W). The peak values of the USF profiles for the two driving voltages of 60 and 80 mV are 138 and 319 counts, respectively. As shown in Figure 3-3(d), the FWHM of the lateral profiles for the two driving voltages are 0.85 and 1.11 mm, respectively. As shown in Figure 3-3(e), the peak values of the USF profiles for the two driving voltages of 60 and 80 mV are 136 and 359 counts, respectively. As shown in Figure 3-3(f), the FWHM of the axial profiles for the two driving voltages are 2.46 and 4.19 mm, respectively. The USF signal strength is higher under the larger driving voltage (i.e., higher ultrasound power), which means a better SNR. However, the increase of FWHM means a worse resolution. This is because the higher temperature rise leads to the larger size of the thermal focal zone and results in more USF contrast agents are switched on. It should be noted that the axial FWHM is about 3~4 times larger than the lateral FWHM which is due to the nonuniform shape of the HIFU transducer focus. The lateral and axial FWHMs of the acoustic intensity focus were measured as 0.55 mm and 2.8 mm [33], respectively. As shown in Figure 3-3(g), the FWHM of the 1D profile obtained by fluorescence imaging (same position on the x-axis as USF imaging) is 9.59 mm. Compared to the fluorescence imaging, the USF imaging improved the resolution by ~11 times (using a 60-mV driving voltage).

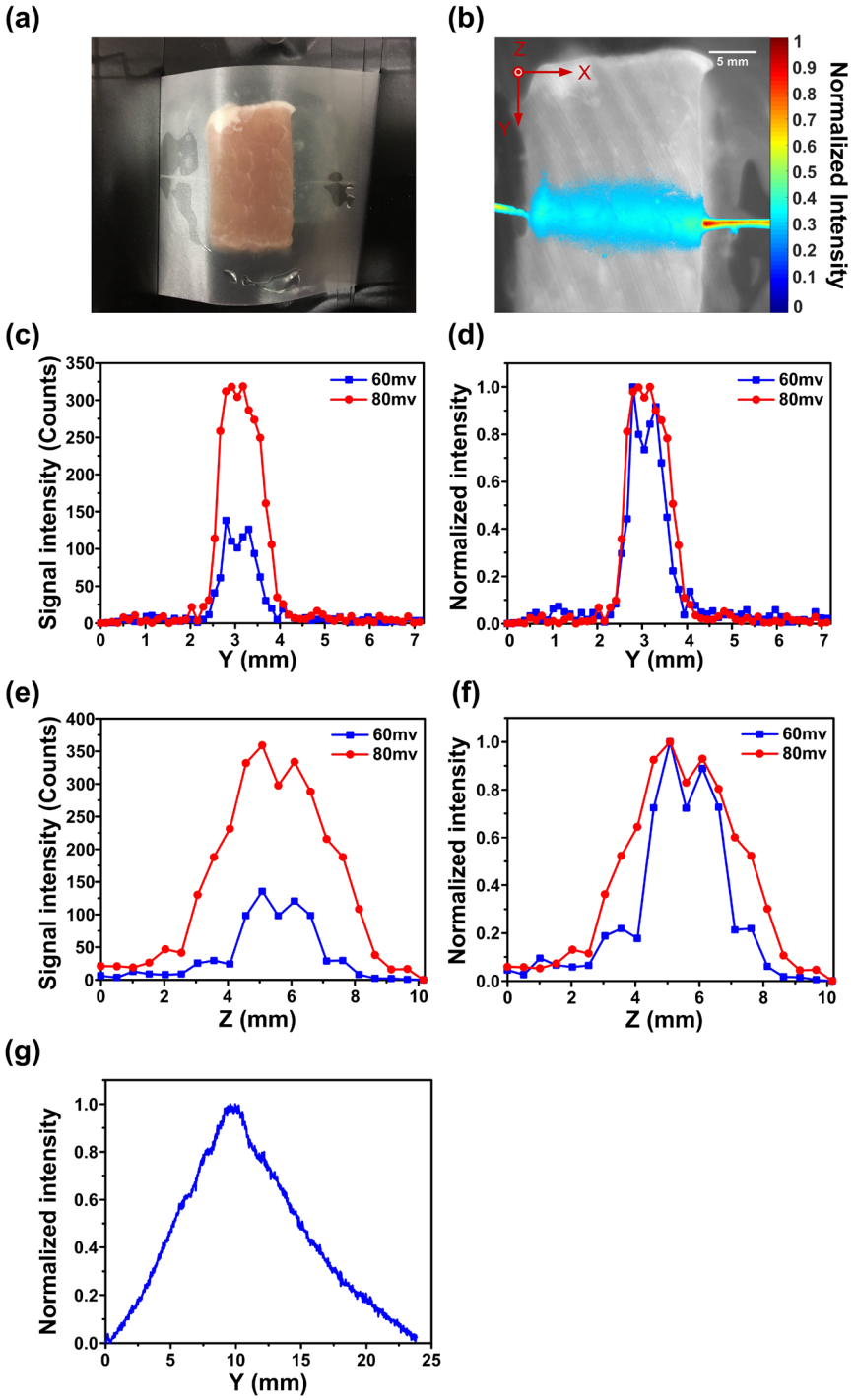

Figure 3-3 (a) A white-light photo of the porcine muscle tissue inserted with a silicone tube. (b) The fluorescence image of the silicone tube filled with ICG-PINIPAM NP inside the tissue (threshold = 0.3). (c) and (d) are the original and normalized lateral (i.e., Y direction) 1D profiles of the silicone tube with a driving voltage of 60 mV (the blue solid line with squares) and a driving voltage of 80 mV (the red solid line with circles), respectively. (e) and (f) are

the original and normalized axial (i.e., Z direction) 1D profiles of the silicone tube with a driving voltage of 60 mV (the blue solid line with squares) and a driving voltage of 80 mV (the red solid line with circles), respectively. (g) Normalized 1D profile of the silicone tube via fluorescence imaging.

3.3.2 Comparison of the Raster Scan and Z-Scan

Figure 3-4(a) shows a white-light photo of the porcine tongue tissue. Because the porcine tongue tissue was relatively dense compared to other available porcine muscle tissues, the contrast agents were less diffused after a local injection. The USF contrast agent (30 μL ICG-PINIPAM NP) with an LCST of ~24–25 °C mixed with the commercial CT contrast agent (10 μL ExiTronTM nano 12000, Miltenyi Biotec, Bergisch Gladbach, Germany) was locally injected into the tissue with a thickness of 1.3 cm to form a single spot. Figure 3-4(b) shows the 2D and normalized fluorescence intensity distribution on the top surface of the tissue. The red box indicates the horizontal scan plane (XY) of the USF imaging. To avoid optical cross talk, the separation distance between the two adjacent scan points in Z-scan mode, such as the distance between point number 1 and number 2, should be examined. To achieve this goal, the USF signal pattern's change in space and time at a scan point was investigated. Specifically, an ultrasound pulse with a 60-mV driving voltage and 400 ms duration was applied to the position indicated by the white spot in Figure 3-4(b). The depth of this scan position was 7.62 mm from the bottom of the tissue. It took 615.82 ms (500 ms exposure time and 115.82 ms readout time) to record a single fluorescence image. A total of 60 frames was recorded (3 frames before the ultrasound exposure and 57 frames after the ultrasound exposure). The background image was obtained by averaging the three frames before the ultrasound exposure. Thus, the dynamic pattern of the USF signal was obtained from the fourth frame to the last one. To analyze the data, the spatial distribution of USF photons on the fifth frame (after it was subtracted by the background image) is shown in Figure 3-4(c). A white bar is drawn on the image. One end is located at the center of the pattern and indicates the location of the HIFU focus (i.e., heating position). The other end of the bar is far away from the center and well beyond the HIFU heating zone. By extracting the data along this white bar at all the different time points, Figure 3-4(d) shows a 2D representation of the HIFU-induced USF photons in space and time. The origin of this image indicates the position where this was illuminated by the ultrasound. The USF photons near the heating center decays slowly, which is why the time interval between the two adjacent scan positions in raster scan mode is long and the imaging speed is low. On the other hand, the USF photons are very weak at the location that is 5 mm away from the heating center after 3 s. Thus, if the next scan location is positioned at 5 mm away from the previous scan location and the next background is taken 3 s after the previous HIFU exposure, the

interference (i.e., cross talk) of the USF photons between these two temporally adjacent scan locations can be avoided. Obviously, it is also true that if the separation distance between two scan points can be increased to 6 mm or above, the waiting time can be avoided. Thanks to the size of the USF signal pattern was limited in space and shrank with time, the Z-scan can significantly improve the imaging speed without suffering the effect of thermal diffusion. Figure 3-4(e) and 3-4(f) show the 2D USF images on the XY plane at Z=7.62 mm using the raster scan and Z-scan, respectively. The patterns of these two images were similar, but the imaging speed of the Z-scan was four times faster than that of the raster scan.

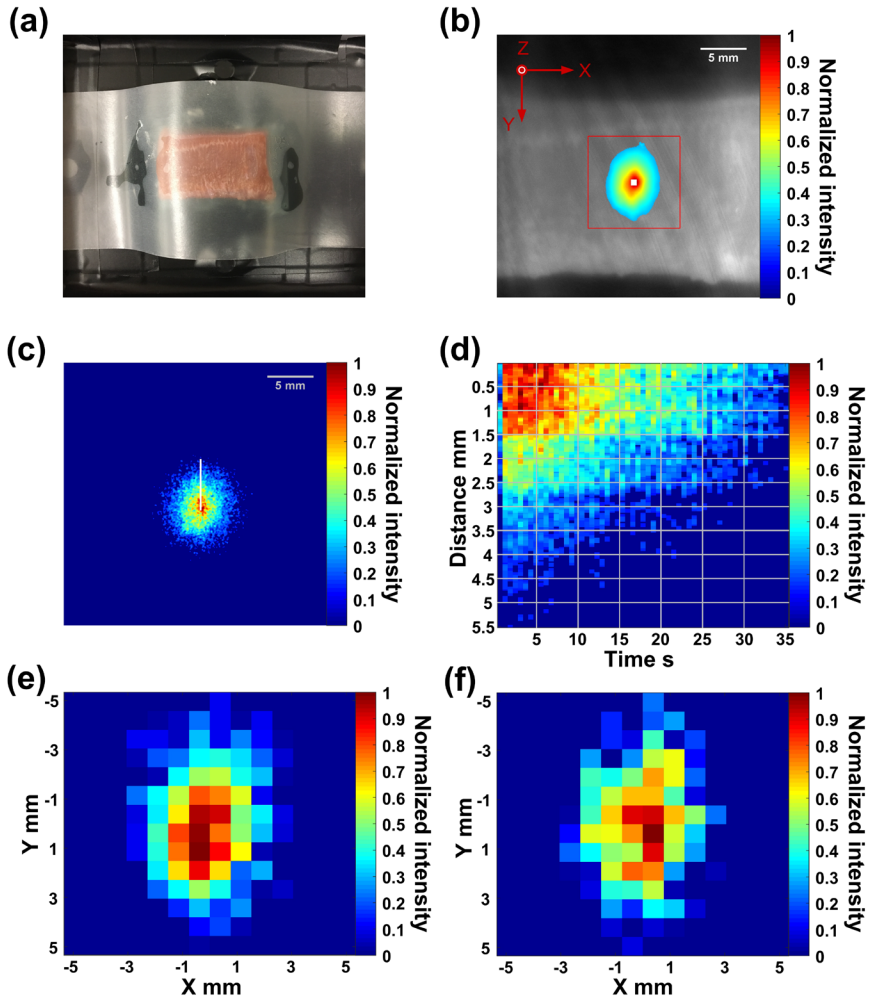

Figure 3-4 (a) A white-light photo of the porcine tongue tissue. (b) The fluorescence image of the mixed contrast agents distribution in the tissue and the red square indicates the scan area of the USF imaging on the horizontal (XY) plane. The white spot indicates the position measuring the USF signal. (c) The pattern of USF signal and the white bar indicates the positions for studying USF signal intensity change with time. (d) The USF signal intensity's change

in space and time. (e) The USF image on the XY plane using the raster scan. (f) The USF image on the XY plane using the Z-scan.

3.3.3 The USF Imaging of the Contrast Agent Distribution in Tissue

To obtain the 3D contrast agent distribution in the porcine tongue tissue shown in Figure 3-4(a), a volume of 9.906 × 9.906 × 10.16 mm^3 was scanned by the HIFU transducer with a driving voltage of 60 mV using the Z-scan method. The lateral step size was 0.762 mm, and the axial step size was 2.032 mm. After the USF imaging, the tissue was scanned by a commercial micro-CT system (Skyscan 1178, Bruker, Kontich, Belgium). Figure 3-5 shows the 2D USF images of the contrast agent distribution on the XY plane at different depths (i.e., Z direction).

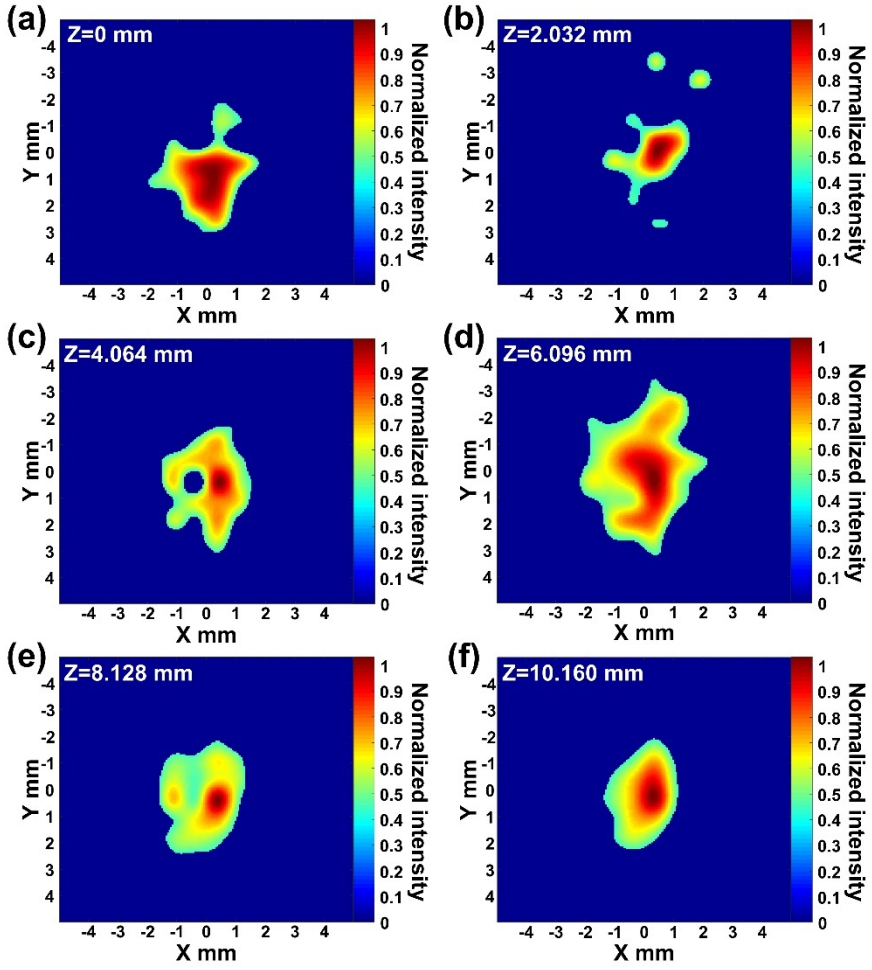

Figure 3-5 2D USF images on XY plane at different depths.

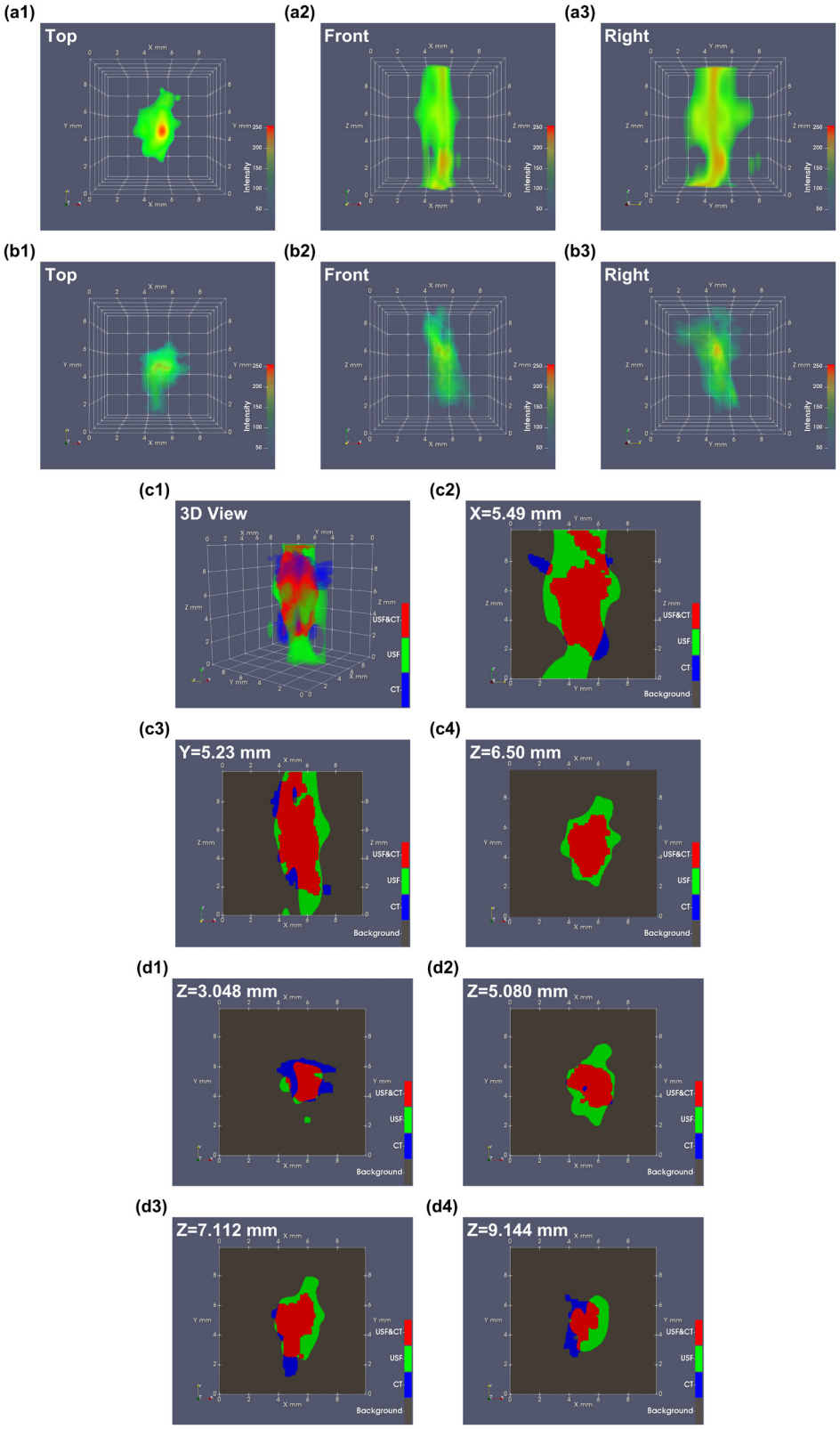

Figure 3-6 (a1–a3) The top view (XY), front view (XZ) and right view (YZ) of the 3D USF images. (b1–b3) The top view (XY), front view (XZ) and right view (YZ) of the reconstructed 3D CT images. (c1) The 3D view of the co-

registered image of the two modalities and (c2–c4) the corresponding 2D cross-section images at X=5.49 mm, Y=5.23 mm and Z=6.50 mm, respectively. (d1–d4) 2D cross-section images of the 3D co-registered image at different depths.

Figure 3-6(a1–a3) show the top view (XY), front view (XZ), and right view (YZ) of the 3D USF images of the USF contrast agent distribution, respectively. Figure 3-6(b1–b3) show the top view (XY), front view (XZ), and right view (YZ) of the 3D CT images of the CT contrast agent distribution, respectively. Figure 3-6(c1) shows the 3D co-registered USF and CT images and Figure 3-6(c2–c4) are the corresponding cross-section images on different planes. The blue volumes or areas indicate the distribution of the CT contrast agent while the green ones show the distribution of the USF contrast agent. The red ones indicate the contrast agent distributions detected by both imaging modalities. In the 3D view image (i.e., Figure 3-6(c1)), the common volume accounts for 48.04% of the total volume of the USF image and 72.49% of the total volume of the CT image, respectively. On the YZ plane at X=5.49 mm (i.e., Figure 3-6(c2)), the common area accounts for 54.32% of the USF image area and 88.65% of the CT image area. On the XZ plane at Y=5.23 mm (i.e., Figure 3-6(c3)), the common area accounts for 68.30% of the USF image area and 88.58% of the CT image area. On the XY plane at Z=6.50 mm (i.e., Figure 3-6(c4)), the common area accounts for 58.26% of the USF image area and 100% of the CT image area. The comparisons at different cross-sections are summarized in Table 3-1. Figure 3-6(d1–d4) show the 2D cross-section images of the 3D co-registered image at different depths (along the Z direction).

Table 3-1 The comparison of USF image and CT image with a single target.

Plane	The proportion of overlap part in USF image	The proportion of overlap part in CT image
Total volume	48.04%	72.49%
YZ plane at X=5.49 mm	54.32%	88.65%
XZ plane at Y=5.23 mm	68.30%	88.58%
XY plane at Z=6.50 mm	58.26%	100%

To investigate the capability of the USF imaging with a more complicated contrast agent distribution pattern, as shown in Figure 3-7(a), 45 μL USF contrast agent mixed with 15 μL CT contrast agent was locally injected into a porcine tongue tissue with a thickness of 1.3 cm in three different locations to form three spots (20 μL each). Figure 3-7(b) shows the 2D and normalized fluorescence intensity distribution on the top surface of the tissue. The red box indicates the scan area of the USF imaging on the horizontal plane. A volume of 12.954 × 12.954 × 10.16 mm^3 was

scanned by the HIFU transducer with a driving voltage of 60 mV using the Z-scan method. The lateral step size was 0.762 mm, and axial step size was 2.032 mm. Figure 3-7 (c–h) show the 2D USF images of the contrast agent distribution on the XY plane at different depths. The three spots can be seen clearly in these USF images at some depths while are not observable in the regular fluorescence image (i.e., Figure 3-7(b)) that is the only image acquired on the tissue surface.

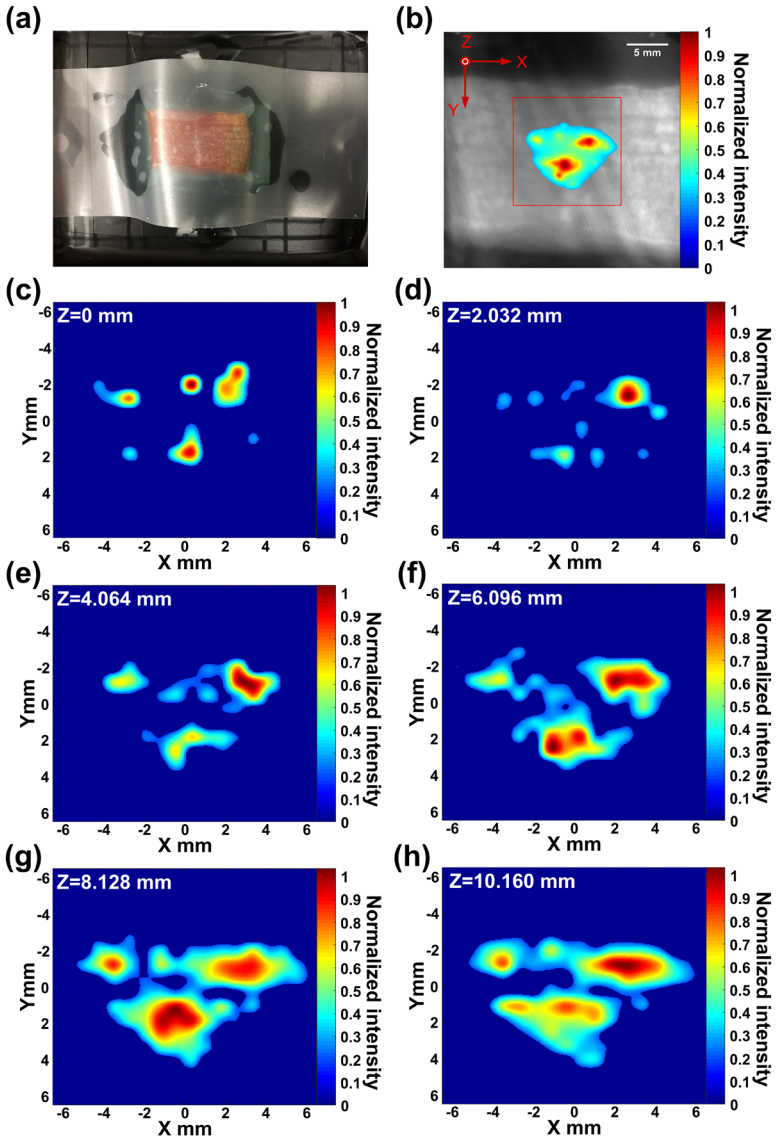

Figure 3-7 (a) A white-light photo of the porcine tongue tissue. (b) The fluorescence image of the mixed contrast agents distribution in the tissue and the red square indicates the scan area of the USF imaging on the horizontal (XY) plane. (c) to (h) are the 2D USF images on XY plane at different depths.

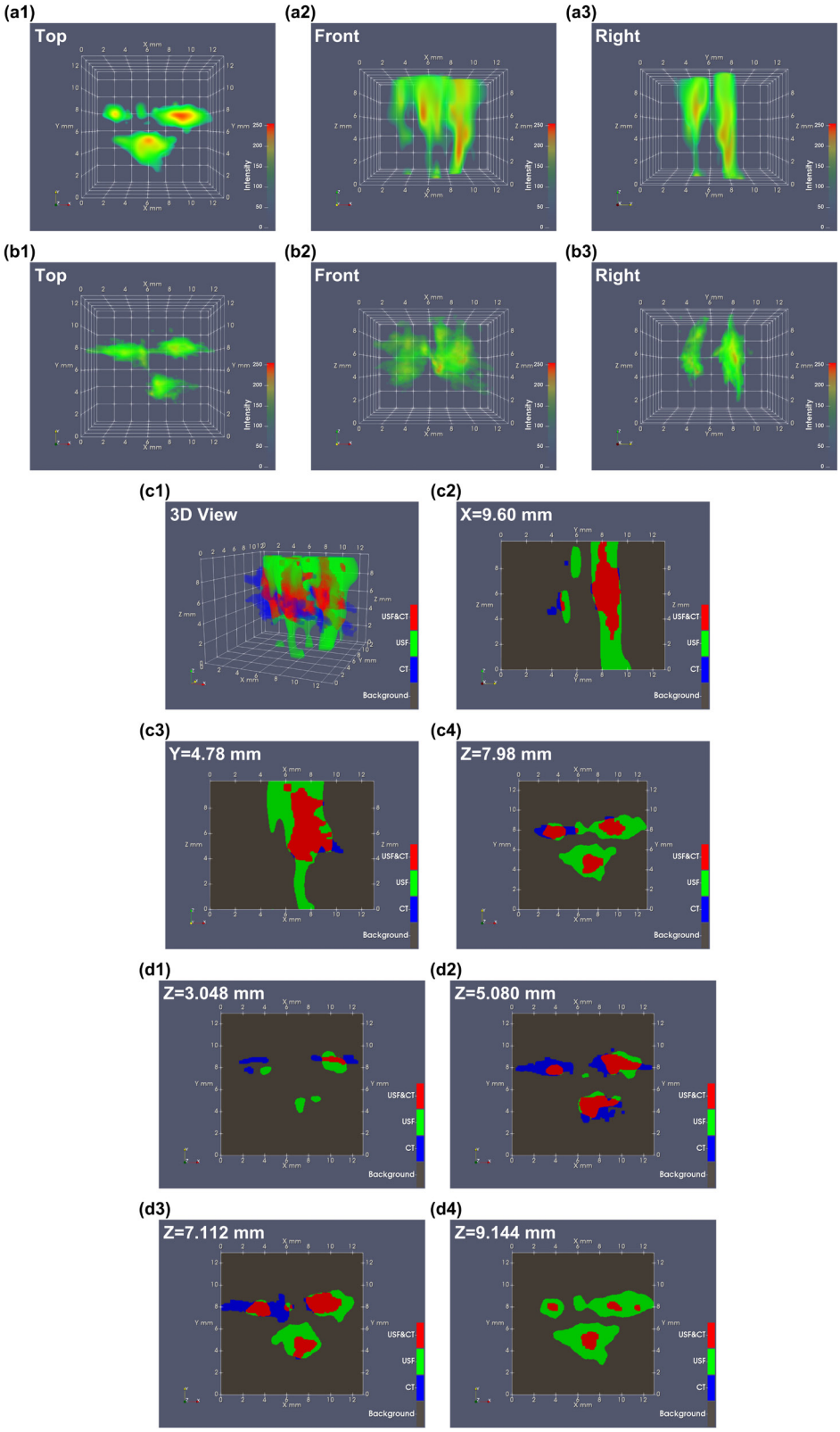

Figure 3-8 (a1–a3) The top view (XY), front view (XZ) and right view (YZ) of the 3D USF images. (b1–b3) The top view (XY), front view (XZ) and right view (YZ) of the reconstructed 3D CT images. (c1) The 3D view of the co-

registered images of the two modalities and (c2–c4) the corresponding 2D cross-section images at X=9.60 mm, Y=4.78 mm and Z=7.98 mm, respectively. (d1–d4) 2D cross-section images of the 3D co-registered image at different depths.

Figure 3-8(a1–a3) show the top view (XY), front view (XZ), and right view (YZ) of the 3D USF images of the USF contrast agent distribution, respectively. Figure 3-8(b1–b3) show the top view (XY), front view (XZ), and right view (YZ) of the 3D CT images of the CT contrast agent distribution, respectively. Figure 3-8(c1) shows the 3D co-registered USF and CT images and Figure 3-8(c2–c4) are the corresponding cross-section images on different planes. In the 3D view image (i.e., Figure 3-8(c1)), the common volume accounts for 32.16% of the total volume of the USF image and 54.40% of the total volume of the CT image, respectively. On the YZ plane at X=9.60 mm (i.e., Figure 3-8(c2)), the common area accounts for 42.93% of the USF image area and 90.40% of the CT image area. On the XZ plane at Y=4.78 mm (i.e., Figure 3-8(c3)), the common area accounts for 45.91% of the USF image area and 94.14% of the CT image area. On the XY plane at Z=7.98 mm (i.e., Figure 3-8(c4)), the common area accounts for 32.58% of the USF image area and 80.86% of the CT image area. The comparisons at different cross-sections are summarized in Table 3-2. Figure 3-8(d1–d4) show the 2D cross-section images of the 3D co-registered image at different depths (along the Z direction).

Table 3-2 The comparison of USF image and CT image with multiple targets.

Plane	The proportion of overlap part in USF image	The proportion of overlap part in CT image
Total volume	32.16%	54.40%
YZ plane at X=9.60 mm	42.93%	90.40%
XZ plane at Y=4.78 mm	45.91%	94.14%
XY plane at Z=7.98 mm	32.58%	80.86%

3.4 Conclusion

In this study, we developed a camera-based USF imaging system to overcome the limitations faced by the previous USF systems that adopted a fiber bundle to collect the photons. By using the Z-scan method, the imaging speed was significantly improved compared to the former raster scan method. The USF imaging of the contrast agent distribution inside the porcine tongue tissue was investigated. All the results of the USF imaging were validated by the micro-CT imaging. In this study, the scan region was only divided into four subregions and was limited by the

speed of translation. This limitation can be solved in the future by optimizing the exposure time and improving the speed of scanning the HIFU focus. Therefore, the imaging speed can be further improved. The work in this chapter has been published in IEEE Journal of Selected Topics in Quantum Electronics [57].

Chapter 4

IN VIVO USF IMAGING USING PNIPAM/B-CD/ICG NANOGEL AND CAMERA-BASED USF IMAGING SYSTEM

4.1 Introduction

In the NIR spectral range, the penetration depth of light becomes larger due to the smaller optical absorption and scattering coefficients of biological tissue. Thus, the fluorescence imaging in NIR region has attracted tremendous attention [58]. In particular, NIR fluorescence imaging between 700 and 900 nm has enabled new technologies for a variety of preclinical and clinical applications [59]. Compared with conventional diagnostic imaging, such as CT, MRI, or PET, NIR fluorescence imaging provides a cost-efficient and high-sensitivity method for real-time molecular imaging [60]. Currently, a serious problem obstructing the applications of the NIR fluorescence technique is the poor resolution in deep tissue [9, 61]. The spatial resolution dramatically declines with the increase of tissue thickness. To address this challenge, USF imaging as a new hybrid imaging modality was developed by our group in the past years [24, 32, 51, 53, 57]. USF imaging employs a unique imaging probe that can be sensitively switched on via ultrasound-induced temperature increase only in the ultrasound focal volume. This indicates that the trapped USF signal only comes from the signal changes of the contrast agent itself, and its signal dynamic pattern can be expediently manipulated by externally controlling the ultrasound exposure, implying that the USF method has high specificity with regard to the contrast agent. These advantages greatly encourage us to explore the USF imaging *in vivo*.

ICG-PNIPAM NP, a type of temperature-responsive USF probe, is one of the most successful NIR-USF contrast agents, which is sensitive to the ultrasound-induced temperature change in focal volume [31]. As shown in chapter 2, *in vivo* USF imaging was successfully achieved using ICG-PNIPAM NP. However, one of the drawbacks of this type of the probe is that its emission peak is blue shifted compared to that of free ICG in water. To remain ICG's NIR emission peak, minimize tissue autofluorescence, achieve better SNR and increase *in vivo* circulation time of this type of contrast agent, there is an urgent need to upgrade the previous ICG-PNIPAM probe to accelerate the utilization of USF imaging in biomedical applications.

Recently, we developed a new ICG-based USF contrast agent, ICG/β-CD complex-encapsulated PNIPAM nanogel (PNIPAM/β-CD/ICG nanogel), to overcome the limitations of the ICG-PNIPAM NP [38]. The average diameter of the PNIPAM/β-CD/ICG nanogel was significantly decreased to ~32 nm from ~335 nm compared to the reported ICG-PNIPAM NP. Additionally, the excitation/emission characteristics of the ICG itself in PNIPAM/β-CD/ICG nanogel were almost completely retained. In this study, the USF performance of the PNIPAM/β-CD/ICG

nanogel was compared with that of the ICG-PNIPAM NP in centimeters-deep chicken breast tissue. The feasibility of *in vivo* USF imaging using PNIPAM/β-CD/ICG nanogel and the camera-based USF imaging system (developed in the previous chapter) was also studied.

4.2 Materials and Methods

4.2.1 Camera-Based USF Imaging System

The details of the camera-based USF imaging system are descried in the Chapter 3. Briefly, we applied a HIFU transducer with a center frequency of 2.5 MHz to heat the sample and switch on the temperature-sensitive probe in the focus. In this study, the ultrasound exposure time was kept at 400 ms and the driving voltage was changed with the different samples. The emitted USF signal was collected through a camera-based fluorescence imaging system. The wavelength of the excitation light was set as 808 nm and the emitted fluorescence signal was filtered by a set of 830 long-pass filters. The background temperature of the sample was controlled by a water bath via an integrated programmed temperature controller system and a magnetic stirrer inside the water bath.

4.2.2 NIR-USF Imaging in the Silicone Tube Embedded Chicken Breast Tissue

A silicone tube with an inner diameter of 0.76 mm and an outer diameter of 1.65 mm was inserted into a piece of chicken breast tissue with a thickness of ~1.5 cm or ~3.5 cm at a height of ~5 mm from the bottom surface to simulate a blood vessel. The tissue sample was placed in a small plastic cell and covered it with a transparent parafilm (PM-992, BEMIS Company Inc., USA). The space between the bottom surface of the tissue and the parafilm was filled with ultrasound transmission gel (Aquasonic 100, Parker Laboratories Inc., USA) to provide efficient ultrasound coupling. The top surface of the tissue sample was also covered by the ultrasound gel and the parafilm to prevent the tissue from drying during the experiment. The ICG-PNIPAM NP and PNIPAM/β-CD/ICG nanogel were injected into the silicone tube via a microsyringe, respectively. The bottom of the small tank was further immersed into a 37 °C water bath to ensure the temperature of the tissue sample close to normal body temperature. An area of 10.16 (X) × 2.54 (Y) mm^2 (step size in X direction: 0.2032 mm; Y direction: 1.27 mm) was scanned by the HIFU transducer with an estimated ultrasound power of 2.36 W. The intensity of the excitation light at 808 nm was measured as 29.25 mW/cm^2 by using a power and energy meter (PM100D, Thorlabs Inc., USA).

4.2.3 Metabolism and In vivo Biodistribution of the PNIPAM/β-CD/ICG Nanogel in BALB/c Mice

Three healthy BALB/c mice (female, 8-10 weeks) were purchased from Jackson Laboratory (Maine, USA) in this study. To explore the metabolism of the PNIPAM/β-CD/ICG nanogel, the mouse (20.6 g) was firstly anesthetized with 2.5% isoflurane at a flow rate of 1 L/min, and the hair on the whole body surface was removed using depilatory cream. Next, 200 μL of PBS dispersion of PNIPAM/β-CD/ICG (~8.0 mg/mL) was administrated via a tail vein injection, where the maximum intravenous dose was 77.6 mg/kg. The 2D fluorescence images of the whole mouse body were collected before the tail vein injection and at different time points (0, 1, 2, 4, 6, 24 , 48, 120 h) after the tail vein injection via a home-made NIR fluorescence imaging system (λ_{ex} = 808 nm, λ_{em} = 830 nm). To evaluate the *in vivo* biodistribution of PNIPAM/β-CD/ICG nanogel, 200 μL of PBS dispersion of PNIPAM/β-CD/ICG (~8.0 mg/mL) was intravenously injected into the mice. The mouse (with a weight of 20.7 g and a corresponding dose of 77.6 mg/kg) and the another one (with a weight of 21.6 g and a corresponding dose of 74.08 mg/kg) were sacrificed at 15 and 90 min after the injection, respectively. Their major organs (heart, kidney, liver, lung, spleen, stomach, large intestine and small intestine) were then harvested and imaged using the same imaging system.

4.2.4 Ex vivo NIR-USF Imaging of Mouse Liver via a Tail Vein Injection

The healthy BALB/c mouse (female, 14 weeks, 27.3 g) was firstly anesthetized with 2.5% isoflurane, and then 200 μL of a PBS dispersion of PNIPAM/β-CD/ICG (~8.0 mg/mL) was injected into the mouse body via a tail vein (the corresponding dose is 58.64 mg/kg). The mouse was sacrificed at 5 min after the injection and the liver was harvested. Part of the liver was then inserted into a piece of porcine heart tissue with a thickness of 1 cm for *ex vivo* USF imaging. The intensity of the as-used excitation light at 808 nm was 26.12 mW/cm^2. A volume of 15.240 (X) × 15.240 (Y) × 6.096 (Z) mm^3 (step size in X&Y direction: 1.016 mm; Z direction: 2.032 mm) was scanned by a HIFU transducer with an estimated ultrasonic power of 4.82 W.

4.2.5 In vivo Biodistribution of the PNIPAM/β-CD/ICG Nanogel in U87 Brain Tumor-Bearing Mice

The healthy NU/J nude mice (female, 6 weeks) were purchased from Jackson Laboratory to establish subcutaneous brain tumor models. Suspension of U87 brain cancer cells (ATTC, USA) was subcutaneously injected into the right hind legs of mice to build the subcutaneous tumor models. The mice were then housed there under pathogen-free conditions. A nude mouse (female, 11 weeks, 22.63 g) was used for this experiment. 200 μL of PBS dispersion of PNIPAM/β-CD/ICG (~8.0 mg/mL) was administrated by tail vein injection (corresponding dose: 70.7 mg/kg). The 2D fluorescence images of the whole mouse body were collected before the intravenous injection and at

different time points (0, 1, 2, 4, 6, 8, 10, 24 h) after the intravenous injection via a home-made NIR fluorescence imaging system.

4.2.6 In vivo NIR-USF Imaging in U87 Brain Tumor Bearing Mice

The U87 tumor bearing nude mouse (13 weeks, 22.58 g) with a tumor size of ~2 cm was used for this experiment. The 35 μL and 20 μL PBS dispersions of PNIPAM/β-CD/ICG were injected into the tumor at two different positions, respectively. During the experiment, the mouse was anesthetized with 2.0 % isoflurane at a flow rate of 0.8 L/min. The temperature of the water bath was kept at 38 °C to sustain the mouse body temperature. The intensity of the excitation light at 808 nm was 0.37 mW/cm^2. A volume of 12.954 (X) × 12.954 (Y) × 8.128 (Z) mm^3 (step size in X&Y direction: 0.762 mm; Z direction: 2.032 mm) was scanned by the HIFU transducer with an estimated ultrasonic power of 3.90 W.

4.2.7. Calculation of SNR

The 2D USF image of the silicone tube was normalized line-by-line (i.e., along the x direction). Each line of the USF image corresponds to a SNR value, and the SNR of the integral USF image was defined as the mean SNR value of all the lines. The SNR was calculated by the following equation:

$$SNR = 20\log_{10}\frac{signal}{noise}$$

where the signal was defined as the root-mean-square of all the values larger than 0.5 in each line, and the noise was defined as the standard deviation of the 10 scan points at the edge of the line (5 points each side).

4.3 Results and Discussion

4.3.1 Comparison of the Two Types of ICG-Based PNIPAM Probes for NIR-USF Imaging

The detectable photons in the USF imaging decrease rapidly with the increase of the tissue thickness, which results in a fast deterioration of SNR [25]. Therefore, high performance USF contrast agents are highly desirable for deep tissue imaging. The USF performance of PNIPAM/β-CD/ICG nanogel and ICG-PNIPAM NP were compared in chicken breast tissues with different thicknesses. The 2D USF images of a silicone tube filled with PNIPAM/β-CD/ICG nanogel (or ICG-PNIPAM NP) in 1.5-cm (or 3.5-cm) thick chicken breast tissue are shown in Figure 4-1. SNR is used to evaluate the USF performance, so we further calculated and analyzed the SNR of the USF image. As shown in Figure 4-1(b) and 4-1(c), results reveals that the SNR of the USF image for PNIPAM/β-CD/ICG nanogel (33.01 ± 2.42 dB) is obviously higher than that of the ICG-PNIPAM NP (18.73 ± 0.33 dB) in 1.5 cm-thick chicken

breast tissue. For further testing, both contrast agents were reevaluated using the same protocol in a 3.5 cm-thick chicken breast tissue. As shown in Figure 4-1(d) and 4-1(e), the SNR of the USF image for PNIPAM/β-CD/ICG nanogel is calculated as 19.57 ± 1.68 dB. Nevertheless, the same silicone tube cannot be differentiated from the background when using ICG-PNIPAM NP. This is understandable based on the following discussion. Compared with ICG-PNIPAM NP, the characteristic of the fluorescence emission of the PNIPAM/β-CD/ICG nanogel is more like that of the ICG [38]. This indicates that the fluorescence emission in the NIR region is enhanced when using the PNIPAM/β-CD/ICG nanogel, which leads to the enhancement of the USF signal and thereby the improvement of the SNR under the similar on-to-off ratio and other test conditions.

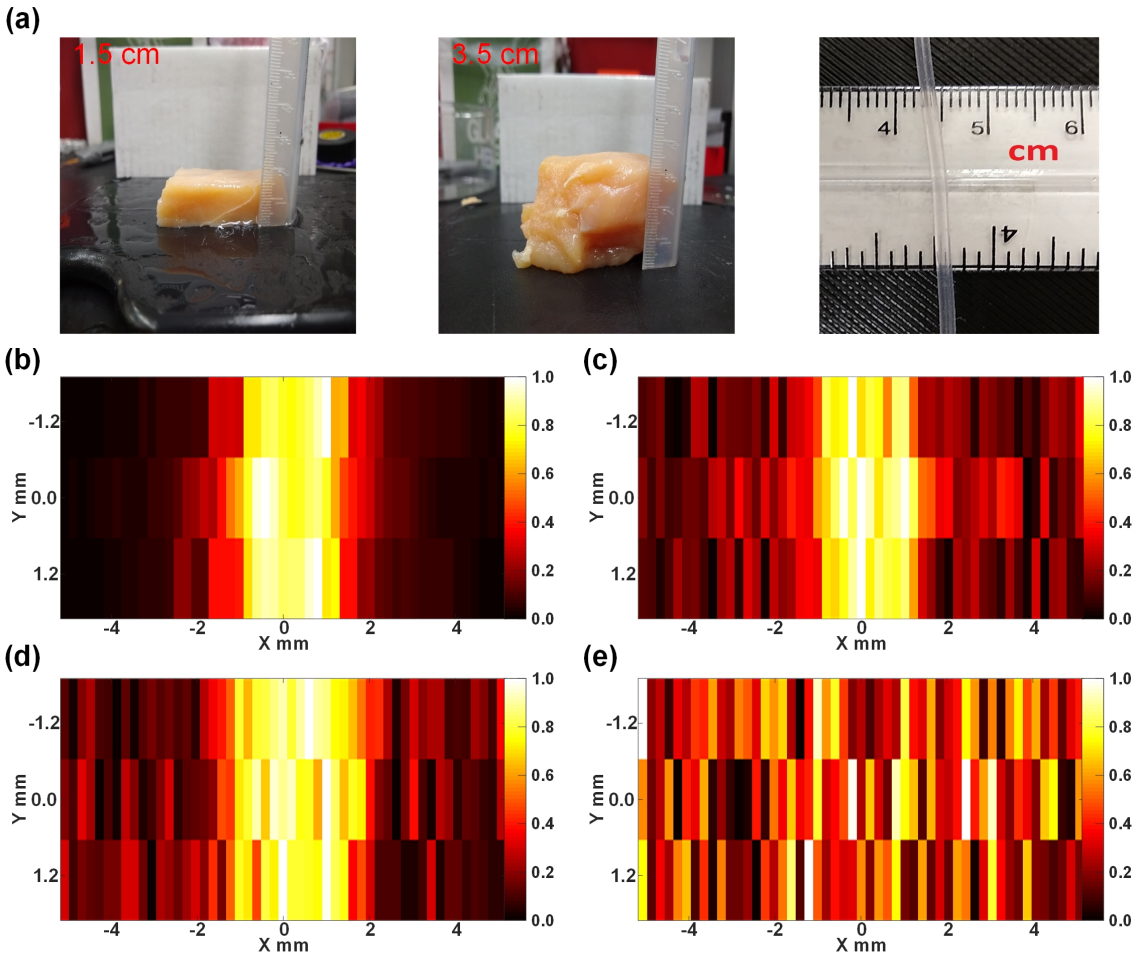

Figure 4-1 (a) Photographs of the silicone tube embedded chicken breast tissue with a thickness of ~1.5 cm and ~3.5 cm, and photo of the as-used real silicone tube in this study. (b, d) 2D USF images of the silicone tube filled with PNIPAM/β-CD/ICG nanogel and (c, e) ICG-PNIPAM nanoparticles in different thickness chicken breast tissue (b,c and d,e represent the tissue thickness of 1.5 cm and 3.5 cm, respectively).

The NIR-USF imaging that uses PNIPAM/β-CD/ICG nanogel to detect light penetrating through ~3.5 cm of chicken breast tissue was significantly improved in comparison with the previously reported NIR-I [62-64] and NIR-II [58, 61, 65-67] imaging results, which even surpassed the maximum depth of detection of ~3.2 cm in pork tissue, using the core/shell α-(NaYbF4: 0.5% Tm3+)/CaF2 nanoparticles as NIR-I imaging probes [68]. Yet for all that, the penetration depth of NIR-USF imaging could be further improved with a USF contrast agent with a larger on-to-off ratio, stronger fluorescence emission, and a narrower transition bandwidth. In short, the PNIPAM/β-CD/ICG nanogel with superior performance will vastly drive the biomedical applications of deep-tissue NIR-USF *in vivo* imaging.

4.3.2 Metabolism and In vivo Biodistribution of the PNIPAM/β-CD/ICG Nanogel

To meet the requirements of the U.S. FDA, all injected contrast agents need to be cleared from the body completely within a reasonable time period [69]. Therefore, an essential understanding of how contrast agents are eliminated from the normal organs/tissues but retained in the tumors is immensely important for their future clinical applications. In light of this necessity, the metabolism of the PNIPAM/β-CD/ICG nanogel (~32 nm) in healthy BALB/c mice was evaluated through tail vein injection. As shown in Figure 4-2(a–c), the fluorescence intensity of the location of the liver reaches peak right after the injection and rapidly decreases within 1 h, indicating that the nanogels can quickly accumulate into the liver tissue through reticuloendothelial system uptake [69] and then decompose fast in a short period. We conjectured that the decomposed PNIPAM/β-CD/ICG nanogel with smaller size in the liver tissue might be principally expelled from the mouse's body through the urinary system. This inference is mainly based on the observation that the bladder region displays a brilliant or saturated fluorescence intensity at 1 h but gradually diminished after 1 h (Figure 4-2(a)), and the locations of the kidney always exhibit strong fluorescence signals after the tail vein injection (Figure 4-2(b) and 4-2(c)). In fact, studies have proved that most small molecular probes are small enough to pass the glomerular capillary walls and enter into the urine if they have no interactions with serum proteins during circulation [69]. This means that the present PNIPAM/β-CD/ICG nanogel are chiefly eliminated from the body through the synergistic pathways of the hepatic route (liver metabolism, bile excretion and feces elimination are involved) and renal clearance. Note that the PNIPAM/β-CD/ICG nanogel almost completely excretes out of the body after 120 h, which is vital for future clinical use. The *ex vivo* biodistribution of PNIPAM/β-CD/ICG nanogel was also examined by recording the fluorescence intensity of major organs dissected from euthanized mice at 15 and 90 min post-injection (Figure 4-2(d)), which further verified the preferential elimination of the nanogels from a normal mouse body mediated by combing the renal (urine) and hepatic (bile to feces) pathways. Moreover, we

observed strong fluorescence signals from mouse hearts and lungs after injection of the as-used nanogels at 15 min, and the signals instantly decreased below the detectable threshold (i.e., 0.3) at 90 min, suggesting the current nanogel could travel through the bloodstream into the heart and lung tissues but could be promptly excreted out of both organs.

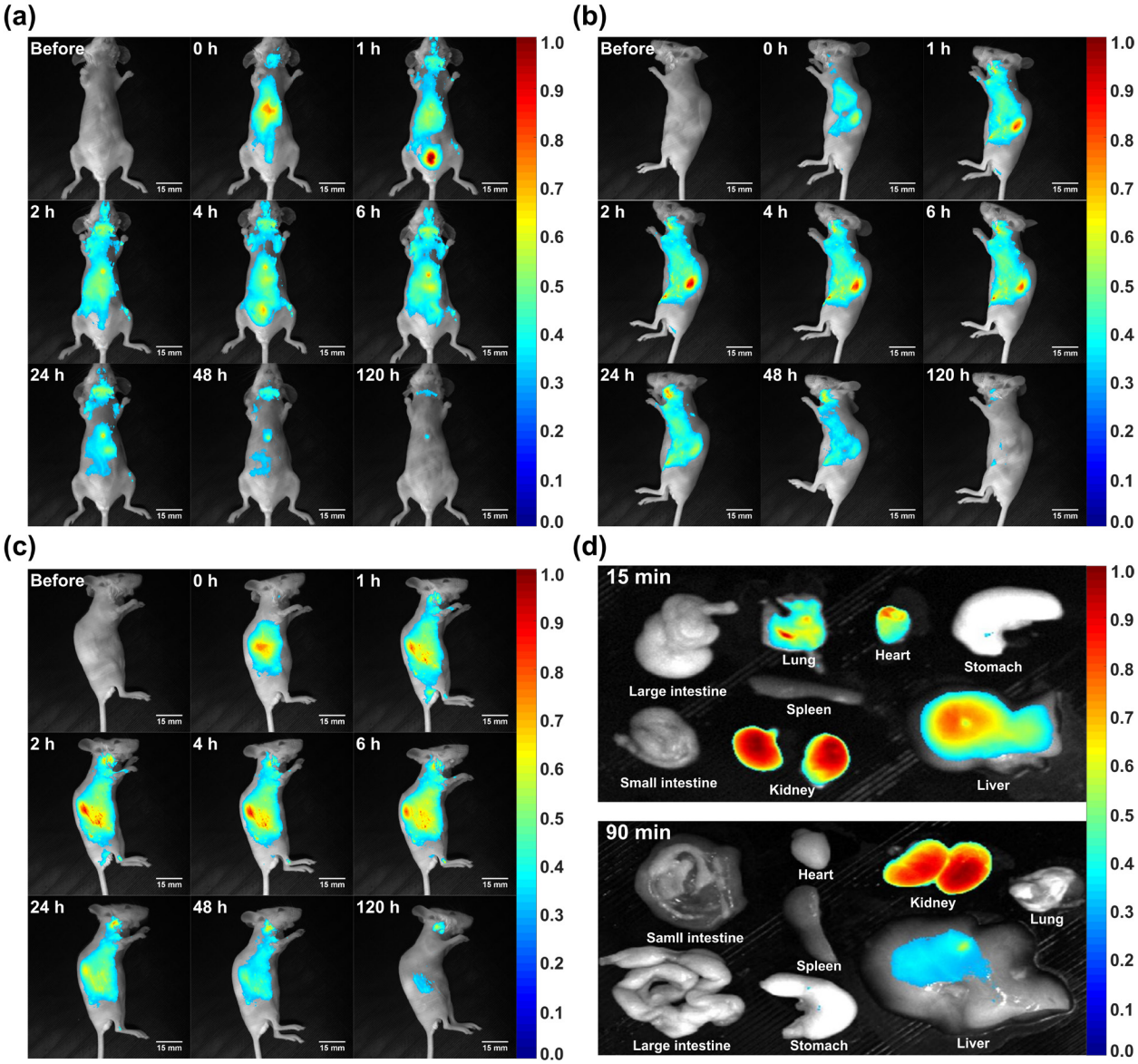

Figure 4-2 Metabolism and *in vivo* biodistribution of PNIPAM/β-CD/ICG nanogel: (a–c) 2D fluorescence images of BALB/c mouse taken at different time points after tail vein injection of PNIPAM/β-CD/ICG nanogel (a–c represent the back side, left side and right side of the mouse body, respectively), and (d) *ex vivo* fluorescence images of major organs dissected at 15 and 90 min post-injection.

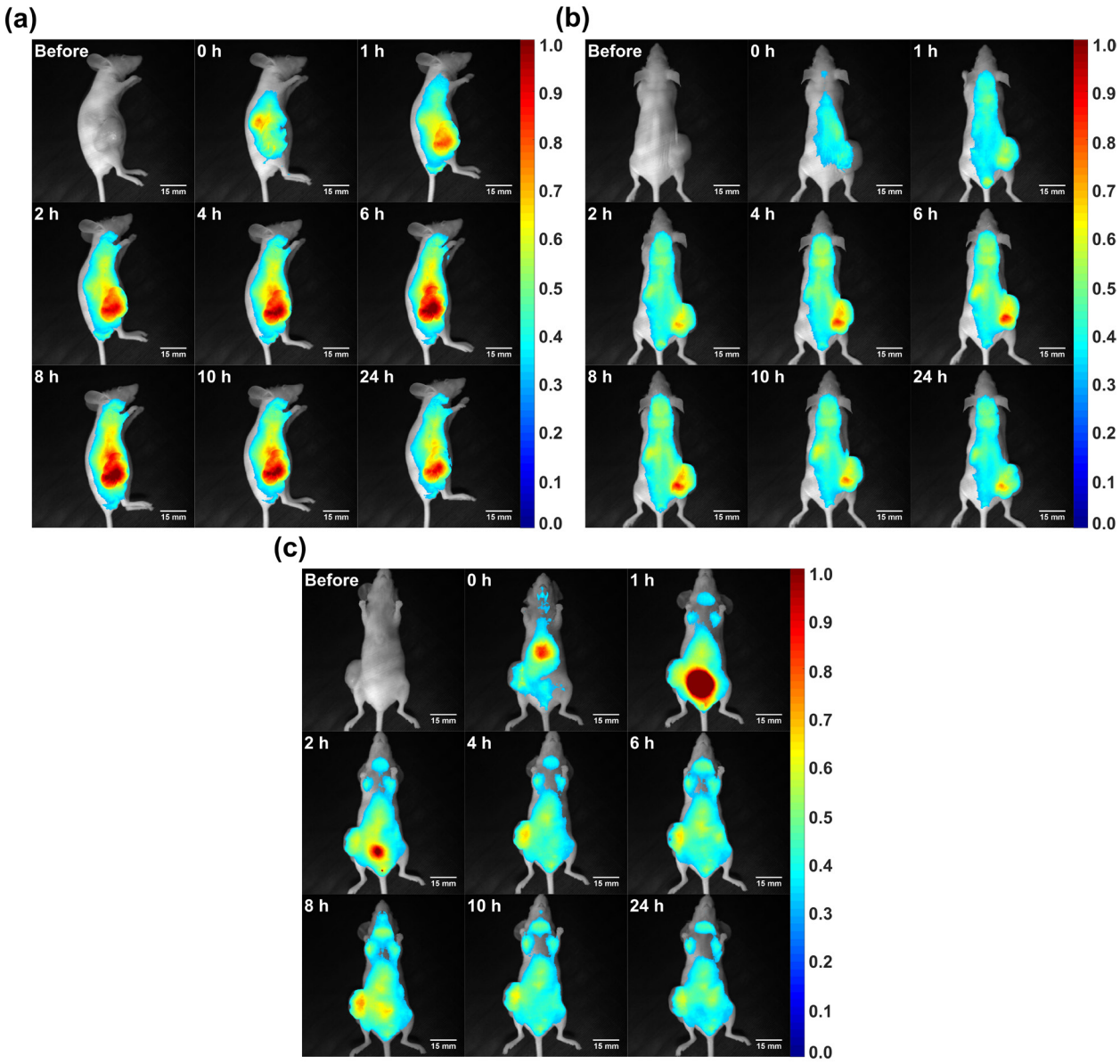

Figure 4-3 Metabolism and *in vivo* biodistribution of the PNIPAM/β-CD/ICG nanogel in U87 brain tumor-bearing mouse: (a–c) 2D fluorescence images of U87 tumor bearing mouse taken at different time points after tail vein injection of the nanogels (a–c represent the right side, dorsal side and ventral side of mouse body, respectively).

As shown in Figure 4-3, the metabolism and *in vivo* biodistribution of PNIPAM/β-CD/ICG nanogel in U87 tumor-bearing mouse was also investigated. The 2D fluorescence images show that the nanogels are broadly distributed throughout the mouse body shortly after injection, within 4 h. Interestingly, the fluorescence intensity in the tumor region gradually increased (1–6 h) and peaked at 8 h, implying the excellent enrichment of nanogels in the tumor via the EPR effect. In contrast, the previously reported ICG-PNIPAM NP with larger hydrodynamic diameter

(~335 nm) was primarily distributed in the spleen and liver. The accumulation effect of ICG-PNIPAM NP in U87 tumor-bearing mouse was relatively low. Thus, the PNIPAM/β-CD/ICG nanogel with an ultra-small size not only has an acceptable and rapid excretion pathway but also its own advantageous EPR accumulation effect in a tumor-bearing mouse.

4.3.3 Ex vivo NIR-USF Imaging of Mouse Liver

Based on the results of the metabolism analysis, we tried to use PNIPAM/β-CD/ICG nanogel to obtain a NIR-USF image of the location of the liver in a live mouse. Unfortunately, we failed to realize *in vivo* NIR-USF imaging of the mouse liver after multiple attempts due to the fast decomposition of the present nanogels in liver. We further carried out the *ex vivo* NIR-USF imaging of the mouse liver to demonstrate whether the USF characteristic of PNIPAM/β-CD/ICG nanogel remained after a tail vein injection. Herein, the mouse was sacrificed at 5 min after a tail vein injection and the liver was harvested, and part of the liver was then inserted into a piece of 1 cm porcine heart tissue for *ex vivo* USF imaging. Specifically, the 2D fluorescence image of the mouse liver embedded in porcine heart tissue is shown in Figure 4-4(a), with the USF scan area marked by a red square. A 3D USF image of the mouse liver embedded in porcine heart tissue appears in Figure 4-4(b). The white dashed circles on the 2D USF images at different depths (Figure 4-4(c–f)) represent the area within which the normalized fluorescence intensity is larger than 0.6. The normalized signal intensity greater than 0.5 is defined as USF signal. The average intensities of USF signal inside and outside the white dashed circles is shown in Figure 4-5. Although the SNR of the USF image is limited, the signal intensity inside the circle is significantly larger than that outside the circle. We speculate that the limited SNR may be mainly caused by the low accumulated concentration of the PNIPAM/β-CD/ICG nanogel inside the liver. These results reveal that the USF property of PNIPAM/β-CD/ICG nanogel is remained (at least partially) after the blood circulation and accumulation/metabolism by the mouse liver. This outcome indicates that the nanogels are physiologically stable in mouse livers, which may benefit for the detection or diagnosis of liver-related diseases in the future. Moreover, exploring other biomedical applications should be also possible in future.

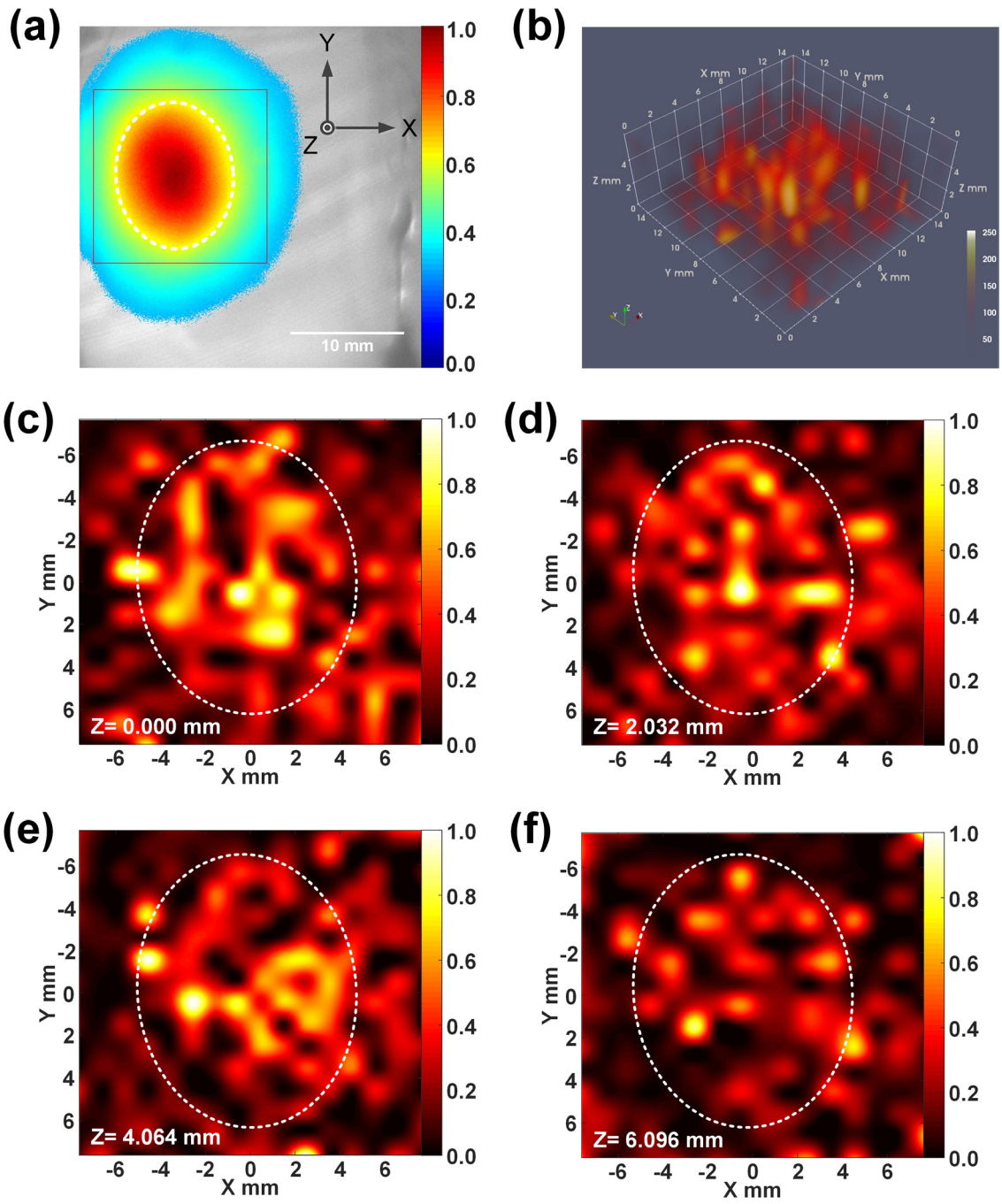

Figure 4-4 (a) 2D fluorescence images of the mouse liver embedded porcine heart tissue, the red square corresponds to the USF scan area in X-Y plane; (b) 3D USF image of the mouse liver; (c–f) the 2D USF image on the X-Y plane at different depths. The white dashed circles in the Figure 4-4(c–f) represent the area within which the normalized fluorescence intensity is larger than 0.6.

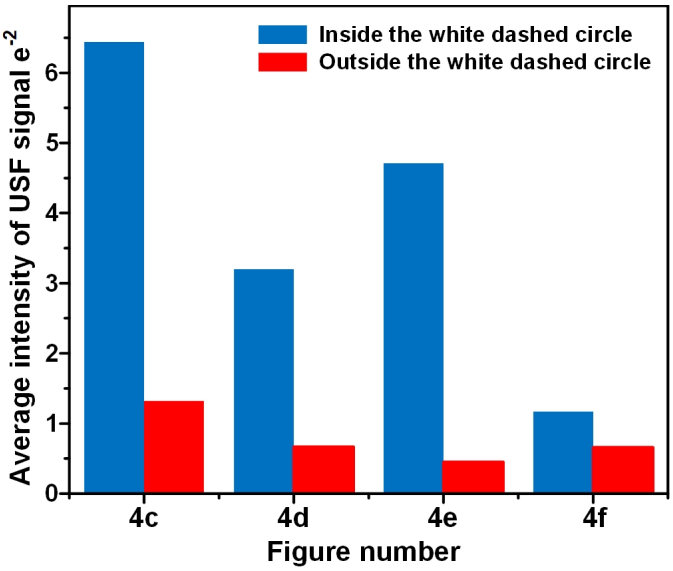

Figure 4-5 The average intensity of USF signal inside/outside the white dashed circle in Figure 4-4(c–f).

4.3.4 In vivo NIR-USF Imaging in U87 Brain Tumor-Bearing Mice

In observations of fluorescence signals in living bodies, various challenges rose due to absorption and scattering, making observation of deep tissue difficult [70]. Hopefully, NIR-USF imaging, as a new technology, will open up great possibilities for comprehensive research into living organisms in deep tissue by a less invasive method. The results from the above *in vivo* biodistribution study reveal that the PNIPAM/β-CD/ICG nanogel can effectively accumulate into the U87 brain tumor of a live mouse via an EPR effect after a tail vein injection (Figure 4-3). Unfortunately, the *in vivo* USF imaging of nanogels distribution in tumor via intravenous injection was not realized after multiple attempts due to insufficient concentration of the nanogels. Hence, the nanogels were injected at two positions with different volumes (35 μL and 20 μL) to form two fluorescence spots for testing the feasibility of USF imaging in the U87 solid tumor. For quantitatively comparing the difference in fluorescence intensity between the tail vein injection and the intratumoral injection in the U87 solid tumor, the ratio of the average fluorescence intensity before and after each injection was calculated. As shown in Figure 4-6, the ratio of the average fluorescence intensity of the nanogels within the white boxes via intravenous injection is 272 (i.e., 4-6(b)/4-6(a) = 45982/169), and the ratio of the average fluorescence intensity of the nanogels within the white boxes via intratumoral injection is 5898 (4-6(d)/4-6(c) = 1220790/207). The results show that the ratio achieved in the intratumoral injection is more than 20-folds greater than that achieved in the tail vein injection (i.e., 5898 vs 272). As shown in Figure 4-7(a), the small and the large spots shown in the 2D planar fluorescence image correspond to the two injection locations with the low and

high doses, respectively. The USF scan area on the X-Y plane is indicated by the red box. The 2D USF images on the X-Y plane at different depths are shown in Figure 4-7(b–f). A 3D USF image of the nanogels distribution inside the solid tumor is shown in Figure 4-7(g). We can see from the Figure 4-7(b–f) that the two USF spots are respectively located in two regions (i.e., Y<0 and Y>0). To quantitatively compare their sizes on each X-Y plane, the pixels with USF signal greater than the half of its maximum USF signal in each spot on each 2D USF image were identified. The area formed by these pixels (in each spot on each 2D USF image) was calculated. As shown in Figure 4-8, the area gradually decreases with the increase of the Z axis from the scanning position Z = 0.00 mm to 8.128 mm. Therefore, we infer that the injected nanogels in both locations are more distributed in the deep tissue (which is close to the Z = 0.00 mm) of the solid tumor than on the superficial tissue (which is close to the Z = 8.128 mm) of the tumor. However, conventional 2D planar fluorescence imaging cannot obtain such 3D fluorescence information in the solid tumor.

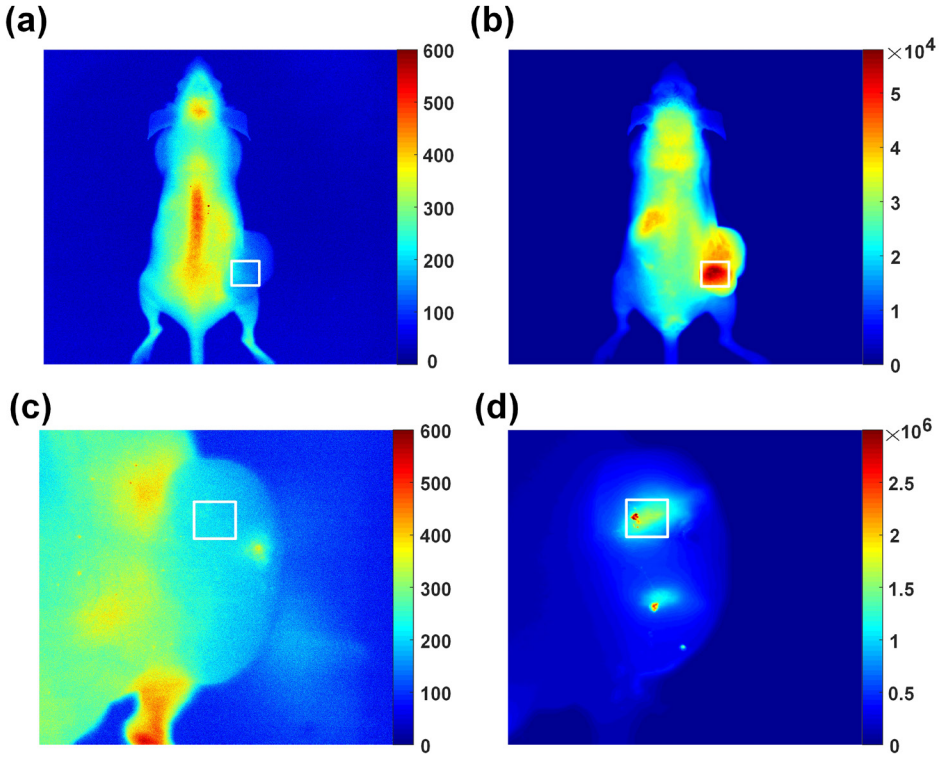

Figure 4-6 2D fluorescence images of U87 brain tumor-bearing mice before and 6 h after tail vein injection (a and b, respectively), and before and after the intratumoral injection (c and d, respectively) of the nanogels.

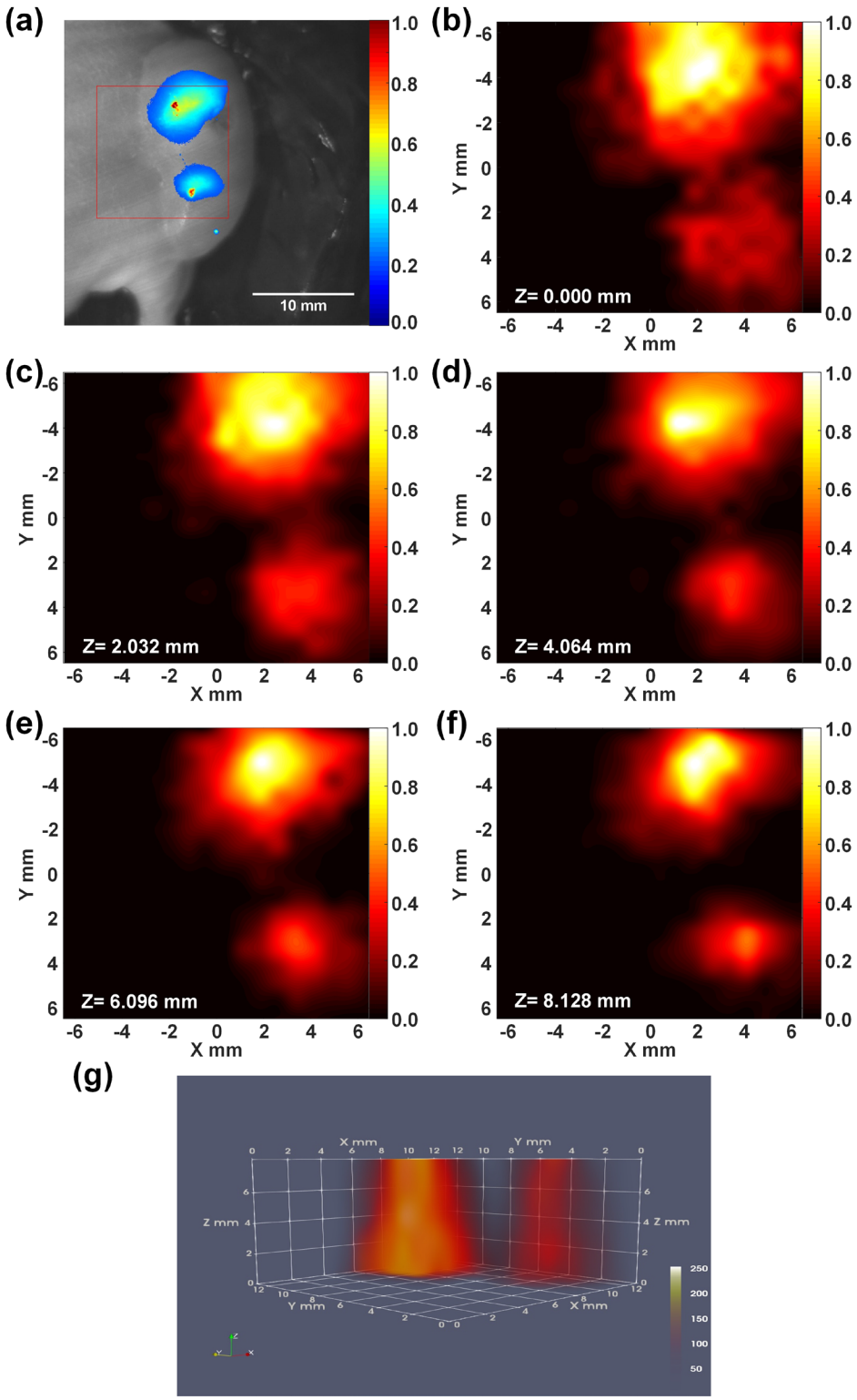

Figure 4-7 (a) The 2D fluorescence image of U87 brain tumor-bearing mouse with two fluorescence spots, the red box corresponds to the USF scan area in X-Y plane; (b–f) the 2D USF images on the X-Y plane at different depths; (g) The 3D USF image of the nanogels distribution at two locations inside the tumor.

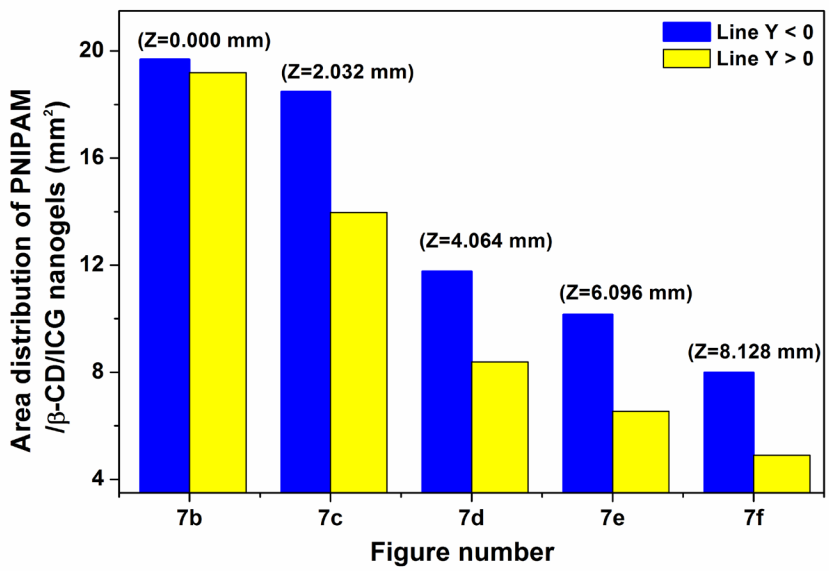

Figure 4-8 The distribution area of the PNIPAM/β-CD/ICG nanogel at each depth. The scanning locations of the Z = 0.00 mm and Z = 8.128 mm are close to the deep and superficial tissues of the U87 solid tumor, respectively.

4.4 Conclusion

The SNR of the NIR-USF image for β-cyclodextrin/ICG-based PNIPAM nanogel is notably improved compared with the ICG-PNIPAM NP in 1.5 and 3.5 cm-thick chicken breast tissues. The *ex vivo* NIR-USF imaging of the mouse liver also confirmed the remarkable stability and biocompatibility of PNIPAM/β-CD/ICG nanogel in biological environment. Animal studies based on U87 tumor-bearing mice revealed that the present nanogels could accumulate into the tumor via an EPR effect. We achieved *in vivo* NIR-USF imaging of nanogel distribution in tumor via local injections. The biodistribution results showed that the nanogels were mainly excreted through the synergistic pathways of the hepatic route and renal clearance. The current study thus outlines the PNIPAM/β-CD/ICG nanogel is a promising NIR-USF probe for deep tissue and high-resolution NIR-USF imaging. The work in this chapter has been published in Nano Research [38].

Chapter 5

IMPROVING SENSITIVITY AND IMAGING DEPTH OF USF VIA AN EMCCD-GAIN-CONTROLLED SYSTEM

5.1 Introduction

NIR fluorescence can penetrate biological tissue several centimeters via scattering, which enables deep tissue NIR fluorescence imaging. Unfortunately, it suffers from poor spatial resolution in centimeters-deep tissue because of tissue's high scattering property. In recent years, many researchers are interested in improving the spatial resolution of NIR fluorescence imaging in centimeter-deep tissues via various strategies, such as NIR-II fluorescence [68, 71-73], ultrasound-pulse-guided digital phase conjugation [20], ultrasound-modulated fluorescence [12, 15, 28] and ultrasound-induced temperature-controlled fluorescence [16-18, 24].

Adopting excitation and/or emission light at the NIR-II window (950 -1700 nm) can significantly reduce tissue's light scattering and has shown promising results in centimeter-deep tissues. For example, a study adopted 980 nm excitation light with strong intensity of ~300 mW/cm^2 and detected ~800 nm emission light (via upconversion) to image a 3.5 mL cuvette filled with core/shell nanoparticles and covered by a piece of 3.2 cm-thick porcine muscle tissue [68]. Another study also used 980 nm excitation light with strong intensity of ~500 mW/cm^2 and ~1100 nm emission light to image structures (a few millimeters) in a 6 cm-deep muscle tissue via a DOLPHIN imaging system [71]. However, some concerns may exist when applying these methods for clinical uses: the biocompatibility and toxicity of the adopted NIR-II contrast agents, and potential significant heating effect of the high intensity excitation light (in order to obtain enough signal photons) on tissue due to the high absorption coefficient of water in tissues at NIR-II region.

During the past years, we developed a new imaging technique, USF, to achieve high-resolution fluorescence imaging in centimeters-deep tissue. The ultrasound-switched-on fluorescence emission (via a thermal sensitive contrast agent) was confined within the ultrasound focal volume (or the ultrasound-induced thermal focal volume depending on the fluorescence detection time of the system) to obtain the fluorescence image with an ultrasound or ultrasound-scaled spatial resolution. Several ICG-based USF contrast agents have been developed to take the advantage of the large penetration depth of the NIR-I photons [24, 31, 38, 74]. The β-cyclodextrin/ICG complex-encapsulated poly(N-isopropylacrylamide) (PNIPAM) nanogel (ICG-nanogel) was recently developed in our lab [38] As shown in Chapter 4, USF imaging using ICG-nanogel was successfully demonstrated *in vitro*, *ex vivo* and *in vivo*. It showed an improved SNR in USF imaging in a piece of 3.5 cm-thick chicken breast tissue compared with ICG-

PINIPAM NP. In this study, we will use this ICG-nanogel as a comparison. While this ICG-nanogel showed a promising USF performance, the adopted material of PNIPAM might generate a safety concern due to the potential toxicity of its monomers (NIPAM) to living cells. To address this concern, the biocompatible ICG-liposomes were recently developed in our lab by encapsulating the ICG dye into 1,2-dipalmitoylsn-glycero-3-phosphocholine (DPPC)-based liposomes. *In vitro*, *ex vivo* and *in vivo* USF images were successfully achieved using this novel contrast agent [74]. However, one disadvantage of this 1st-generation ICG-liposome is its large hydrodynamic size (~7 μm), which is too large and limits its *in vivo* application. Therefore, reducing its size is highly desired. In this study, an ICG-liposome with reduced hydrodynamic size (181 nm) was used, and its USF performance was found superior to that of the ICG-nanogel.

As shown in Chapter 3, we demonstrated that an EMCCD camera-based USF imaging system could well overcome the limitations of our previous USF imaging systems in which a single-fiber was used to collect photons to a photomultiplier tube, including the improved photon collection efficiency via the EMCCD camera and related lenses, and the increased imaging speed by adopting a Z-scan method. To apply the Z-scan method, the USF dynamic pattern was studied to determine the time interval and space interval between two sequential scan points to avoid signal interference induced by the thermal diffusion. However, the EM gain was observed to be unstable when recording a sequence of images after responding the external hardware trigger which was used to synchronize the camera with other devices (such as an ultrasound transducer and an translation stage). Therefore, the advantage of the EMCCD camera was not fully taken in our previous study in which an EM gain of 1 was adopted to achieve stable USF signals. However, to image much deeper tissue (such as >3 cm in chicken breast tissue), USF photons need to be significantly amplified so that they can clearly outstand from the background photons and be clearly differentiated from the noise caused by the background photons. To achieve this goal, a relatively stable gain is required. Therefore, instead of using the hardware trigger mode, in this study we adopted a software trigger mode by using MATLAB (The MathWorks, Inc. USA) to control the software of the EMCCD camera (i.e., LightField from the manufacturer). This software trigger mode not only simplified the system but also reduced the temperature-induced EM gain variation. Our results showed this software trigger mode could provide a more stable gain compared with the hardware trigger mode. The SNRs of USF images with different EM gains in various thick tissues were also studied. By combining the improved ICG-liposome and the USF imaging system, we successfully achieved the USF imaging of a sub-millimeter

silicone tube (inner diameter: 0.76 mm, outer diameter: 1.65 mm) embedded in 5.5 cm-thick chicken breast tissue using an excitation laser with a low intensity of 28.35 mW/cm^2.

5.2 Materials and Methods

Here I would like to acknowledge my colleague Mr. Yang Liu, who developed the ICG-liposome used in this study.

5.2.1 ICG-Liposome Synthesis

The ICG-liposome was synthesized based on the previously reported method with modifications [74]. First, the ICG solution was prepared by dissolving the ICG dye (Chem-Impex Int'L Inc., USA) in chloroform (99.9% pure) and ethanol mixture (4:1 v/v) at a concentration of 0.28 mg/mL. 5.0 mg DPPC (Avanti, USA) was dissolved with 2 mL chloroform in a 50 mL round flask and 0.2 mL of the prepared ICG solution was added later. After a well-mixing of the solution, the solvent was evaporated using a rotary evaporator (BUCHI Corp., USA) at 150 rpm with -80 kPa vacuum in a 55 ˚C water bath for at least 30 min to form a thin lipid layer on the wall of the round flask. Afterward, 0.8 mL hydration water, which was made by mixing 95 % PBS (pH 7.4) and 5 % glycerol (99.8% pure), was added into the flask and swirled at 55 ˚C for 1 min and then rotated for 1 hour at 150 rpm in a 42 ˚C water bath. Then, the ICG-liposome solution was vortexed using the amalgamator (DB338, Medical Instrument Co., Ltd, China) for 1 min. The obtained ICG-liposome was diluted to a final volume of 3.5 mL. Thus, theoretically, the maximum ICG concentration is 0.016 mg/mL (0.28 mg/mL × 0.2 mL /3.5 mL). A freeze-thaw-mix cycle was performed for 5 times by freezing the ICG-liposome in dry ice for 8 min and then transferred the ICG-liposome into a 60 ˚C water bath to thaw for 5 min followed by shaking the sample for 2 min with a shaker at 250 rpm. To control and uniform the size of liposome vesicles, an extrusion method was conducted with a mini-extruder (Avanti, USA). A 200 nm polycarbonate filter (Whatman, UK) was utilized and the ICG-liposome was extruded at 50 ˚C for 19 times. The obtained ICG-liposome was stored at 4 ˚C. All chemicals were purchased from Fisher Scientific International, Inc., USA.

5.2.2 An In-House Built Temperature-Controlled Fluorescence Spectrometer

An in-house built temperature-controlled fluorescence spectrometer system was developed to study the fluorescence intensity change of the USF contrast agents versus the solution temperature. A 3.5 mL quartz cuvette (Hellma, Germany) was filled with 3 mL sample and placed into a temperature-controlled sample compartment (qpod 2e, Quantum Northwest, Inc., USA; temperature precision: ±0.01 ℃; temperature accuracy: ±0.15 ℃ from -20 ℃ to

+105 ℃). The solution temperature was measured by the qpod system via inserting a thermometer probe (WD-93824-00, Oakton, USA; temperature accuracy: 0.1°C from 0 to 70 °C) into the sample. The excitation light with a wavelength of 808 nm generated by a laser (MGL-II-808-2W, Dragon lasers, China) was passed through the open window on the cuvette holder and delivered to the sample via a fiber bundle. The emitted fluorescence from the sample was filter by a longpass filter (BLP01-830R-25, Semrock Inc., USA) and collected by a modular USB spectrometer (USB2000+, Ocean Insight, USA) attached to the cuvette holder at a 90-degree angle from the excitation light beam. A MATLAB based program was developed to read the solution temperature from the interface of the Q-Blue software (the Quantum Northwest, Inc., USA) which controlled the cuvette holder. The spectrometer received the commands from the program to acquire the spectrum at the preset temperature points automatically during the heating of the sample.

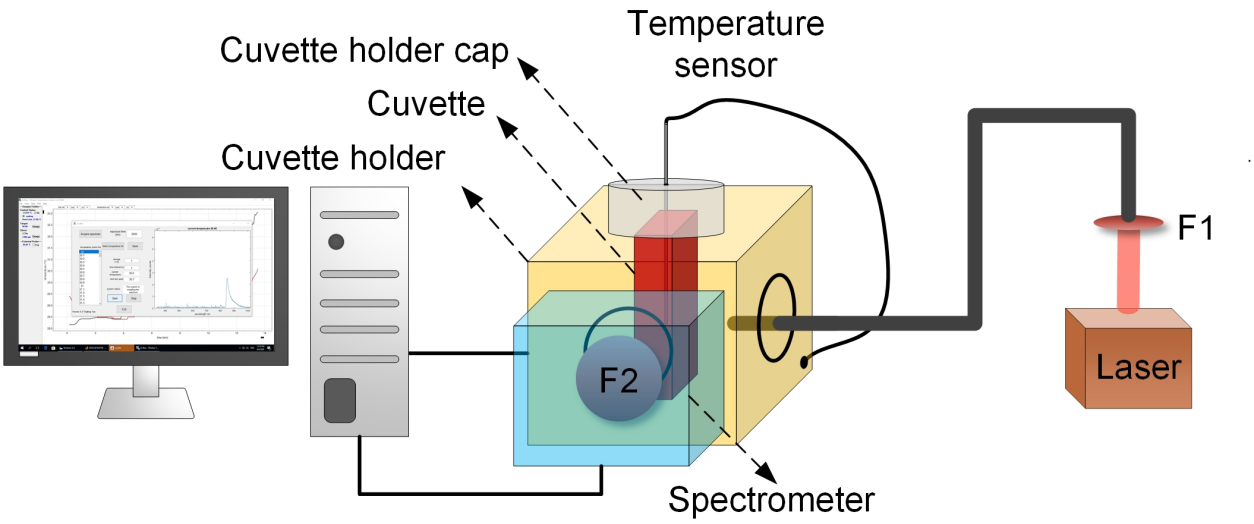

Figure 5-1 Schematic diagram of the temperature-controlled fluorescence spectrometer system. F1: excitation filter (785/62 BP); F2: emission filter (830LP).

5.2.3 ICG-Liposome Characterization

Three independently synthesized ICG-liposome samples were tested by the in-house built fluorescence spectrometer system with same setting parameters. The wavelength of the excitation light was 808 nm and the emitted fluorescence was filtered by a 830 nm-longpass filter. The preset solution temperature of the sample was increased from 35.0 ℃ to 45.0 ℃ with an increment of 0.1 ℃ (limited by the precision of the thermometer probe). The exposure time of the spectrometer was 100 ms. The fluorescence intensity at each temperature point was calculated by summing

the acquired spectrum data from 830 nm to 1020 nm. The hydrodynamic size of the ICG-liposome was measured using a dynamic light scattering (DLS, NanoBrook 90PlusPALS, Brookhaven Instruments, USA) system at room temperature. The sample was diluted 100 times with PBS buffer before conducting the measurement to avoid aggregation.

5.2.4 EMCCD-Based USF Imaging System

The schematic diagram of the proposed USF imaging system in this study is shown in Figure 5-2(a). It was improved from the previously developed EMCCD based USF imaging system (Figure 3-1). Briefly, the excitation laser with a wavelength of 808 nm (MGL-II-808-2W, Dragon lasers, China) was driven by the first function generator (FG1, 33500B, Agilent, USA). The output light was filtered by a bandpass filter (FF01-785/62-25, Semrock Inc., USA) and coupled into a dual branch light guide (¼" x 72", Edmund Optics Inc., USA). To make uniform illumination, the tissue sample placed in a water tank was illuminated by the excitation light from two opposite directions. The emitted fluorescence from the contrast agents transmitted through two 2-inch longpass filters (BLP01-830R-50, Semrock Inc., USA), a camera lens (AF NIKKOR 50 mm f/1.8D Lens, Nikon, Japan), a 1-inch longpass filter (BLP01-830R-25, Semrock Inc., USA) and received by the EMCCD camera (ProEM®-HS:1024BX3, Princeton Instruments, USA) with a field of view around 4 cm × 4 cm (slightly variant when imaging different thick sample because of adjusting lens focus). The driving signal from the second function generator (FG2, 33500B, Keysight Technologies, USA) was amplified by a 50 dB-gain RF-AMP (A075, E&I, USA), passed through a MNW and delivered to a 2.5 MHz HIFU transducer (H-108, Sonic Concepts Inc., USA). To realize the sample scanning, the HIFU transducer was mounted to a three-axis motorized translation stage (Xslide™ and VXM™, Velmex Inc., USA). The temperature of the water was controlled at 37 ℃ by a temperature controller system (PTC10, Stanford Research Systems, USA). A magnetic stirrer along with a long magnetic bar (11-100-16S, Fisher Scientific, USA) was used to uniform the water temperature. A MATLAB based program was developed to synchronize three different parts in the system, including ultrasound generation, camera exposure and HIFU transducer movement. The time sequence of the system is shown in Figure 5-2(b). At each scanning point, the program controlled the camera to take an image with an exposure time of 1.5 s before the ultrasound exposure (i.e., heating) as a background used for signal processing. The FG2 then received a trigger from the MATLAB program in the computer through a multifunctional input/output device (I/O, PCIe-6363, National Instruments, USA), and generated a sinusoidal wave (frequency: 2.5 MHz, duration time: 0.4 s) to drive the HIFU transducer. Immediately after the ultrasound heating, another image with the same exposure time was acquired by the

EMCCD camera. The increase of the fluorescence intensity between the two images was considered as the USF signal. After camera exposure, the MATLAB program controlled the translation stage to move the HIFU transducer to the next scanning point. To avoid the thermal diffusion-induced signal interference, the time interval between two adjacent scanning points was 10 s.

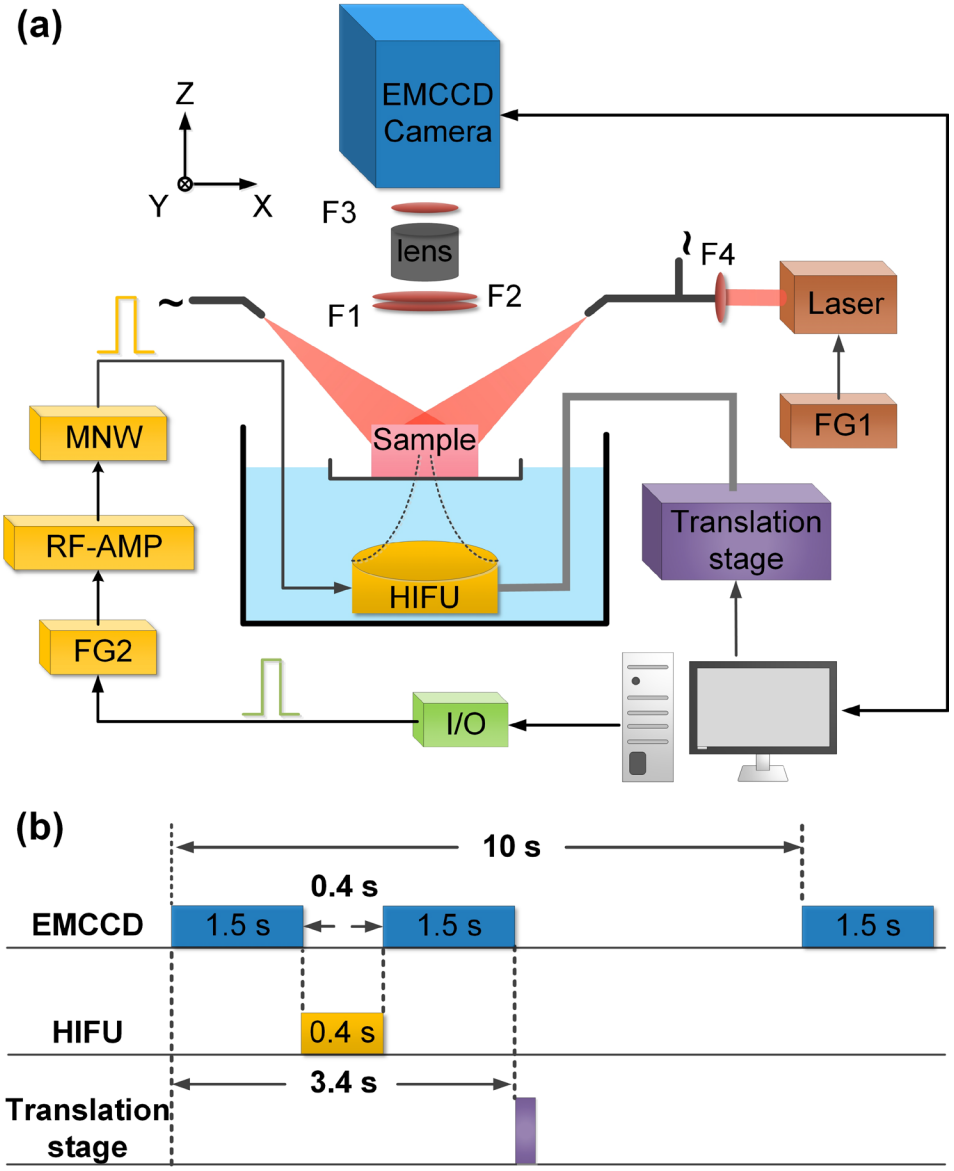

Figure 5-2 (a) A schematic diagram of the improved EMCCD-based USF imaging system. HIFU: high intensity focused ultrasound; MNW: matching network; RF-Amp: radio-frequency power amplifier; FG: function generator; I/O: multifunctional input/output device; F1–F3: emission filters (830 LP); F4: excitation filter (785/62 BP). (b) A time sequence diagram of the USF imaging system.

5.2.5 USF Imaging of a Sub-Millimeter Silicone Tube Embedded in Chicken Breast Tissues

A sub-millimeter silicone tube (inner diameter: 0.76 mm, outer diameter: 1.65 mm, ST 60-011-04, Helix Medical, USA) was inserted into a piece of chicken breast tissue at a height of ~5 mm from the bottom surface to simulate a blood vessel. Since the thickness of a single piece of chicken breast tissue was limited (i.e., ≤ 3cm), another one (for thickness: 3.5 cm, 4.5 cm or 5.0 cm) or two (for thickness: 5.5 cm) pieces of chicken breast tissue were stacked on the first one where the silicone tube was embedded to obtain the targeted thickness. The multiple-piece tissue was placed on a transparent parafilm (PM-992, BEMIS Company Inc., USA) that was used to seal an open window at the bottom center of a small plastic box. In order to maintain the ultrasound coupling, ultrasound gel (Aquasonic 100, Parker Laboratories Inc., USA) was used to fill the gap between the parafilm and the tissue. The top surface of the tissue was also covered by ultrasound gel and parafilm to keep it from drying out during the experiment. The USF contrast agents were injected into the silicone tube via a syringe. The silicone tube was washed after each experiment by injecting water and filled with new contrast agent solution for the next experiment. The bottom of the small plastic box was immersed into a water tank (water temperature: 37 ℃) to keep the USF contrast agents at body temperature. An area of 8.128 (X) × 4.064 (Y) mm^2 (step size in X direction: 0.2032 mm; in Y direction: 2.032 mm) was raster scanned by the ultrasound focus with an estimated ultrasound power of 1.74 W under various EM gains. The maximum applicable EM gain was limited by the dynamic range of the camera (0 to 65535 counts). The intensity of the excitation light illuminated on the tissue surface was 28.35 mW/cm^2 (Power: 20.10 mW, sensor's area: 0.709 cm^2) measured at the center of the illumination spot on the tissue surface via a photodiode power sensor (S120C, Thorlabs Inc., USA) and a power and energy meter (PM100D, Thorlabs Inc., USA).

5.2.6 The Comparison of the EM Gain Stability between the External Hardware Trigger Mode and the MATLAB Trigger Mode

To investigate the stability of the EM gain under different trigger modes, a weak and stable light source is needed to illuminate the EMCCD camera. Tissue's autofluorescence is a reasonable light source for this purpose because it is weak under the 808 nm excitation and also stable in a short period time. A brief discussion about the background photons is given here. In USF imaging, it is common that some background photons can be detected, which are independent of ultrasound and usually consist of tissue autofluorescence, excitation light leakage from the laser, and/or non-100%-off fluorescence from the USF contrast agent. Usually, the excitation light leakage has been well minimized by using the multiple and high-quality emission filters, which should not be dominant in the

background photons. When the silicone tube is injected with water only, the background photons should not have any fluorescence photons from the non-100%-off fluorophores. Thus, the major light source is from the tissue autofluorescence.

The comparison of the external hardware trigger mode and the MATLAB trigger mode was realized in the same silicone tube embedded in 5.0 cm-thick chicken breast tissue. The silicone tube was filled with water during the experiment. Briefly, the only difference between the two trigger modes was the trigger source. All the parameters of the EMCCD camera (e.g., exposure time, number of frames, EM gain and trigger response) were set via the LightField software (Princeton Instruments, USA). In external hardware trigger mode, the trigger response was set as 'Start on a single trigger' which means the camera won't begin to take the images until the trigger circuit detected the rising edge of an external hardware trigger. In MATLAB trigger mode, the Lightfiled received commands from MATLAB via software interface (provided by the manufacturer) to control the camera to take the images. The trigger response was set as 'No response' which means the trigger circuit did not work and the camera will not respond to the external hardware trigger. In this experiment, the camera exposure time of each frame image was 0.2 s and a total of 25 images were acquired continuously. The EM gain was set as various values (i.e., 1, 9, 27 or 81). All the other parameters of the Lightfield were set as default values.

5.2.7 Compare the ICG-Liposome and the ICG-Nanogel

The ICG-nanogel was synthesized according to the previously proposed protocol [38]. To compare the ICG-nanogel with the ICG-liposome, the concentration of the initial ICG (i.e., the mass of the initial ICG divided by the volume of the final solution) was remained the same (0.016 mg/mL) by diluting the synthetized ICG-nanogel solution (0.056 mg/mL). The synthesized ICG-nanogel was tested by the in-house built fluorescence spectrometer with the same setting parameters used for the ICG-liposome. The comparison of USF imaging performance between the ICG-liposome and the ICG-nanogel were realized in the same silicone tube embedded in 2.5 cm-thick chicken breast tissue. The EM gain was set as 1 for both contrast agents.

5.2.8 Calculation of Image's SNR

Along the y axis, each USF image had three lines and each line had 41 scan points. From each line, we could calculate a SNR value based on the following definition. The SNR of each USF image was defined as the mean of the three SNRs of the three lines. The background defined as the average of the 12 scan points at the two edges of each

line (i.e., 8 points at each edge, two maximum values and two minimum values of the total 16 points were excluded) was subtracted first. To calculate the SNR of each line, the noise was defined as the standard deviation of the 12 scan points (used for calculating the background) and the signal was defined as the root-mean-square of the maximum six signal values from the 11_{th} to 31_{th} scan points (the silicone tube was shown in this range). The SNR was then calculated by the following equation:

$$SNR = 20\log_{10}\frac{Signal}{Noise}.$$

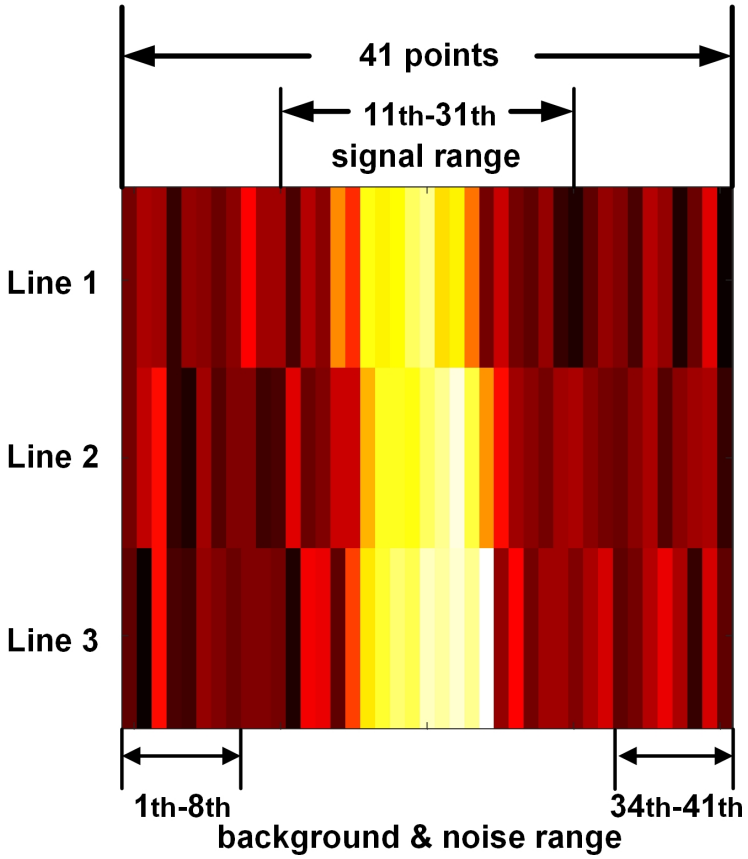

Figure 5-3 The schematic diagram of SNR calculation.

5.3 Results

5.3.1 The ICG-Liposome Characterization

As shown in Figure 5-4(a), the fluorescence intensity of the ICG-liposome increases with the rise of the solution temperature and the LCST is 38.4 ˚C (defined as where the slope of the curve was 10% of its maximum value). The fluorescence intensity increases 2.02 folds when the temperature rises from 38.4 ˚C to 40.4 ˚C. As shown in Figure 5-4(b), the hydrodynamic size of the ICG-Liposome is 181.0 ± 58.1 nm. The polydispersity is 0.126.

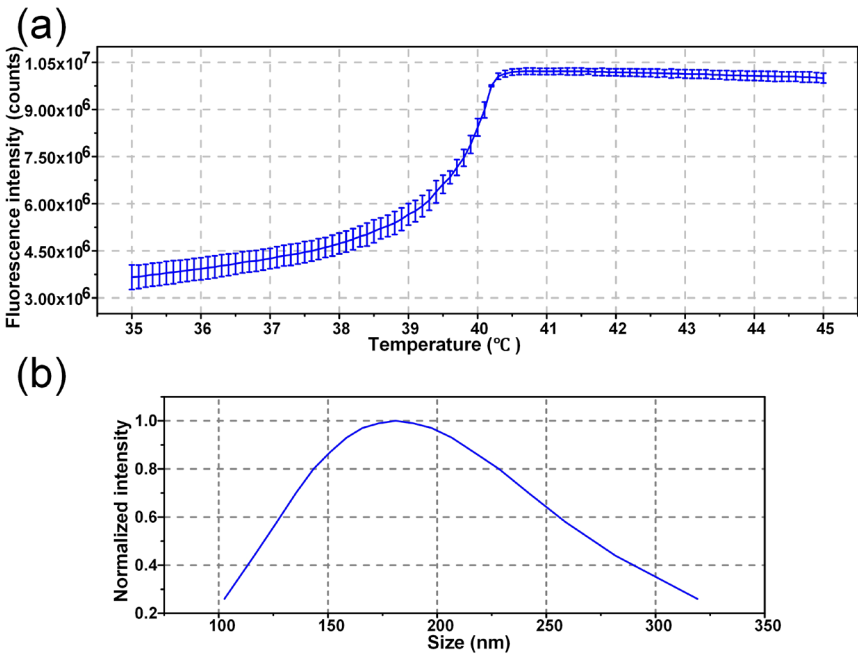

Figure 5-4 (a) The fluorescence intensity of ICG-liposome versus the solution temperature. (b) Hydrodynamic size of the synthesized ICG-liposome.

5.3.2 The Comparison of the EM Gain Stability between the MATLAB Trigger Mode and the External Hardware Trigger Mode

Figure 5-5(a) shows the first frame of the 25 images taken by the EMCCD camera with an EM gain of 1 in MATLAB trigger mode. Figure 5-5(b–d) show the mean intensity (i.e., spatial average value of the whole 2D fluorescence image) of the acquired 25 frames using MATLAB trigger mode (blue line with squares) and the hardware trigger mode (red line with circles) with an EM gain of 1, 9 and 81, respectively. As shown in Figure 5-5(b), the mean intensities of the two modes are fluctuated and similar to each other when the EM gain is 1. As shown in Figure 5-5(c) and 5(d), the mean intensity of the MATLAB trigger mode is higher and more stable than that of the external hardware trigger mode with an EM gain of 9 or 81. The curve of the hardware trigger mode continuously rises with a higher increase rate at the beginning. Figure 5-5(e) shows the normalized mean intensity using the MATLAB trigger mode with an EM gain of 9 (green line with squares), 27 (red line with circles), and 81 (blue line with triangles). The maximum decrease of the mean intensity is less than 1% and the higher EM gain leads to slightly more intensity decrease. However, when using external hardware trigger mode (Figure 5-5(f)), the maximum increase of the mean intensity can reach as high as ~10% and the higher EM gain leads to a higher intensity increase.

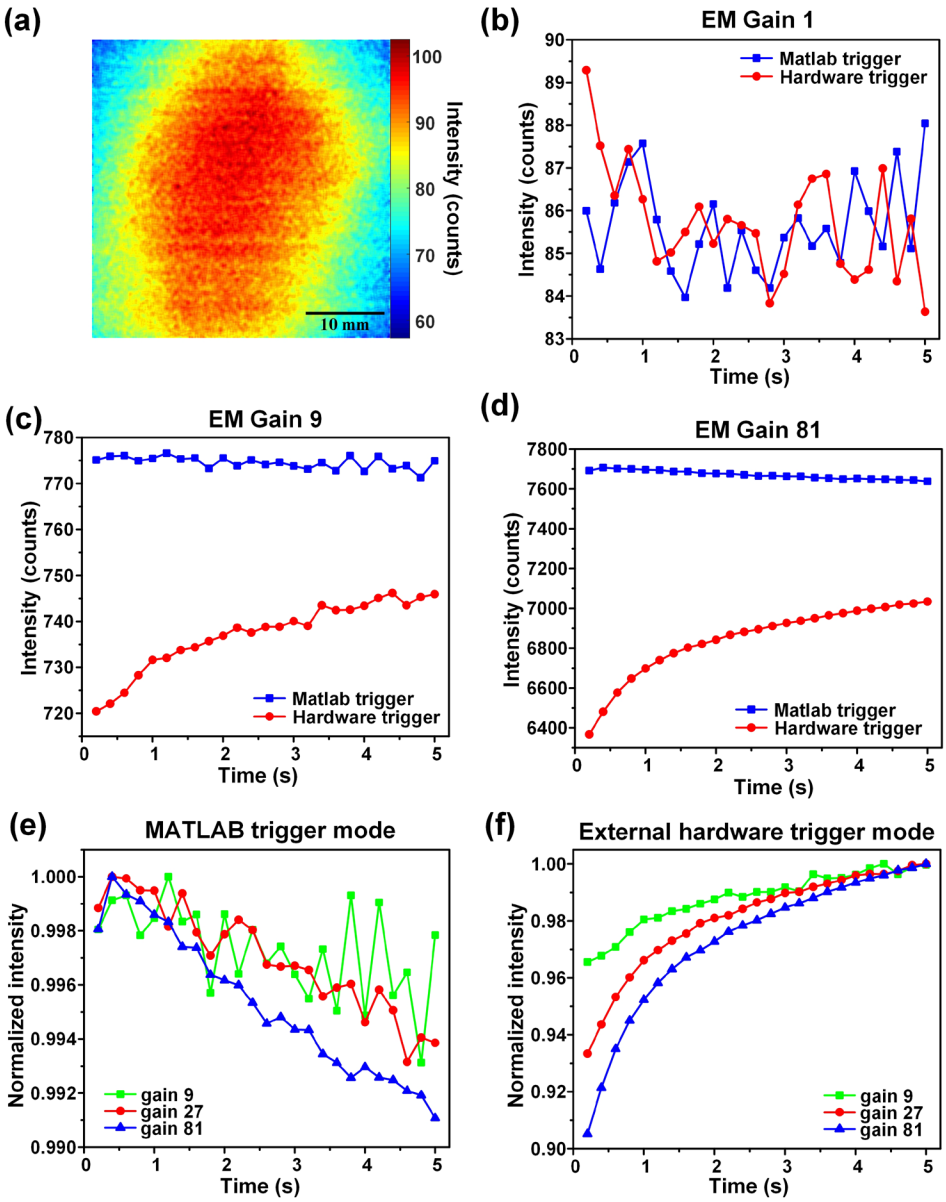

Figure 5-5 (a) The first frame of the images taken by the camera with an EM gain of 1 in MATLAB trigger mode. The mean intensity of the acquired 25 frames in MATLAB trigger mode (blue line with squares) and external hardware trigger mode (red line with circles) with an EM gain of (b) 1, (c) 9 and (d) 81. Normalized mean intensity curve using (e) MATLAB trigger mode and (f) external hardware trigger mode with an EM gain of 9 (green line with squares), 27 (red line with circles), and 81 (blue line with triangles).

5.3.3 Background Images and Background Fluorescence Images of the Tissue Samples

A background image (I_{BG}) is defined as the image acquired by the EMCCD camera when the silicone tube is filled with water (i.e., no USF contrast agents are injected, and no ultrasound is exposed). The background image is

usually formed by tissue's autofluorescence (I_{AF}) and also some minor excitation photons leaked through the emission filters from the laser due to the imperfect property of the emission filters (I_{EL}). In general, we have $I_{BG} = I_{AF} + I_{EL}$. When the silicone tube is filled with the USF contrast agent solution, one more component, i.e., the background fluorescence (I_{BGF}) from the non-100%-off contrast agents, is included in the acquired image (i.e., $I_{UCA} = I_{BGF} + I_{BG} = I_{BGF} + I_{AF} + I_{EL}$). Again, no ultrasound is applied when acquiring these images. Thus, by subtracting the image acquired when the tube is filled with water (I_{BG}) from the image acquired when the tube is filled with USF contrast agent (I_{UCA}), we can have the background fluorescence image (i.e., $I_{BGF} = I_{UCA} - I_{BG}$), which is generated only from the non-100%-off USF contrast agent because tissue's autofluorescence (I_{AF}) and the laser leakage (I_{EL}) have been subtracted.

When the EM gain is set to 1, Figure 5-6(a–e) show the white light photo, background image (i.e., I_{BG}, tissue's autofluorescence and laser leakage) and the background fluorescence image (i.e., I_{BGF}, fluorescence coming from the non-100%-off USF contrast agent) of the silicone tube embedded in chicken breast tissue with a thickness of 2.5, 3.5, 4.5, 5.0 and 5.5 cm, respectively. The average intensity (the spatial average of the whole 2D image) of these figures are quantitatively shown in Figure 5-6(f). The average intensity of all the background images (I_{BG}) acquired with different tissue thickness is similar to each other (444, 573, 533, 545 and 564 counts corresponding to 2.5, 3.5, 4.5, 5.0 and 5.5 cm, respectively). This is because the background photons are from tissue's autofluorescence and laser leakage, which are usually independent of tissue's thickness when the thickness is large enough (such as ≥3.5 cm in this example). However, the average intensity of all the background fluorescence images (I_{BGF}) reduces dramatically with the increase of the tissue thickness (5113, 706, 182, 88 and 56 counts corresponding to 2.5, 3.5, 4.5, 5.0 and 5.5 cm, respectively). When tissue thickness >3.5 cm, the background fluorescence intensity (I_{BGF}) becomes smaller than the background intensity (I_{BG}). This result is understandable because the background fluorescence photons are mainly caused by the non-100%-off USF contrast agents in the tube. When increasing the depth of the tube in tissue samples, the fluorescence intensity will exponentially decay due to tissue's scattering and absorption and the attenuation of the excitation light in tissue. When depth is small enough, the background fluorescence intensity (I_{BGF}) may be higher than the background intensity (I_{BG}) depending on the fluorophore concentration, its emission efficiency and the excitation light intensity. This happens in this example when tissue thickness is 2.5 and 3.5 cm. With the increase of the depth, the background fluorescence intensity (I_{BGF}) reduces so quickly that it may be lower than the background intensity (I_{BG}). This happens in this example when tissue thickness is >3.5 cm.

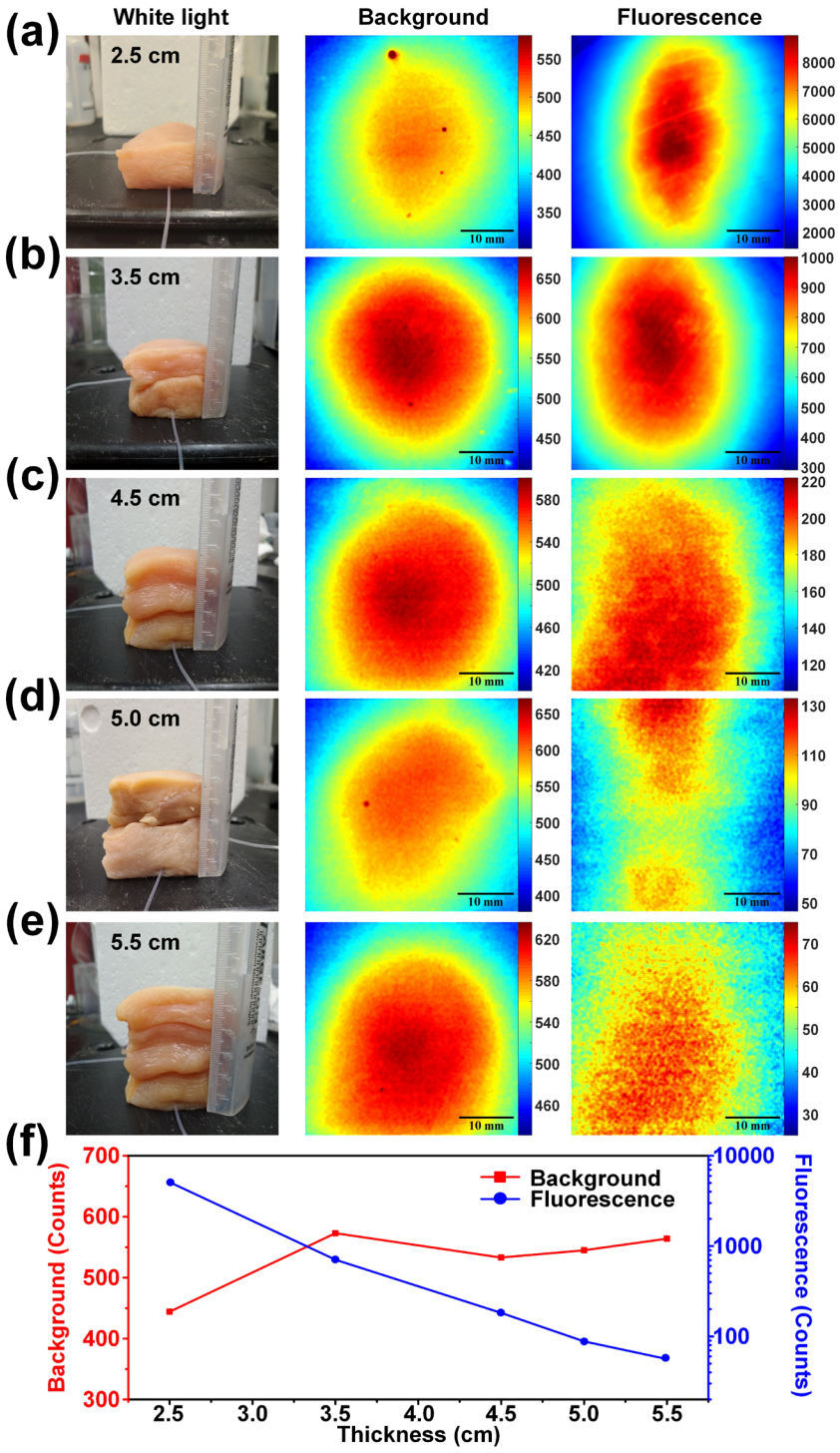

Figure 5-6 The white light photo, background image (I_{BG}) and background fluorescence image (I_{BGF}) of the silicone tube embedded in chicken breast tissue with a thickness of (a) 2.5 cm, (b) 3.5 cm, (c) 4.5 cm, (d) 5.0 cm and (e) 5.5 cm. (f) The average intensity of the background images (the red line with squares, and see the left y axis with a linear

scale) and the average intensity of the background fluorescence images (the blue line with circles, and see the right y axis with a logarithm scale) at different thicknesses.

5.3.4 2D-USF-Signal Images

A 2D-USF-signal image ($I_{2D-USF-sig}$) at a specific scan position of the ultrasound focus is defined as the subtracted image between the two images acquired from the EMCCD camera after (I_{US-On}) and before (I_{US-Off}) the ultrasound is applied. The following equation illuminates the relationship among these images: $I_{2D-USF-sig} = I_{US-On} - I_{US-Off} = (I_{2D-USF-sig} + I_{BG} + I_{BGF}) - (I_{BG} + I_{BGF})$, where $I_{2D-USF-sig}$ represents ultrasound-induced fluorescence increase and is the real USF signal that we are detecting. I_{BG} and I_{BGF} are the background image and background fluorescence image, respectively, discussed in the previous section. By subtracting I_{US-Off} from I_{US-On}, both the I_{BG} and I_{BGF} can be removed and the real 2D-USF-signal image $I_{2D-USF-sig}$ can be found.

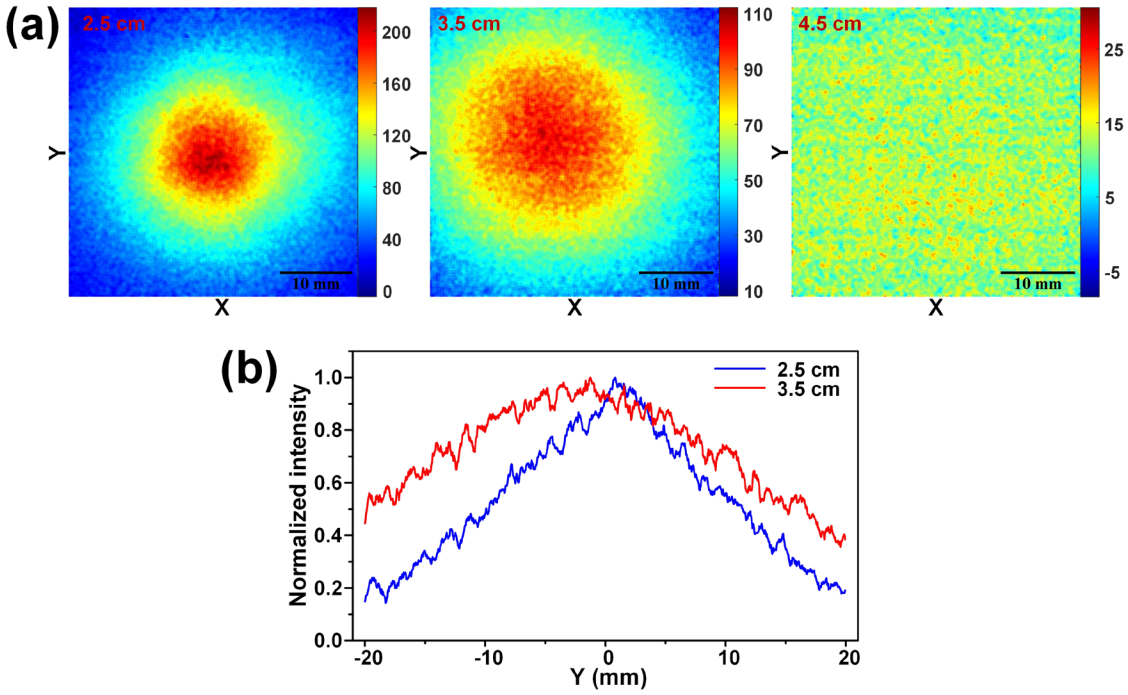

Figure 5-7 (a) Three 2D-USF-signal image when the ultrasound focus is scanned on the silicone tube embedded in chicken breast tissue with three different thicknesses, 2.5 , 3.5 and 4.5 cm, respectively. (b) The 1D profiles of the 2D-USF-signal image across the geometric center along the Y direction with the tissue thickness of 2.5 cm (the blue line) and 3.5 cm (the red line).

Figure 5-7(a) shows a typical example of a 2D-USF-signal image when the ultrasound focus is scanned on the silicone tube embedded in chicken breast tissue with three different thicknesses, 2.5, 3.5 and 4.5 cm, respectively. Figure 5-7(b) shows the 1D profiles of the Figure 5-7(a) across the geometric center along the Y direction for the tissue thickness of 2.5 cm (the red line) and 3.5 cm (the blue line). The FWHM of the 1D profiles significantly increases from 21.32 mm to 34.84 mm when the tissue thickness rises from 2.5 to 3.5 cm. The circular shape of the 2D-USF-signal image is even not recognizable in the 4.5 cm-thick chicken breast due to the increased light scattering from the thicker tissue.

5.3.5 USF Imaging of the Sub-Millimeter Silicone Tube Embedded in Chicken Breast Tissue

All the signals shown on a 2D-USF-signal image are generated from USF photons and induced by the ultrasound focus at a specific scan point. We average these signals to form a single value to represent the USF signal at this specific scan point of the ultrasound focus. By scanning the ultrasound focus on the X-Y 2D plane, we can form a 2D USF image. Figure 5-8(a) shows the 2D USF images of the sub-millimeter silicone tube with an EM gain of 1, 3, 9, 27 and 54 in the 4.5 cm-thick chicken breast tissue. The image of the silicone tube is very noisy with the EM gain of 1. When increasing of the gain from 1 to 9, the image becomes much clearer. However, further increasing the gain from 9 to 54, the quality of images remains similar. The SNR values are 10.69(±1.39), 14.88(±1.39), 23.52(±2.96), 21.7(±0.64) and 20.88(±0.35) dB corresponding to the EM gain of 1, 3, 9, 27 and 54, respectively. Obviously, by optimizing the EM gain, we can significantly improve the SNR of a USF image. By adopting the optimized EM gain, Figure 5-8(b) shows the USF images of the silicone tube in the different thick chicken breast tissues (2.5 cm: EM gain 3; 3.5, 4.5 and 5.0 cm: EM gain 9; 5.5 cm: EM gain 54). The SNR values are 41.56(±1.96), 37.45(±3.75), 23.53(±2.96), 12.78(±2.07) and 8.69(±1.46) dB corresponding to the thickness of 2.5 cm, 3.5 cm, 4.5 cm, 5.0 cm and 5.5 cm, respectively. Although the SNR still decreases with the increase of tissue thickness, the decrease of image quality slows down because the SNR at deeper tissue is improved by the optimized EM gain. Figure 5-8(c) shows the SNR of the USF images versus the EM gain in different thick tissues. The SNR increases quickly when the EM gain rises from 1 to 9 (thickness: 2.5 cm, 3.5 cm, 4.5 cm and 5.0 cm) and then reduces slightly or remains stable when the EM gain rises from 9 to 54 (thickness: 4.5 cm and 5.0 cm). Figure 5-8(d) shows the USF signal and the noise versus the EM gain for the 4.5 cm- and 5.0 cm-thick tissue samples. In both thicknesses, the USF signal shows a higher increase rate than the noise in the gain range of 1–9. However, after gain is >9, both the signal and the noise show a similar increase rate versus the gain, which explains why the SNR becomes flat when gain is >9. Figure 5-8(e) shows the

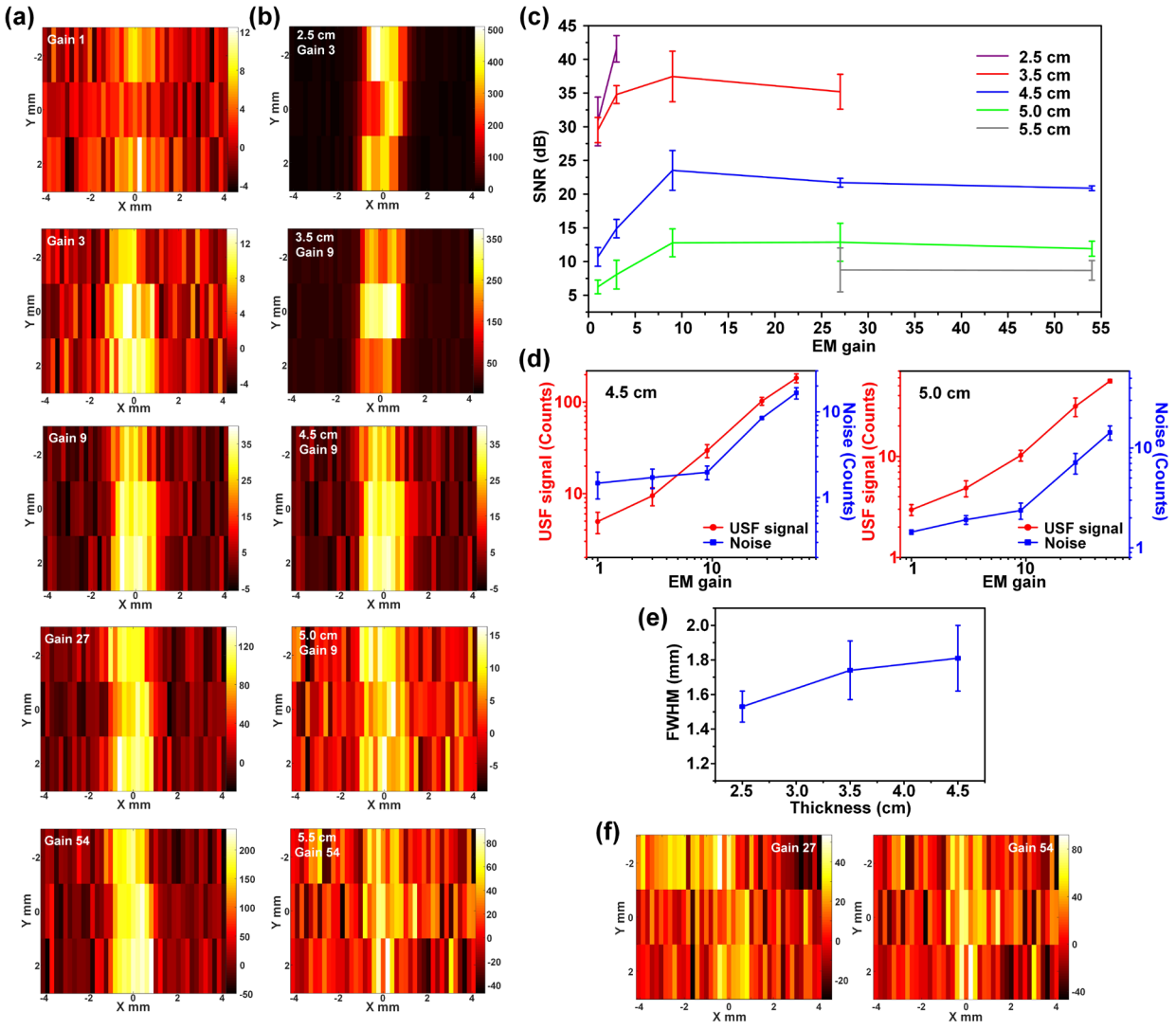

Figure 5-8 (a) The USF images of the silicone tube in the 4.5 cm-thick chicken breast tissue with different EM gains of 1, 3, 9, 27 and 54, respectively. (b) The USF images of the silicone tube in the chicken breast tissue with different thicknesses of 2.5, 3.5, 4.5, 5.0 and 5.5 cm, and with an EM gain of 3, 9, 9, 9 and 54, respectively. (c) The SNR of the USF images with different EM gains in various thick tissue (2.5 cm: purple line; 3.5 cm: red line; 4.5 cm: blue line; 5.0 cm: green line; 5.5 cm: grey line). (d) The average intensity of USF signal (red line with circles) and the average intensity of noise (blue line with squares) with different EM gains in 4.5 cm-thick tissue and 5.0 cm-thick tissue. (e) The FWHM of the USF image of the silicone tube with different thicknesses (2.5 cm: EM gain 3; 3.5 cm: EM gain 9; 4.5 cm: EM gain 9). (f) The USF images of the silicone tube embedded in 5.5 cm-thick chicken breast tissue with a gain of 27 (left) and 54 (right), respectively.

FWHM of the USF images of the silicone tube in different thick tissues. They are closed to the outer diameter of the silicone tube (i.e., 1.65 mm). Ideally, the FWHM is mainly determined by the convolution of the ultrasound or thermal focal size (the lateral FWHM of the acoustic intensity focus is 0.55 mm) with the object size, and should be independent of tissue's thickness. The slight increase of the FWHMs in Figure 5-8(e) may be because of the fact that the USF images become much noisier in deeper tissue and the estimated FWHMs are less accurate than those in shallower tissue. It should be noted that the USF imaging system reaches its detection limitation in 5.5 cm-thick chicken breast tissue with current setting so that the quantitative analysis may be not reliable. The silicone tube can only be roughly differentiated with an EM gain of 54, although the SNRs of with the EM gain of 27 and 54 are similar (Figure 5-8(f)).

5.3.6 The Comparison between the ICG-Liposome and the ICG-Nanogel

Figure 5-9(a) shows the fluorescence intensity as a function of the temperature of the sample solution (ICG-liposome: red line with circles; ICG-nanogel: blue line with squares). The fluorescence increase of the ICG-liposome is much sharper than that of the ICG-nanogel. As mentioned in Figure 5-4(a), the fluorescence increases 2.02 folds in a narrow temperature range of 2.0 ˚C (i.e., from 38.4 to 40.4 ˚C). The ICG-nanogel shows an LCST at 35.1 ˚C and the fluorescence increases 2.74 folds in a relatively wide temperature range of 7.4 ˚C (i.e., from 35.1 to 42.5 ˚C). In addition, the increase of the absolute fluorescence intensity of the ICG-liposome was 3.0 times stronger than that of ICG-nanogel (i.e., 5.12e6 counts versus 1.69e6 counts). A stronger increase in the absolute fluorescence intensity ($\Delta I_{On-Off} = I_{On} - I_{Off}$) within a narrower temperature range ($\Delta T_{On-Off} = T_{On} - T_{Off}$) indicates a higher (absolute) temperature sensitivity of the contrast agent (i.e., $S_{abs} = \Delta I_{On-Off}/\Delta T_{On-Off}$), which has a unit of counts per ˚C. The S_{abs} of the ICG-liposome and ICG-nanogel are 2.56e6 counts/˚C and 0.23e6 counts/ ˚C, respectively. The higher temperature sensitivity of the contrast agent will be favorable for USF imaging to achieve a higher SNR because it will provide more USF photons using the same ultrasound/thermal energy. This speculation is verified in Figure 5-9(b) and 9(c) in which the SNR of the USF image of the silicone tube filled with the ICG-liposome (Figure 5-9(b)) and ICG-nanogel (Figure 5-9(c)) is 30.79 (±3.61) dB and 26.34 (±2.03) dB, respectively (note that the tissue thickness is 2.5 cm and the EM gain is 1, and all other experimental parameters remained the same). Therefore, the ICG-liposome has a better USF performance than the ICG-nanogel because of its higher temperature sensitivity.

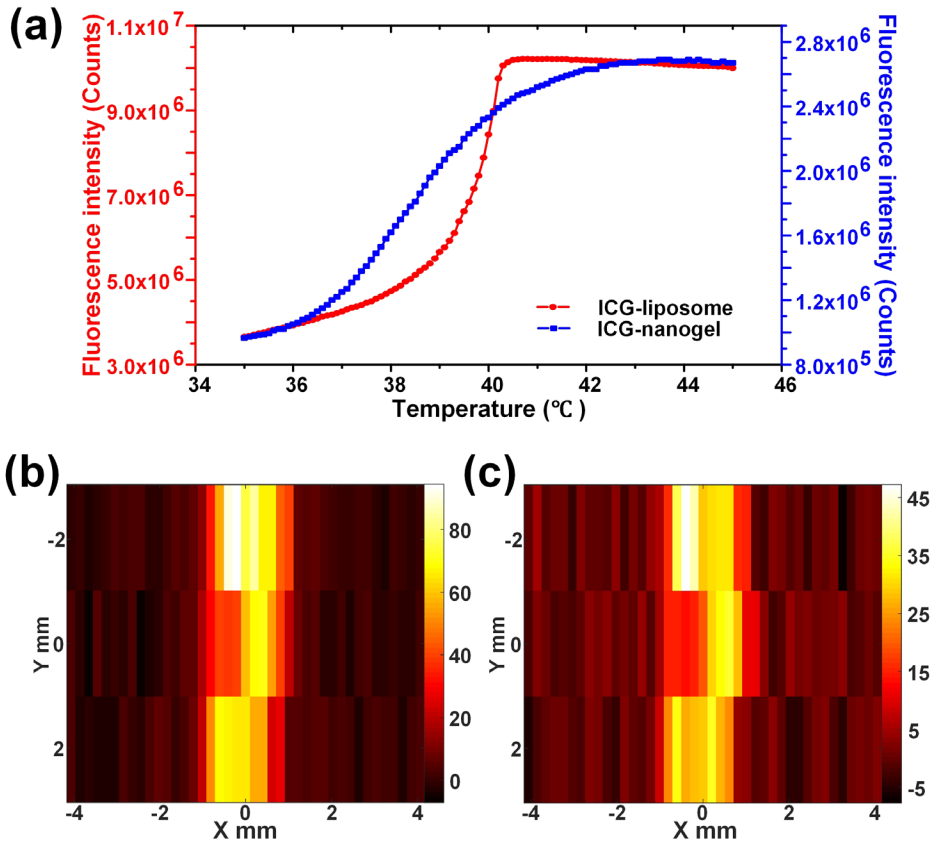

Figure 5-9 (a) The fluorescence intensity of the ICG-liposome (the red line with circles) and the ICG-nanogel (the blue line with squares) versus temperature. The USF image of the silicone tube filled with ICG-liposome (b) and ICG-nanogel (c) in 2.5 cm-thick chicken breast tissue with an EM gain of 1. All experiment parameters were same.

5.4 Discussion

In current study, we demonstrated that improving the sensitivity of both the USF contrast agent and the imaging system could significantly increase the SNR of USF imaging. The USF imaging of a silicone tube in a 5.5 cm-thick (i.e., 5.0 cm deep from the top) chicken breast tissue with an illumination intensity of 28.35 mW/cm^2 was successfully demonstrated (Figure 5-8(b)) via two key factors: (1) the USF contrast agent with high temperature sensitivity; (2) the USF imaging system with high detection sensitivity.

In our previous studies, we usually defined a fluorescence on-to-off ratio of the USF contrast agent ($R_{On/Off} = I_{On}/I_{Off}$) as a parameter to characterize the contrast agent's USF performance [24, 31]. Recently, we reported that this ratio was an effective parameter only when the background photons (i.e., the autofluorescence and laser leakage) are significantly less than the background fluorescence photons generated from the non-100%-off

contrast agent [74]. This is usually happening in shallow-tissue USF imaging (such as at a depth of <2-3 cm). When imaging deep tissue (such as >3 cm) or the USF contrast agent has a very low quantum efficiency at the off state, the background fluorescence photons are much weaker than or comparable to the background photons (Figure 5-6). In this situation, the $R_{On/Off}$ is less effective to characterize the contrast agent's USF performance. Instead, the on-and-off difference of the absolute fluorescence intensity (ΔI_{On-Off}) becomes a good indicator for the USF contrast agent if other parameters remain the same. In addition, we also moved one more step further to define the (absolute) temperature sensitivity of a USF contrast agent ($S_{abs} = \Delta I_{On-Off}/\Delta T_{On-Off}$) after comparing the two types of contrast agents, ICG-liposomes versus ICG-nanogels. Obviously, a contrast agent with high (absolute) temperature sensitivity should provide a high SNR in USF imaging, which has been demonstrated in Figure 5-9.

It is important to point out that the noise of the USF imaging is different from the noise of the 2D planar fluorescence imaging via an EMCCD camera. In 2D planar fluorescence imaging, the main noise components are photon shot noise, dark current noise, clock induced charge noise and readout noise [75]. These noise electrons directly affect each pixel of the image taken by the camera. However, the noise of the USF imaging is the variation of the difference of the mean spatial intensities between two sequential images taken by the camera when ultrasound is off. In an ideal situation, this difference of the mean spatial intensities should be zero or an invariable value. According to the definition of the USF image's noise, the noise would be zero in this ideal situation. Unfortunately, the difference in a real case is variable because of various reasons, such as the excitation light, bias of the camera and/or the variation of the EM gain, and others, which are unstable and dependent on environment.

In this study, we focused on: (1) the method to stabilize the EM gain; (2) the affection of the EM gain on USF image's quality while all other parameters kept the same. The EM gain is more stable in MATLAB trigger mode than the external hardware trigger mode (Figure 5-5). The reason may be the larger environment temperature change inside the camera while waiting for an external hardware trigger. The higher environment temperature inside the camera may reduce the probability of charge multiplication and therefore lower the EM gain under the same voltage applied across the multiplication register [76]. It is interesting to find that the changes of the mean intensity curves are opposite in these two modes. The temperature of the sensor is kept at -55℃ (default value) through thermoelectric cooling with an internal fan. However, the real temperature may be above this value when the circuit is working (e.g., waiting for the external trigger or taking images). New thermal equilibrium would be reached at a temperature (T1: taking images; T2: waiting for the external trigger; T1<T2) lower than -55℃. Thus, the spatial mean intensity

decreases (Figure 5-5(e))/increases (Figure 5-5(f)) when the generated thermal energy is more/less than that taken away by the cooling system.

The noise increases much slower than the USF signal when the EM gain rises from 1 to 9, and follows a similar increase as the USF signal when the EM gain is larger than 9 (Figure 5-8(d)). As mentioned above, the change of the USF imaging's noise is coming from the change of the stability of the EM gain because all other parameters are same. The EM gain seems to be more stable when the gain is low (<9). Thus, rising the EM gain (<9 in this study) helps to improve the SNR of the USF image in a tissue with a thickness less than 5.5 cm (Figure 5-8(c)). Lastly, it should be mentioned that current study aims to demonstrate a general concept that the SNR in USF imaging can be improved by optimizing the EMCCD's gain. However, because we have not investigated other types of EMCCD cameras, cautions should be taken when extending the specific numbers provided here into other studies (such as the optimized gain of 9) because the numbers may vary among different cameras. Similarly, the conclusion about the trigger mode should be used cautiously when other model of EMCCD cameras are used.

5.5 Conclusion

In this study, we successfully achieved USF imaging of a sub-millimeter silicone tube (inner diameter: 0.76 mm, outer diameter: 1.65 mm) embedded in centimeter-deep chicken breast tissue (2.5, 3.5, 4.5, 5.0 and 5.5 cm) using a low intensity excitation light (28.35 mW/cm^2). The SNR improving strategies include (1) adopting a new contrast agent, ICG-liposome, with high USF performance and (2) stabilizing and optimizing the EM gain in the USF imaging system via a software trigger mode. The ICG-liposome showed better USF performance than the previous ICG-nanogel in deep tissue. The gain of the EMCCD camera used in the USF imaging system was stabilized by using the MATLAB trigger mode instead of the external hardware trigger mode. In conclusion, USF imaging can achieve high sensitivity (SNR) and high spatial resolution in several centimeters deep tissues using a low-intensity NIR-I excitation laser. With these unique features, it has dramatic potentials for different biomedical applications in future.

Chapter 6

CONCLUSIONS AND FUTURE WORK

6.1 Conclusions

This dissertation aims to demonstrate the feasibility of *in vivo* USF imaging via various NIR USF contrast agents and develop camera-based USF imaging systems suitable for the *in vivo* study. The specific objectives of this work were to: (1) investigate the biodistribution of PINIPAM-ICG NP and demonstrate its feasibility of USF imaging in mice; (2) develop a camera-based USF imaging system and a Z-scan method; (3) study the biodistribution of PNIPAM/β-CD/ICG nanogel in mice and demonstrate its feasibility of USF imaging using the camera-based USF imaging system; (4) improve the EMCCD-based USF imaging system by using software trigger. The specific objectives have been accomplished in the studies presented in Chapters 2–5.

In Chapter 2, we, for the first time, successfully demonstrate the feasibility of *in vivo* USF imaging in mice. The USF contrast agent adopted in this study, PNIPAM-ICG NP, was proved to be stable in biological environments (such as in breast tumor and spleen). Biodistribution studies showed that PNIPAM-ICG NP was mainly accumulated in the spleen of mice. Thus, it provided a good opportunity to conduct *in vivo* USF imaging. The *ex vivo* USF imaging in a heart tissue and *in vivo* USF imaging in a mouse breast tumor via local injections were obtained. The *ex vivo* and *in vivo* USF imaging of mouse spleen were also realized. All the results were validated by the commercial micro-CT system. Due to the nonuniformity of the ultrasound focus, the USF achieved similar accuracy to CT on the lateral plane (i.e., the horizontal XY plane orthogonal to the direction of the ultrasound wave propagation), and lower accuracy than CT in the axial direction (i.e., the direction of the ultrasound wave propagation).

In Chapter 3, a camera-based USF imaging system was developed to overcome the limitations of the previous fiber-bundle-based USF imaging systems, such as low photon collection efficiency, unsuitable for scanning an uneven surface and low scanning speed. Because the spatial information for the fluorescence distribution at the tissue surface was acquired in this system, the desired scan area could be precisely selected. With the camera as the detector, a smart scan method, Z-scan, was developed, which improved the imaging speed by four times over the raster scan method adopted by the previous systems. Two temporally adjacent scan positions were spatially well separated, which significantly reduce the effect of thermal diffusion and signal crosstalk. The resolution of the proposed imaging system was investigated by using a piece of porcine muscle tissue with a silicone tube. To evaluate the accuracy of the newly

developed USF system, the USF imaging of contrast agent distribution in the porcine tongue tissues were carried out. The USF images were validated by a commercial CT imaging system.

In Chapter 4, the biodistribution of the PNIPAM/β-CD/ICG nanogel and its feasibility of USF imaging in mice were studied. The PNIPAM-ICG NP has a restriction of bule shifted spectrum compared to ICG itself. To overcome the limitation, the PNIPAM/β-CD/ICG nanogel was proposed recently. In this study, it was demonstrated to have a much better USF performance than the PNIPAM-ICG NP in chicken breast tissues. Additionally, its biodistribution in BALB/c mice was different with that of PNIPAM-ICG NP due to the various particle's sizes (i.e., 32 nm for PNIPAM/β-CD/ICG nanogel versus 335 nm for PNIPAM-ICG NP). The nanogels could accumulated into mouse liver in a short time and then quickly excreted through the synergistic pathways of the hepatic route and renal clearance. Thus, *ex vivo* USF imaging of mouse liver was achieved instead of *in vivo* USF imaging. Animal studies based on U87 tumor-bearing mice revealed that the present nanogels could accumulate into tumor via an EPR effect. *In vivo* high-resolution USF imaging of contrast agent distribution in tumor via local injections was successfully achieved.

In Chapter 5, an EMCCD-based USF imaging system using software trigger was proposed. It was improved from the system developed in Chapter 3 which using the external hardware trigger. Adopting MATLAB to control the EMCCD camera, not only simplify the system structure but also stabilize the EM gain. The SNRs of the USF images with various EM gain in different thick chicken breast tissues were investigated. The results showed that the SNR could be significantly improved with an EM gain increased from 1 to 9. However, the SNR would not increase with a larger EM gain (i.e., >9) due to the instability of the EM gain. By applying the modified USF system and a ICG-liposome with reduced size, the USF imaging of a sub-millimeter silicone tube (inner diameter: 0.76 mm, outer diameter: 1.65 mm) embedded in 5.5 cm-thick chicken breast tissue using an excitation laser with a low intensity of 28.35 mW/cm^2 was successfully achieved.

6.2 Limitations and Future Directions

6.2.1 In vivo USF Imaging in Mouse Tumor

In this study, the *in vivo* USF imaging in mouse tumor using PNIPAM-ICG NP and PNIPAM/β-CD/ICG nanogel via local injections were successfully achieved. However, the *in vivo* USF imaging in mouse tumor via intravenous injection has not been realized yet. The PNIPAM/β-CD/ICG nanogel with a size of 32 nm shows a promising result that it can accumulated into the U87 tumor via EPR effect. Unfortunately, the concentration of the

nanogels in tumor is not high enough for USF imaging. Currently, the fluorescence of PNIPAM/β-CD/ICG nanogel increases 2.74 folds in a relatively wide temperature range of 7.4 ˚C (i.e., from 35.1 to 42.5 ˚C), which may be not enough for *in vivo* USF imaging in tumor via intravenous injection. Thus, it is highly desirable to develop new USF contrast agents that have better switching performance (such as high on-to-off ratio, narrow-switching bandwidth, in near-infrared region, etc.), are feasible for molecular targeting, and are biocompatible and biodegradable.

6.2.2 Further Improving the Imaging Speed

In this study, EMCCD camera-based USF imaging systems which can well overcome the limitations of the previous fiver-bundle based USF imaging systems are proposed. Thanks to the spatial information provided by the camera, a new scan method, Z scan, is developed to significantly improve the imaging speed. However, the further improvement of imaging speed is limited by the mechanical scanning with a single HIFU transducer. In current USF imaging systems, the HIFU transducer is mounted on a 3D translation stage. By moving the translation stage, the HIFU transducer heat the tissue point by point to generate a USF image. Nevertheless, the moving speed of the translation stage is limited and simultaneously scanning several areas cannot be realized. To further improve the scanning speed of the USF imaging system, a HIFU array is helpful as it can generate multi-focus simultaneously to scan multiple areas, which is currently investigated both experimentally and theoretically in our laboratory (PI: Dr. Baohong Yuan and the advisor of this dissertation).

Reference

1. Lichtman JW and Conchello J-A. Fluorescence microscopy. Nature methods 2005;2(12):910-9.
2. Santi PA. Light sheet fluorescence microscopy: a review. Journal of Histochemistry & Cytochemistry 2011;59(2):129-38.
3. Hilderbrand SA and Weissleder R. Near-infrared fluorescence: application to in vivo molecular imaging. Current opinion in chemical biology 2010;14(1):71-9.
4. Van Dam GM, et al. Intraoperative tumor-specific fluorescence imaging in ovarian cancer by folate receptor-α targeting: first in-human results. Nature medicine 2011;17(10):1315-9.
5. Corlu A, et al. Three-dimensional in vivo fluorescence diffuse optical tomography of breast cancer in humans. Optics express 2007;15(11):6696-716.
6. Xu CT, et al. High-resolution fluorescence diffuse optical tomography developed with nonlinear upconverting nanoparticles. ACS nano 2012;6(6):4788-95.
7. Hu C-D and Kerppola TK. Simultaneous visualization of multiple protein interactions in living cells using multicolor fluorescence complementation analysis. Nature biotechnology 2003;21(5):539-45.
8. Yamamoto N, et al. Tumor imaging with multicolor fluorescent protein expression. International journal of clinical oncology 2011;16(2):84-91.
9. Frangioni JV. In vivo near-infrared fluorescence imaging. Current opinion in chemical biology 2003;7(5):626-34.
10. Shung KK. Diagnostic ultrasound: Imaging and blood flow measurements: CRC press; 2015.
11. Wang LV. Multiscale photoacoustic microscopy and computed tomography. Nature photonics 2009;3(9):503-9.
12. Kobayashi M, et al. Fluorescence tomography in turbid media based on acousto-optic modulation imaging. Applied Physics Letters 2006;89(18):181102.
13. Yuan B, et al. Microbubble-enhanced ultrasound-modulated fluorescence in a turbid medium. Applied physics letters 2009;95(18):181113.
14. Yuan B. Diffuse optical tomography and fluorescence diffuse optical tomography: University of Connecticut; 2006.
15. Yuan B, et al. Mechanisms of the ultrasonic modulation of fluorescence in turbid media. Journal of applied physics 2008;104(10):103102.

16. Lin Y, et al. Temperature-modulated fluorescence tomography in a turbid media. Applied physics letters 2012;100(7):073702.
17. Lin Y, et al. Temperature-modulated fluorescence tomography based on both concentration and lifetime contrast. Journal of biomedical optics 2012;17(5):056007.
18. Yuan B, et al. High-resolution imaging in a deep turbid medium based on an ultrasound-switchable fluorescence technique. Applied physics letters 2012;101(3):033703.
19. Xu X, et al. Time-reversed ultrasonically encoded optical focusing into scattering media. Nature photonics 2011;5(3):154-7.
20. Si K, et al. Fluorescence imaging beyond the ballistic regime by ultrasound-pulse-guided digital phase conjugation. Nature photonics 2012;6(10):657-61.
21. Si K, et al. Breaking the spatial resolution barrier via iterative sound-light interaction in deep tissue microscopy. Scientific reports 2012;2:748.
22. Wang YM, et al. Deep-tissue focal fluorescence imaging with digitally time-reversed ultrasound-encoded light. Nature communications 2012;3(1):1-8.
23. Judkewitz B, et al. Speckle-scale focusing in the diffusive regime with time reversal of variance-encoded light (TROVE). Nature photonics 2013;7(4):300-5.
24. Pei Y, et al. High resolution imaging beyond the acoustic diffraction limit in deep tissue via ultrasound-switchable NIR fluorescence. Scientific Reports 2014;4(1):4690.
25. Cheng B, et al. High-Resolution Ultrasound-Switchable Fluorescence Imaging in Centimeter-Deep Tissue Phantoms with High Signal-To-Noise Ratio and High Sensitivity via Novel Contrast Agents. PLOS ONE 2016;11(11):e0165963.
26. Kandukuri J, et al. A Dual-Modality System for Both Multi-Color Ultrasound-Switchable Fluorescence and Ultrasound Imaging. International Journal of Molecular Sciences 2017;18(2):323.
27. Kandukuri J, et al. Modulation of ultrasound-switchable fluorescence for improving signal-to-noise ratio. Journal of Biomedical Optics 2017;22(7):076021.
28. Yuan B. Ultrasound-modulated fluorescence based on a fluorophore-quencher-labeled microbubble system. Journal of Biomedical Optics 2009;14(2):024043.

29. Wang LV and Hu S. Photoacoustic tomography: in vivo imaging from organelles to organs. science 2012;335(6075):1458-62.
30. Ollinger JM and Fessler JA. Positron-emission tomography. IEEE Signal Processing Magazine 1997;14(1):43-55.
31. Yu S, et al. New generation ICG-based contrast agents for ultrasound-switchable fluorescence imaging. Scientific Reports 2016;6(1):35942.
32. Yu S, et al. An ICCD camera-based time-domain ultrasound-switchable fluorescence imaging system. Scientific Reports 2019;9(1):10552.
33. Yuan B, et al. Breaking the acoustic diffraction limit via nonlinear effect and thermal confinement for potential deep-tissue high-resolution imaging. Applied physics letters 2013;102(6):063703.
34. Harris GR, editor FDA regulation of clinical high intensity focused ultrasound (HIFU) devices. 2009 Annual International Conference of the IEEE Engineering in Medicine and Biology Society; 2009: IEEE.
35. Wells P. Absorption and dispersion of ultrasound in biological tissue. Ultrasound in medicine & biology 1975;1(4):369-76.
36. Cheng B, et al. Development of ultrasound-switchable fluorescence imaging contrast agents based on thermosensitive polymers and nanoparticles. Ieee Journal of Selected Topics in Quantum Electronics 2013;20(3):67-80.
37. Cheng B, et al. The Mechanisms and Biomedical Applications of an NIR BODIPY-Based Switchable Fluorescent Probe. International Journal of Molecular Sciences 2017;18(2):384.
38. Liu R, et al. Temperature-sensitive polymeric nanogels encapsulating with β-cyclodextrin and ICG complex for high-resolution deep-tissue ultrasound-switchable fluorescence imaging. Nano Research 2020;13(4):1100-10.
39. Landsman M, et al. Light-absorbing properties, stability, and spectral stabilization of indocyanine green. Journal of applied physiology 1976;40(4):575-83.
40. Ntziachristos V, et al. Fluorescence molecular tomography resolves protease activity in vivo. Nature medicine 2002;8(7):757-61.
41. Engelbrecht CJ, et al. Ultra-compact fiber-optic two-photon microscope for functional fluorescence imaging in vivo. Optics express 2008;16(8):5556-64.

42. McDonald DM and Choyke PL. Imaging of angiogenesis: from microscope to clinic. Nature medicine 2003;9(6):713-25.
43. Yuan B and Zhu Q. Separately reconstructing the structural and functional parameters of a fluorescent inclusion embedded in a turbid medium. Optics express 2006;14(16):7172-87.
44. Huynh NT, et al. Ultrasound modulated imaging of luminescence generated within a scattering medium. Journal of biomedical optics 2013;18(2):020505.
45. Ahmad J, et al. Ultrasound-mediation of self-illuminating reporters improves imaging resolution in optically scattering media. Biomed Opt Express 2018;9(4):1664-79.
46. WENQING LJL and Jianzhuang L. The Automatic thresholding of gray-level pictures via two-dimensional otsu method [J]. Acta Automatica Sinica 1993;1:015.
47. Culjat MO, et al. A review of tissue substitutes for ultrasound imaging. Ultrasound in medicine & biology 2010;36(6):861-73.
48. Moghimi SM, et al. Long-circulating and target-specific nanoparticles: theory to practice. Pharmacological reviews 2001;53(2):283-318.
49. Boll H, et al. Comparison of Fenestra LC, ExiTron nano 6000, and ExiTron nano 12000 for micro-CT imaging of liver and spleen in mice. Academic Radiology 2013;20(9):1137-43.
50. Brigger I, et al. Nanoparticles in cancer therapy and diagnosis. Advanced drug delivery reviews 2012;64:24-36.
51. Yao T, et al. In vivo ultrasound-switchable fluorescence imaging. Scientific Reports 2019;9(1):9855.
52. Zhang Q, et al. Nanoscale Ultrasound-Switchable FRET-Based Liposomes for Near-Infrared Fluorescence Imaging in Optically Turbid Media. Small 2017;13(33):1602895.
53. Kwong TC, et al. Feasibility study of high spatial resolution multimodality fluorescence tomography in ex vivo biological tissue. Applied optics 2017;56(28):7886-91.
54. Liu Y, et al. Ultrasound-modulated fluorescence based on donor-acceptor-labeled microbubbles. Journal of Biomedical Optics 2015;20(3):036012.
55. Liu Y, et al. Ultrasound-modulated fluorescence based on fluorescent microbubbles. Journal of biomedical optics 2014;19(8):085005.
56. Huynh NT, et al. Effect of object size and acoustic wavelength on pulsed ultrasound modulated fluorescence signals. Journal of biomedical optics 2012;17(7):076008.

57. Yao T, et al. Ultrasound-Switchable Fluorescence Imaging via an EMCCD Camera and a Z-Scan Method. IEEE Journal of Selected Topics in Quantum Electronics 2019;25(2):1-8.
58. Shou K, et al. Multifunctional biomedical imaging in physiological and pathological conditions using a NIR-II Probe. Advanced functional materials 2017;27(23):1700995.
59. Carr JA, et al. Shortwave infrared fluorescence imaging with the clinically approved near-infrared dye indocyanine green. Proceedings of the National Academy of Sciences 2018;115(17):4465-70.
60. Hong G, et al. Near-infrared fluorophores for biomedical imaging. Nature Biomedical Engineering 2017;1(1):1-22.
61. Qi J, et al. Aggregation-induced emission luminogen with near-infrared-II excitation and near-infrared-I emission for ultradeep intravital two-photon microscopy. ACS nano 2018;12(8):7936-45.
62. Zhao J, et al. NIR-I-to-NIR-II fluorescent nanomaterials for biomedical imaging and cancer therapy. Journal of Materials Chemistry B 2018;6(3):349-65.
63. Yuan A, et al. Application of near-infrared dyes for tumor imaging, photothermal, and photodynamic therapies. Journal of pharmaceutical sciences 2013;102(1):6-28.
64. Resch-Genger U, et al. Quantum dots versus organic dyes as fluorescent labels. Nature methods 2008;5(9):763.
65. Bhavane R, et al. NIR-II fluorescence imaging using indocyanine green nanoparticles. Scientific reports 2018;8(1):1-10.
66. Wang Y-F, et al. Nd3+-sensitized upconversion nanophosphors: efficient in vivo bioimaging probes with minimized heating effect. ACS nano 2013;7(8):7200-6.
67. Hong G, et al. Multifunctional in vivo vascular imaging using near-infrared II fluorescence. Nature medicine 2012;18(12):1841-6.
68. Chen G, et al. (α-NaYbF4: Tm3+)/CaF2 core/shell nanoparticles with efficient near-infrared to near-infrared upconversion for high-contrast deep tissue bioimaging. ACS nano 2012;6(9):8280-7.
69. Yu M and Zheng J. Clearance pathways and tumor targeting of imaging nanoparticles. ACS nano 2015;9(7):6655-74.
70. Imamura T, et al. In vivo optical imaging of cancer cell function and tumor microenvironment. Cancer science 2018;109(4):912-8.
71. Dang X, et al. Deep-tissue optical imaging of near cellular-sized features. Scientific reports 2019;9(1):1-12.

72. Wan H, et al. A bright organic NIR-II nanofluorophore for three-dimensional imaging into biological tissues. Nature communications 2018;9(1):1-9.
73. Antaris AL, et al. A small-molecule dye for NIR-II imaging. Nature materials 2016;15(2):235-42.
74. Liu Y, et al. A Biocompatible and Near-Infrared Liposome for In Vivo Ultrasound-Switchable Fluorescence Imaging. Advanced Healthcare Materials 2020;9(4):1901457.
75. Zhang WW, et al. Signal-to-Noise Ratio Improvement of EMCCD Cameras. World Academy of Science, Engineering and Technology 2010;4(5):966-70.
76. Ingley R, et al. Life testing of EMCCD gain characteristics. Nuclear Instruments and Methods in Physics Research Section A: Accelerators, Spectrometers, Detectors and Associated Equipment 2009;600(2):460-5.

Biographical Information

Tingfeng Yao received his Bachelor of Science degree in Electronic Information Science and Technology and Master of Science degree in Electromagnetic Field and Microwave Technology from Nanjing University of Aeronautics and Astronautics, Nanjing, China, in 2012, and 2015, respectively. He worked in Prof. Shilong Pan's Microwave Photonics Research Laboratory from 2011 to 2015, Nanjing University of Aeronautics and Astronautics, and focused on developing distributed localization system based on microwave photonics technique. After that, he continues his graduate study in the U.S. and received the Doctor of Philosophy degree in Biomedical Engineering at the Joint Program of University of Texas at Arlington and the University of Texas Southwestern Medical Center, Texas, USA, in 2020. During this time, he worked as a research assistant in Prof. Baohong Yuan's Ultrasound and Optical Imaging laboratory. His expertise includes medical imaging instrumentation, ultrasound and optical imaging, and signal processing. His research projects focused on developing and improving a novel hybrid imaging modality, ultrasound-switchable fluorescence-imaging, to realize high resolution fluorescence imaging in centimeters-deep tissue. As a doctoral student, he has published two first-author and two co-first-author journal papers, four co-author journal papers, presented three talks in prestigious conferences and filed one US patent. Currently, he is revising the third first-author journal paper. Based on his achievements, he was awarded Alfred and Janet Potvin Award in 2019 and Graduate Studies Dissertation Fellowship in 2020 from the University of Texas at Arlington. In the future, he hopes to develop more innovative medical technologies that can bring benefits to human health.